SCALE-BRIDGING MOLECULAR DYNAMICS SIMULATIONS OF PLASMA-SURFACE INTERACTIONS

BY

ABHILASH HARPALE

DISSERTATION

Submitted in partial fulfillment of the requirements
for the degree of Doctor of Philosophy in Aerospace Engineering
in the Graduate College of the
University of Illinois at Urbana-Champaign, 2018

Urbana, Illinois

Doctoral Committee:

Assistant Professor Huck Beng Chew, Chair
Professor Deborah Levin
Professor Philippe Geubelle
Professor Harley Johnson

ABSTRACT

Plasma processing of materials plays a vital part in electronic, aerospace, automobile, metal manufacturing and biomedical industries. Plasma-surface interactions can be divided into two categories: controlled and erosive. Controlled plasma interactions are used to pattern the surfaces of materials to achieve desirable electronic and mechanical properties in an ionizing chamber. Examples include focused ion beam (FIB) milling of silicon thin films and plasma patterning of graphene. Erosive interactions typically involve damage to surfaces in close proximity to high temperature, ionized gases in an uncontrolled environment. Examples include plasma facing components in reactor vessels and thermal protection system in re-entry spacecraft. Due to the complex chemistry at the plasma surface boundaries, it is difficulty to either control or predict the effect of plasma on the patterning or erosion of the material. In this dissertation, atomic scale simulations coupled with micromechanics models are used to study the patterning of graphene and the ablation of thermal protection systems resulting from controlled and erosive plasma-surface interactions, respectively.

Scalable and precise nanopatterning of graphene is an essential step for graphene-based device fabrication. Hydrogen-plasma reactions have been shown to narrow graphene only from the edges, or to selectively produce circular or hexagonal holes in the basal plane of graphene, but the underlying plasma-graphene chemistry is unknown. In part I of this dissertation, we characterize the surface patterning of graphene via low energy hydrogen plasma treatment across a range of ion energies, using scale-bridging molecular dynamic simulations. Our results uncover distinct etching mechanisms, operative within narrow ion energy windows, which explain the various plasma-graphene reactions observed experimentally. For monolayer graphene, specific ion energy ranges are demonstrated for stable isotropic (∼2 eV) versus anisotropic hole growth (∼20-30 eV) within the basal plane of graphene, as well as for pure edge etching (∼1 eV). For multilayered graphene, our results demonstrate the initial development of columnar holes, which transition to stepped-edge holes at higher fluence due to cumulative effects of basal-plane etching. The contributions of thermal radicals and dehydrogenation effects on the hole growth process are also discussed.

In part II of this dissertation, multi-scale simulations are used to study the erosive role of high temperature plasma generated by the shock heating of ambient gases on the surfaces of high velocity atmospheric re-entry space craft. We specifically examine the ablation of AVCOAT, which is a composite thermal protection system (TPS) material attached to the leading edge of the Orion multi-purpose crew vehicle. Phenol formaldehyde resin used as the matrix material in AVCOAT is modeled and its pyrolysis kinetics are determined using ReaxFF-based molecular dynamics (MD) simulations. Our MD simulations show that bulk pyrolysis starts at temperatures of ~500 K, and exhibits a temperature dependence that follows the Arrhenius law. The pyrolysis process initiates with the removal of -OH functional groups and -H atoms from aromatic C rings within the bulk phenolic resin to release H_2O, followed by breaking of these C rings to release C-based fragments. Through the calculation of rate constants associated with C-C bond breaking during the pyrolysis process, we determine the effective surface recession rates of phenolic resin as a function of temperature. The surface recession rates from MD are used to inform a thermal material response model, capable of predicting the char thickness, temperature and gas blowing rates of AVCOAT TPS at macroscopic length-scales. Our model predictions of the char thickness and temperature distributions, under a variety of heat loads, are in good agreement with prior experiments.

ACKNOWLEDGEMENTS

I would like to express my great appreciation to all the people who offered me support and made my PhD journey very enjoyable and interesting. First and foremost, I would like to express my gratitude for Prof. Chew who was extremely supportive and patient with me throughout my PhD. As my academic mentor he has taught me more than I can give his credit for. He has shown, by example, what a good scientist (and person) should be. I feel extremely privileged to have him as my advisor and consider him as a role model for my future endeavors.

I would like to thank my wonderful colleagues and for their camaraderie over the past four years. Our discussions and arguments were the fertile soil for intellectual development. The evenings spent playing video games in the office with Ruizhi and the numerous coffee trips and lunch breaks with Hoaran will be some of the most cherished memories of my time at UIUC.

I would like to thank my roommates Shripad and Giri for making the research less boring and painful by providing much needed distractions. I enjoyed all the TV shows, board games and numerous evening walks we had together. I appreciate the friendships that we have maintained since our days at IIT Bombay.

I would also like to thank Giri, Shekhar, Mim, Mai, Will and Dylan for coming together to form the Sunday night trivia team. Despite our consistent mediocre performance, we continued to show up for trivia every week over the past two years. It was a true testament of the persistence necessary for grad school.

Most importantly, I would like to thank my parents and my sister, Pinu. Their love and encouragement has always been with me and has helped me throughout my PhD journey. I am also grateful for the support of Datta mama and Madhu tai who were my closest family and home in the US.

Lastly, I would like to express my appreciation for Krannert Center for Performing Arts at UIUC. I have been a regular patron of their orchestras over the past 4 years and I am constantly amazed by the quality of artists they attract and the phenomenal music they bring to the community.

TABLE OF CONTENTS

Chapter 1. Introduction

Plasma is a partially or fully ionized gas consisting of a mixture of ions, electron, thermal and energetic radicals and molecules. Application of gaseous plasma to a surface can be used to modify its properties or cause material erosion. Plasma processing of materials plays a vital part in electronic, aerospace, automobile, metal manufacturing and biomedical industries.[1,2] Despite the wide spread use of plasma processing technologies, fundamental understanding of the surface reactions has been lacking due to complex chemistry of the plasma.

Plasma surface interactions can be classified into two categories: 1) controlled patterning of surfaces and 2) erosive damage to materials. The former is desirable and is widely used in the electronic industry. Examples of controlled plasma surface interactions are, focused ion beam (FIB) milling of silicon thin films and plasma patterning of graphene.[3,4] On the other hand, plasma interactions which cause uncontrolled, erosive damage to surfaces are undesirable and encountered when extremely high temperature gases interact with solids. Plasma facing components in nuclear reactors and heat shields in atmospheric re-entry vehicles are examples of materials subjected to the erosive effect of plasma.[5,6] For both these categories careful analysis of the surface chemistry is necessary to improve the resolution of plasma-based processing or to reduce the damage caused by plasma. This PhD dissertation focuses on the patterning of graphene (Part I) and the ablation of thermal protection systems (Part II) resulting from controlled and erosive plasma-surface interactions, respectively.

Plasmas are categorized based on their electron temperature and charge density. Low energy plasmas which are used for material patterning occupy the middle regions of the temperature-density space as shown in Fig 1.1.[1] The degree of ionization which determines the charge density ranges from few parts per billion to a high percent. It is controlled by the power supplied to the ionizing chamber in surface patterning setups. The electron temperature is determined by the mean kinetic energy of the species in the plasma and ranges from 100 to 10^5 K.[1] The patterning of materials using plasma involves the low energy plasma regimes of glow discharge and thermal plasma. Within the discharge the plasma is electrically neutral since the ionized gas and electrons are in equilibrium. However, downstream from the discharge the mixture has a net positive charge as the electrons travel fasters and coat the chamber surface with

a negatively charged layer called Langmuir sheath.[7] The potential difference accelerates the positively charged species toward the sample. Before interacting with the surface however, an ion electron recombination occurs in the Langmuir sheath. The accelerated but neutral gas atoms bombard the surface and produce various patterns. Due to high kinetic energy and low coulombic contribution at the surface the plasma physics can be considered classical in nature.[1] Thus, the dynamics of the interactions are accessible via classical molecular dynamics techniques used in part one of this dissertation.

Unlike the controlled environment of the ionizing chamber used for material processing, plasma sheaths generated by space craft re-entry heating depend of factors which cannot be regulated. The velocity profile of the re-entry, gaseous composition of the upper atmosphere and the shape of the vehicle are examples of the factors which influence the plasma characteristics.[8] Due to the challenges of in-flight measurements and the complexity of chemical and thermodynamic processes, the composition of the re-entry plasma sheath is not well understood. Fig 1.2 shows the schematic of various gas regions around a blunt body during atmospheric re-entry.[9] Early work done by NASA in the 1960s established the temperature of the plasma to be approximately 10,000 to 12,000 K.[8] The partially ionized and dissociated atmospheric gases are confined to the shockwave region shown in Fig 1.2, and do not directly contact the vehicle surface. The presence of the extremely high temperatures in close vicinity of the surface leads to strong radiation heating.[10] The heat causes the ablative material to thermally decompose and convert to gaseous state. These pyrolysis gases play a critical role in improving the thermal protection provided by the heat shield. They push the heated shock layer away from the surface resulting in a reduction of radiative heating, as shown by the red arrows in Fig 1.2. More importantly, the gases prevent the ionized atmospheric O and N ions in the re-entry plasma from reaching the material surface. As a result, the surface erosion is purely due to radiative heating, in sharp contrast to the mechanism present in controlled material patterning.

In part I of this dissertation (chapters 2-6), we study the etching of graphene via low energy hydrogen plasma treatment as an example of the controlled plasma processing of surfaces. Results from our MD simulations can be used to fine tune the plasma chamber parameters (power, gas pressure, flow rate, etc.) to improve the resolution of graphene patterning. In part II (chapters 7-11), we study the pyrolysis of the phenolic resin commonly used in ablative heat

shields of spacecraft. During high velocity atmospheric re-entry, the erosive nature of high temperature plasma generated by the shock heating of ambient gases results in pyrolysis of the ablative heat shields. Results from MD simulations were used to inform thermal material response models at the meso-scale to predict the temperature distributions and charring thickness of an AVCOAT thermal protection system (TPS) used in the Apollo and Orion re-entry vehicles.

1.1 Figures

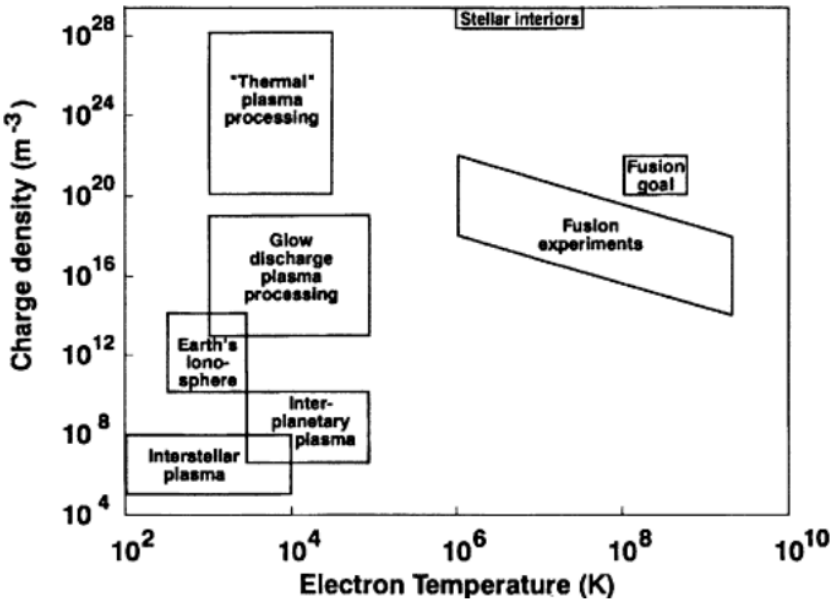

Fig 1.1: Various types of plasmas on the electron temperature-charge density plane. Glow discharge and thermal plasmas are involved in the controlled patterning of materials in ionizing chambers.[1]

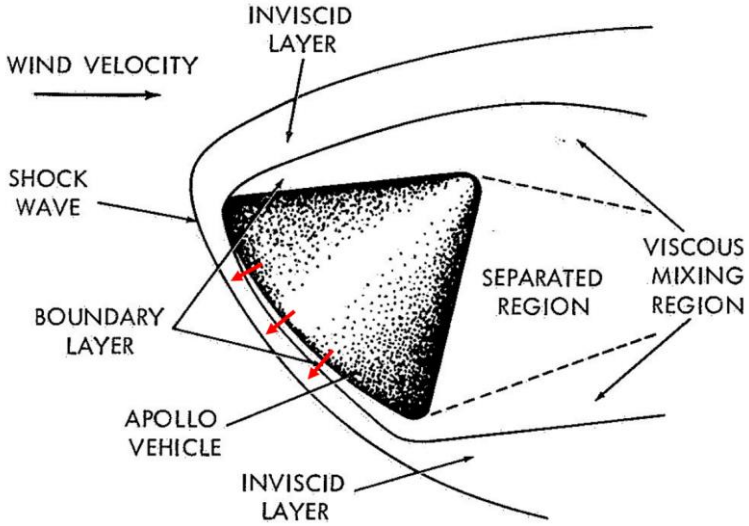

Fig 1.2: Schematic of the gas flow regimes around a blunt body during atmospheric re-entry. The plasma is confined near the shock wave regions. Red arrows indicate the direction of the pyrolysis gas flow.[9]

PART I: PATTERNING OF GRAPHENE USING LOW ENERGY HYDROGEN PLASMA

Chapter 2. Background: Graphene Patterning

The technique of plasma surface nanopatterning of materials has played an important role in the fabrication of semiconductors of ever reducing dimensions over the past several decades. Silicon which has so far been the primary material for manufacturing of transistors has reached its technological limitation with the recent 7 nm scale transistors. Use of novel materials like graphene has been proposed to achieve the next milestone of the 5 nm ITRS node (International Technology Roadmap for Semiconductors).[11] Graphene is one of the lightest and strongest known material with exceptionally high thermal and electrical conductivity.[12,13] However, graphene must be patterned to achieve its full engineering and nanotechnological potential. The selective etching of graphene from its edges to form nanoribbons or the patterning of holes in the basal plane of graphene can open a band gap necessary to achieve graphene transistors.[14–16] In additional to its electronic applications nanoporous graphene membranes are also highly attractive as water filters, gas separators, and can be utilized for fast DNA sequencing and translocation, as well as energy storage.[17–22] Several techniques such as fluorination,[23] boron nitride doping,[24] irradiation by heavy ions,[25] electron beam lithography[26] and etching by hydrogen plasma[27–29] have been used in the past for this purpose. Among these techniques, hydrogen plasma etching has shown the most promise in terms of scalability and cost effectiveness and will be the focus of part I (chapter 2-6) of this dissertation.

In this chapter, we describe the details of prior experimental studies on hydrogen plasma etching on monolayer and multilayer graphene, as well as studies correlating the plasma chamber parameters with the energy of H ions responsible for modifying graphene.

In chapter 3, we use ReaxFF based molecular dynamics (MD) simulations on SiO_2 supported monolayer graphene to establish the contribution of the energetic H ions to the plasma-etching process. We uncover distinct transitions in the etching mechanisms with ion energy which

explain the differing plasma-graphene reactions reported in the experiments. The role of the SiO_2 substrate as well as the interatomic potential is examined.

In chapter 4, MD simulations are performed for plasma etching of multilayer graphene. We uncover energy regimes for ion transmission to achieve targeted etching of the individual graphene layers within the multilayer structure. The etching rates obtained from MD are scaled to experimental length- and time-scales via a mechanistic model which incorporates the added contributions of hydrogen radicals and dehydrogenation effects.

In chapter 5, we examine the role of long time scale effects such as thermal dehydrogenation and their role in plasma etching of graphene. The kinetics of dehydrogenation is calculated by high temperature MD simulations, and compared with previous experimental and theoretical studies.

In chapter 6, we detail the limitations of our atomistic simulations, and discuss possible future directions.

2.1 Overview of Hydrogen Plasma based Graphene Patterning

A typical hydrogen plasma chamber is comprised of an ionizing chamber with a radio frequency (RF) power source, operating at 13.56 MHz (assigned for plasma experiments by the ISM radio bands) into which pure H_2 gas is pumped at low pressure of 0.01-0.03 mbar. The alternating current adds energy to the hydrogen gas, and separates the hydrogen nuclei from the electrons. The cloud of protons and electrons resulting from ionization of hydrogen atoms by the energy source is called hydrogen plasma. Compared to the H ions, the electrons are much lighter, and they reach the graphene sample placed downstream of the ionization chamber faster, as shown in Fig 2.1, this creates a negatively-charged surface resulting in a Langmuir sheath. The H ions are then accelerated towards the negatively-charged surface and bombard the graphene surface as neutral, energetic species.

While there exists ample experimental evidence for the pattering of graphene by hydrogen plasma-treatment, the reported etching reactions and the resulting graphene nanostructures have been vastly different.[27–29] Xie *et al.* observed that a graphene sheet deposited on SiO_2 substrate and placed downstream of an active H_2-plasma chamber undergoes selective

edge etching with no damage to its basal plane.[29] In contrast, Diankov *et al.* and Yang *et al.* both reported combined basal plane and edge etching of graphene by H_2-plasma treatment.[27,28] Regarding the basal plane etching of monolayer graphene, Diankov *et al.* and Yang *et al.* demonstrated isotropic and anisotropic hole growth in the basal plane of graphene respectively, which led to the formation of circular and hexagonal holes. The plasma-graphene etching rates for all three studies were also found to be very different, and ranged from 0.1 to 40 nm/min. To-date, controlling the patterned graphene nanostructures by hydrogen plasma treatment has not been achieved due to a lack of fundamental understanding of the complex hydrogen plasma-graphene chemistry.

Some have proposed that the neutral H radicals, having a density ~ 1,000 times that of the ions, are the primary species responsible for the plasma-graphene etching.[30,31] However, the H radicals alone cannot explain how defects within the initially pristine basal plane of graphene can continuously nucleate, nor can it account for the distinctively different plasma-etched graphene nanostructures reported experimentally. Recent mass spectrometry measurements show that the ions approaching the graphene sample downstream from the discharge can have energies as high as ~ 45 eV, depending on the plasma process conditions.[32] Three possible types of ions (H^+, H_2^+, H_3^+) have been found in the H_2-plasma etching of graphene, with H_3^+ being the most prevalent. Closer to the graphene surface, these energetic ions will undergo dissociative recombination to form neutral, but energetic, H radicals. For example, two possible branching reactions for $H_3^+ + e$ are $H_2 + H$ and 3H.[33,34] The following sections of this chapter describe the details of relevant prior experiments on hydrogen plasma treatment of graphene.

2.2 Monolayer Selectivity of Hydrogen Plasma Treatment

This section summarizes on report by Diankov *et al.* on the reactivity of hydrogen plasma towards monolayer (1LG) and multilayer (MLG) graphene.[27] The graphene sheets were obtained by mechanical cleaving from HOPG using an adhesive tape and were subjected to pre-treatment in a partial oxygen environment to remove any hydrocarbon residue. The influence of the oxidative pre-treatment on the subsequent hydrogen plasma etching was shown to be negligible.

The graphene samples were supported on quartz (SiO_2) substrate and placed downstream of the ionizing chamber at a distance of 30 cm from the discharge. H_2 gas was pumped into the chamber at a rate of 130 sccm and pressure of ~ 400 mTorr. The RF current source used to decompose the H_2 gas into plasma was set to run at 20 W of power and a frequency of 13.56 MHz.

A striking difference was observed in the plasma-etched patterns formed on 1LG compared to MLG. The most visible was the shape of the etch pits which was reported to be circular for 1LG compared to hexagonal for MLG under the same plasma chamber parameters, as shown in Fig 2.2. The circular holes on 1LG were reported to etch at an average rate of 40 nm/min after 10 min of H plasma treatment, based on the radius of the largest intact etch pit. By contrast, the etching rate of MLG was 3 times slower, with the density of holes being ~ 2 orders of magnitude lower. Further, the hexagonal etch pits in MLG appeared to be oriented in the same direction indicating etching rate dependence on crystallographic directions of the graphene lattice. Etching rates for both 1LG and MLG displayed a non-monotonic dependence on substrate temperature, with peak value observed at 300 ℃ as shown in Fig 2.3. The reaction was completely suppressed for temperatures beyond ~ 700 ℃ or below room temperature (25 ℃).

The etching of 1LG was reported to be very sensitive to the distance of the sample from the glow discharge. Moving the sample a mere 1 cm closer (29 cm from the discharge) completely etched away the graphene sheet. Even at the set distance of 30 cm, it was reported that 6 out of 45 1LG samples were complete etched. It is apparent from these finding that the plasma energy window responsible for circular hole formation in 1LG also results in very high etching rate with high sensitivity to ion energy. The Diankov *et al.* observed a large range of etch pit diameters on the 1LG at the end of the 10 min H plasma treatment indicating that the nucleation of etching was occurring continuously and uniformly on the basal plane, and not preferentially at preexisting defects. However, the etch pits were clustered in certain locations on the basal plane, with some regions having much higher density of defects that others. A contrasting observation was reported for MLG where the etch pits were largely uniform in size suggesting that damage nucleates at the start of the plasma treatment at pre-existing defects and not continuously in the basal plane.

Diankov *et al.* also examined the role of the SiO_2 substrate in the etching reactions. The AFM micrographs of the substrate displayed a clear contrast between the reacted (exposed) and unreacted (covered) regions. An apparent relative depression of 0.3-0.5 nm and a cantilever phase lag of 1-5^o was reported for the exposed SiO_2. It was concluded that the substrate was not inert but played an active role in the chemical processes involved in graphene etching. Diankov *et al.* also studied the effect of the crystallinity and surface roughness of SiO_2 on the graphene etching rates[27]. It is conceivable that local roughness can induce a curvature on the graphene sheet and explain the localization of etch pits. To test this hypothesis, the authors repeated the plasma treatment for graphene supported on cleaved muscovite mica which had a surface roughness of 50 ± 15 pm compared to 165 ± 25 pm of the original SiO_2 surface. AFM images of mica supported graphene showed similar phenomena of circular and selective etching in 1LG compared to MLG, suggesting that the substrate roughness plays no role in the reactions of the supported graphene sheets.

The time dependence of etching rate was obtained by in situ measurements of the etch pits size during the plasma treatment. The etching rate for 1LG was observed to be decreasing with time, with an average rate of 80-90 nm/min observed first 30 s which reduced to 40 nm/min by the 3 min mark and remained unchanged till the end of the treatment (10 min), indicating the etching proceeds fasters initially but levels off after ~ 3 min. The dependence of plasma power was studied by performing the experiments at a setting of 10, 20 and 30 W. Etching rate increased monotonically with power with 10, 20 and 30 W settings resulting in a rate of 10 nm/min, 28 nm/min and 80 nm/min in 1LG respectively, after 30 s of exposure. The selectivity of 1LG over MLG remain unchanged with plasma power.

2.3 Selective Edge Etching of Graphene

To achieve the etching of graphene selectively from the edges, Xie *et al.* placed graphene nanoribbons (GNR) on SiO_2 substrates inside a home built remote plasma system at 40 cm from the discharge.[29] H_2 gas was pumped in at a pressure of 300 mTorr, and was ionized using a RF source operating at 13.56 MHz and 20 W of power. The plasma treatment was performed for 60 min and samples were maintained at a temperature of 300 ℃. AFM scans of the treated GNRs

showed selective etching from the edges without any damage to the basal plane. The monolayer GNR reduced in width from ~ 330 nm to ~ 295 nm suggesting an average rate of (over 4 different samples) 0.27 ± 0.05 nm/min while the few layer GNR reduced from ~ 71 nm to ~ 56 nm, suggesting a rate of 0.10 ± 0.03 nm/min. Fig 2.4 shows the AFM micrographs of the GNR before and after the plasma treatment. It is worth noting that while the etching rates observed by Xie *et al.* are several orders of magnitude lower than those reported by Diankov *et al.* In both studies, the etching of monolayer graphene proceeded at ~ 3 times faster than for multilayer graphene.[27,29]

By analyzing the Raman D band of the post treated GNRs, Xie e*t al.* report no hydrogenation of the graphene basal plane. The plasma treatment was also performed at room temperature (25 ℃) as well as 500 ℃ to determine the effects of substrate temperature. In agreement with Diankov *et al*. the etching was shown to proceed at a faster rate at the intermediate temperature of 300 ℃. The authors also hypothesize that the reaction at the edges is nucleated by the formation of C-H chemical bonds which cause the cleaving of the C-C bonds. The further hydrogenation eventually results in the formation of CH_4 molecules.

2.4 Anisotropic Etching in Monolayer Graphene

This section discusses the work of Yang *et al.* who observed anisotropic etching resulting in hexagonal etch pit growth on monolayer graphene.[28] Their findings are in contrast to those of Diankov *et al.* who reported formation of exclusively circular etch pits on the monolayer graphene. The disagreement is most likely due to the difference in the plasma chamber setting adapted by the two studies. Yang *et al.* obtain the monolayer graphene samples from mechanical cleaving of HOPG. The samples were placed on a quartz substrate and inserted inside a homemade plasma setup operating at a frequency of 13.56 MHz and power of 50 W. H_2 gas was pumped into the setup at a rate of 30 sccm and pressure of 350 mTorr. The graphene sample was placed at a distance of ~ 38 cm downstream from the discharge. Plasma etching was performed for a duration of 120 min and the sample was maintained at a temperature of 500 ℃.

The monolayer graphene samples showed distinctly hexagonal etch pits as a result of the plasma treatment. The average etching rate was reported to ~ 6-8 nm/min for monolayer graphene and ~ 2-3 nm/min for bilayer graphene. The ratio of etching rates for monolayer to multilayer (bilayer) graphene is ~ 3:1 which is in agreement with both the work of Diankov *et al.* and Xie *et al.*[27,29] This observation is remarkable because it holds true despite the vast difference in the plasma parameters and etching characteristics observed by the three studies. Another striking similarity between the three studies is the non-monotonous variation in etching rate with substrate temperature. Yang *et al.* show that the etching proceeds most rapidly at an intermediate temperature of ~ 450 ℃ and is largely suppressed for temperatures below 200 ℃ and above 700 ℃. Using in situ measurements the authors calculated the etching rate at various stages of hydrogen treatment and found that the etching rate remains constant throughout the process. This finding is also in agreement with experiments of Diankov *et al.* [27]

Fig 2.5 shows the variation of etching rate with temperature as well as the AFM micrographs of the plasma treated graphene samples at 50 W and 100 W. Deep valleys in the treated graphene seen in the AFM micrographs indicate that the etching occurs preferentially at grain boundaries and line defects, as well as concurrently in the basal plane. The basal plane etching itself likely originates at preexisting point defects. The authors report the presence of methane gas in the plasma chamber which suggest that the etching is due to hydrogenation and volatilization of the C atoms. The etching of the hexagonal etch pits were reported to be H saturated and oriented in the zigzag direction.

2.5 Influence of Plasma Parameters on Ion Energy Distribution

This section discusses the key findings from Felten *et al.*[32] which studied the relationship between input plasma chamber parameters and the H ion energies downstream from the discharge. Felten *et al.* subjected SiO_2 supported monolayer graphene to hydrogen plasma treatment, and varied the plasma power, H_2 gas flow rate, chamber pressure, distance of sample from the discharge as well as the exposure time. They also quantified the composition and ion energy distribution (IED) of H species using energy-filtered mass spectrometry at the various plasma settings. The samples were placed at 3 locations with increasing distance from the

discharge, namely POS1 (inside the discharge), POS2 (20 cm downstream) and POS3 (40 cm downstream).

The intensity of the D band in the Raman spectroscopy was used to calculate the density of defects in the graphene. They observed that the defects increase with exposure time for all setups, which is expected and in agreement with prior experiments. The D band intensity decreased with annealing after mild H plasma treatment, which could be associated with dehydrogenation on graphene. After prolonged treatment, however, a decrease in the D band intensity was no longer apparent which was interpreted to be evidence for the formation of stronger CH_2 and CH_3 bonds, as well as permanent damage associated C-C bond breaking in the graphene sheet. The density of defects in graphene was also observed to increase with plasma power, decrease with distance from the discharge, and decrease with H_2 gas pressure and flow rate. Modifications on the graphene sheet are strongly associated with the energy and type of hydrogen species bombarding the surface. Fig 2.6 shows the IED of H^+, H_2^+ and H_3^+ at POS1 and POS2 at various plasma pressures. The ion energies range from 1-45 eV with the mean ion energy decreasing with increasing distance from the plasma, or with increasing H_2 gas flux and pressure. However, the ion energy increases with plasma power. Along with the energetic hydrogen ions in the plasma chamber, there is also the presence of thermal H radicals which have a density 1000 times that of the H ions inside the discharge; the H radical density in the plasma decreases with increasing distance downstream due to H-H recombination to form H_2 molecules.

Marinov pointed out in a comment on the work of Felten *et al.*, that their graphene samples were electronically floating causing a difference in the ion energy distribution arriving at the graphene samples and their energy filtered mass spectrometry measurements.[35] The reason for the discrepancy is the DC offset and the radio frequency component of the plasma potential. Due to complexities of plasma surface chemistry Marinov remarks that the IED at the floating graphene samples cannot be simple calculated by a constant shift from the IED reported by the mass spectrometer. Nevertheless, they indicate that maximum ion energy for an ion accelerated through a plasma sheath can be written as,

$$E_{max} = \frac{T_e}{2}\ln\left(\frac{M_i}{2\pi m_e}\right) + \frac{T_e}{2} \tag{2.1}$$

Where, T_e is the electron temperature, M_i and m_e are the mass of the ion and electron respectively. For H_3^+ which is the most dominant ion species and for typical plasma chamber settings, $E_{max} \sim 15 - 20$ eV, which is ~ 50 % lower than the values reported by Felten *et al.*

2.6 Figures

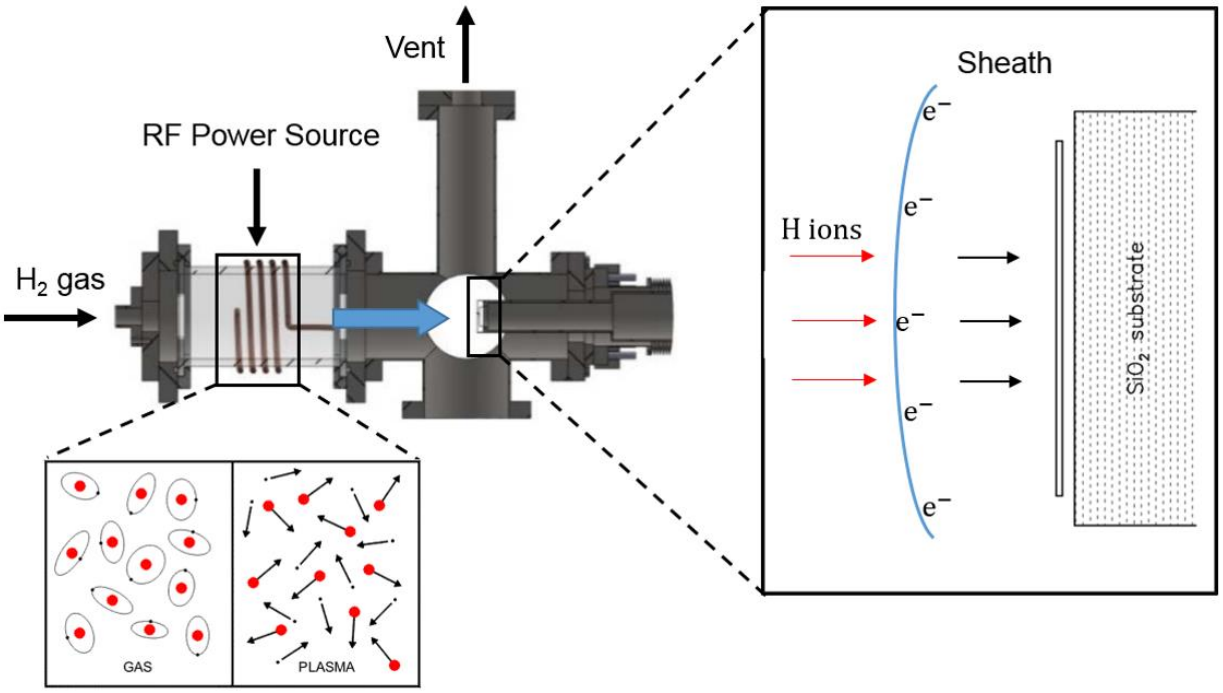

Fig 2.1: Schematic of a typical RF plasma chamber used for etching graphene.[32]

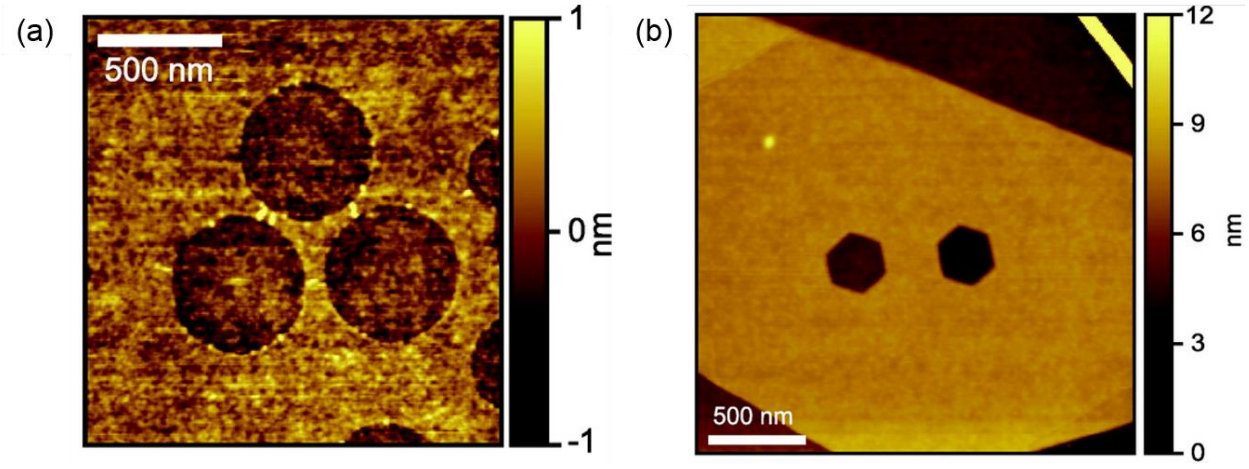

Fig 2.2: Effect of hydrogen treatment on monolayer (a) and multilayer (b) graphene. Note that the etch pits on monolayer graphene are circular while the ones on multilayer graphene are hexagonal. [27]

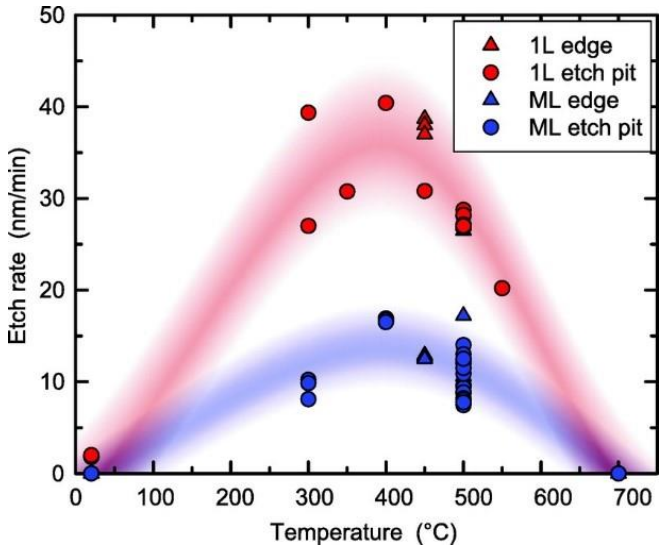

Fig 2.3: Effect of substrate temperature on the etching rate of monolayer (1L) and multilayer (ML) graphene at 10 min of plasma treatment. The etching rate is calculated based on the radius of the largest intact etch pit, as the radius divided by the treatment time. [27]

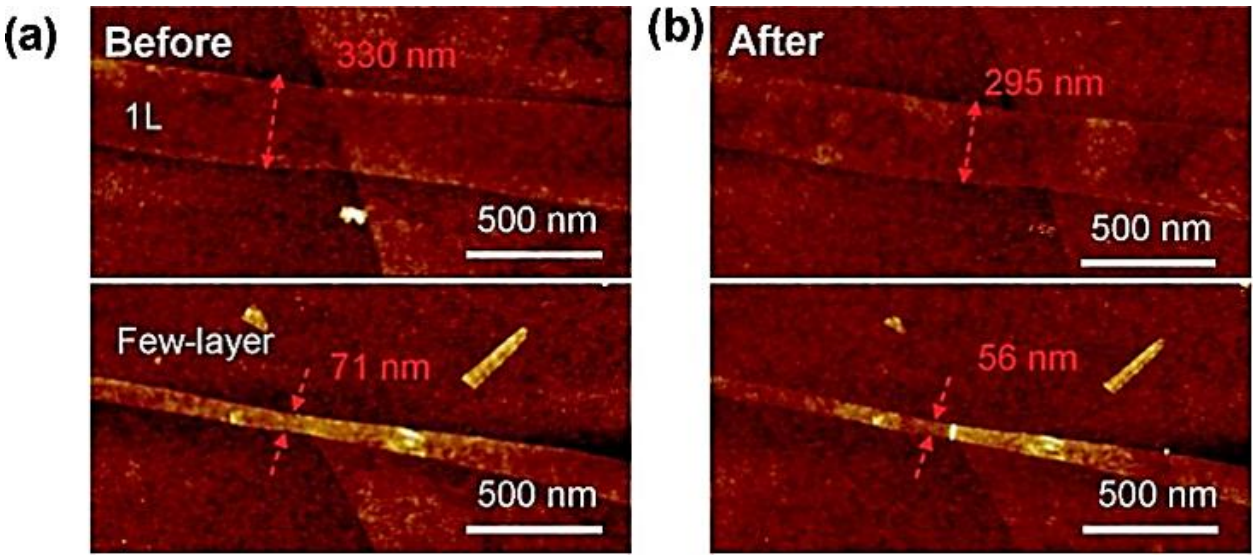

Fig 2.4: Selective etching of graphene from the edges under hydrogen plasma treatment for 60 min at 300 ℃. (a) monolayer and few layer graphene nanoribbons before the plasma treatment are ~ 330 and ~ 71 nm wide respectively. (b) graphene nanoribbons after plasma treatment. The treated monolayer and few layer strips are ~ 295 nm and ~ 56 nm wide respectively.[29]

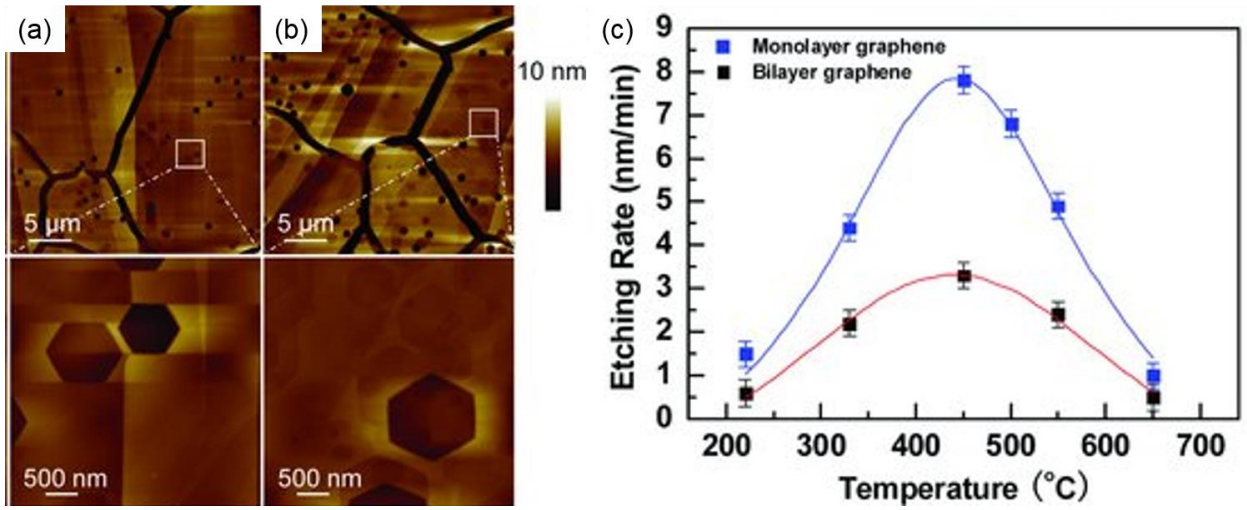

Fig 2.5: Anisotropic etching of monolayer graphene under 50 W (a) and 100 W (b) plasma treatment for 120 min at 500 ℃. (c) Etching rate as a function of substrate temperature for monolayer and bilayer graphene.[28]

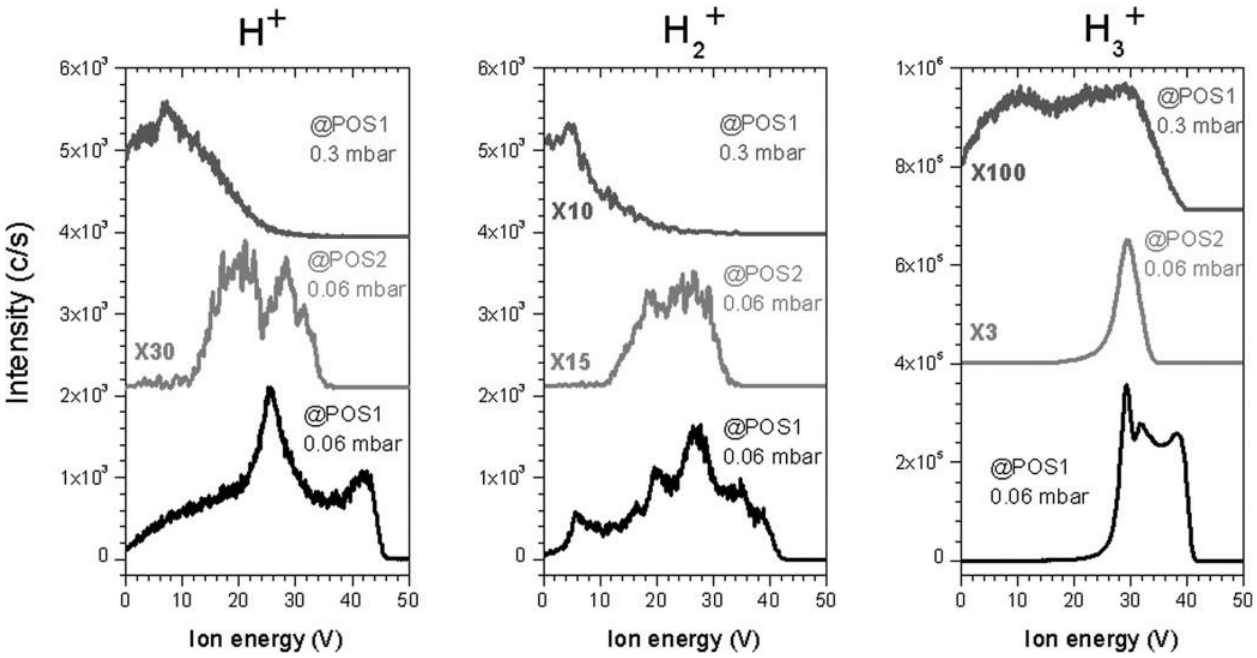

Fig 2.6: Ion energy distribution of various H species inside the plasma chamber at POS1 (inside the discharge) and POS2 (20 cm from the discharge). The energies are measured using energy-filtered mass spectroscopy. [32]

Chapter 3. Patterning of Monolayer Graphene[1]

In this chapter, we establish the contribution of the energetic H ions to the plasma-etching process using large-scale massively parallel molecular dynamics (MD) simulations. We uncover distinct transitions in the etching mechanisms with ion energy which fully explain the differing plasma-graphene reactions reported in the experiments. Based on the MD simulation results, we develop a micromechanics model to predict the hole growth response in monolayer graphene at experimental length- and time-scales, accounting for synergistic effects of both the energetic H ions and the H radicals. In particular, we show that selective edge etching with no damage to the basal plane occurs at ion energies of ~ 1 eV, while nanopores within the graphene basal plane can only stably grow within very narrow ion energy bands of ~ 2 eV for circular holes and ~ 25-30 eV for hexagonal holes. Our results underscore the importance of tuning the plasma process conditions to achieve the desired nanoscale patterns.

3.1 Computational Method

In this subsection we describe the details of the MD simulations used to investigate the etching of graphene via hydrogen plasma treatment. While MD simulations have been used previously to study the interaction of graphene with hydrogen a detailed analysis of energetic H atoms with the SiO_2 supported graphene sheet has not been performed.[31,36] All our simulations are performed using the Large-scale Atomic/Molecular Massively Parallel Simulator (LAMMPS) developed by Sandia National Lab in 1995.[37]

3.1.1 Interatomic Potential

The interatomic interactions between the Si, O, C and H atoms involved in the MD simulations are governed by the ReaxFF potential.[38] The potential allows for bond breaking and formation with a bond order which varies with bond length in a continuous fashion. Additionally,

[1] Some of the results presented in this chapter have been previously published in the following publication: Harpale A., Panesi M. and Chew H.B."Plasma-Graphene Interaction and its Effects on Nanoscale Patterning." *Physical Review B*, 93 (2016): 035416.

the potential consists of bond-order-dependent valance terms, position-dependent change distribution and non-bonded van der Waals and Coulombic interactions between all atoms. The charge on each atom is continuously updated by the Electron Equilibration Method (EEM) in order to maintain a neutral system.[39] As a result, the H atoms impacting the graphene sheet are energetic but charge free. The particular class of ReaxFF function used in our MD simulations was characterized for chemical reactions involving the oxidation of silicon carbide by O_2 and H_2O. It has been shown to accurately capture the reaction dynamics of SiO_2, C/H/O and SiC systems; including graphene hydrogenation and hydrocarbon decomposition.[38] We perform a set of validation studies to ascertain the transferability of the ReaxFF potential for the system of interest. Prior DFT calculations have shown that the barrier energy and formation energy of an H atom chemisorption on the top site of graphene lattice to be ~ 0.5 eV and ~ 1.44 eV, respectively.[31,40,41] Using the ReaxFF potential in the MD framework we reproduce the bonding energy curve by rigidly moving an H atom towards the top site of the graphene lattice iteratively, in increments of 0.1 Å. During each iteration the C atoms in the graphene are minimized using the conjugate gradient method. We obtain an H chemisorption barrier and formation energy to be 0.47 eV and 1.65 eV, in good agreement with prior DFT studies. In its most stable configuration when the H atom is chemically bonded to the C atom graphene, the presence of C-H bond causes a transition in the local hybridization state of the C atom from planar sp^2 to tetragonal sp^3 which is accompanied by distortion of neighboring C-C bonds.[42] Most noticeable the sp^2-to-sp^3 transition causes the C atoms to displace out of plane by 0.35 Å in our simulations, comparable to the DFT reported value of 0.47-0.53 Å as shown in Fig 3.1.[43] Specifically, at the sp^3 hybridized site, our ReaxFF calculations show the C-C and C-H bond length to be 1.50 Å and 1.10 Å respectively, in exact agreement with DFT studies. Further, the C-C-H and C-C-C angle was calculated to be 104^o and 114^o respectively. In excellent agreement with the corresponding DFT reported values of 101^o and 115^o respectively.

Despite the good agreement between the ReaxFF potential and DFT calculation involving chemical properties and hybridization, ReaxFF potentials are inherently limited in their ability to model arbitrarily high velocity impacts between atoms in MD due to inclusion of a shielding term in their van der Waals and coulombic energy terms.[39] The total energy calculated using ReaxFF remains finite even if two atoms overlap. The lack of a hard repulsion means that at sufficiently high impact energy an incident atom can unphysically pass through a target atom

without any transfer of energy. As a result, ReaxFF based ion bombardment MD simulations are limited to a maximum incident energy of E_{max}^{ReaxFF}, even for arbitrarily small simulation time step. The value of E_{max}^{ReaxFF} depends on the type of incident and target atom, as well as the training set used to obtain the ReaxFF parameters. To estimate the value of E_{max}^{ReaxFF} for the system of interest, an H atom is directed head-on towards a C atom in a pristine graphene sheet with kinetics energy of 1-70 eV. The trajectory of the H atom is tracked to determine if it has passed through the C atom. We obtain E_{max}^{ReaxFF} to be $\sim$ 50 eV, which is greater than the H incident energy present in a typical H plasma chamber used for the etching of graphene.[32] For collisions below $\sim$ 50 eV, the momentum exchange between the H and C was seen to be exactly as expected from a perfectly elastic collision. Hence, the lack of the hard repulsion term in ReaxFF potential is not a limitation for the MD simulations performed here. It should be noted that higher energy bombardment simulations are possible but require the ReaxFF functional form to be modified to include a Ziegler-Biersack-Littmark (ZLB) universal repulsive term.[44]

3.1.2 Simulation Setup

Fig 3.2a shows the schematic of the graphene supported on an SiO_2 substrate during the H plasma treatment. We model a 6.8 × 9.8 × 6.1 nm^3 MD simulation box comprising of a 2.1 nm thick α-quartz (SiO_2) crystal, which is oxygen terminated, and with the (001) plane oriented normal to the vertical (*z*) axis. Periodic boundary conditions are enforced in the in-plane dimensions *(x-y)* while fixed boundary conditions are enforced out of plane (*z*). In our simulation of pristine basal plane etching, we model a periodic monolayer graphene sheet on top of SiO_2. The dimensions of the graphene and SiO_2 unit cells are chosen to be 4.26 × 2.459 $Å^2$ and 8.514 × 4.915 × 5.405 $Å^3$, respectively, such that the lattice mismatch in the in-plane direction is negligible ($\sim$ 0.07 % in both x and y dimensions). However, even the tiny mismatch must be eliminated in order to prevent overlap of atoms in the boundary regions of the periodic MD box shown in Fig 3.2b. To achieve this, a slight compression is introduced in the graphene unit cell in order to match the SiO_2 unit cell dimensions.

To delineate the effects of edge etching, we model a 4.2 nm (5.8 nm) wide graphene nanoribbon, which is periodic in the *y (x)* direction and has exposed zigzag (armchair) edges. Each of these SiO_2-graphene systems, with initial configurations depicted in Fig 3.2 b, c and d, is

first subjected to an NVT ensemble at a temperature of 300 ℃, which is maintained by a Berendsen thermostat for 1.5 ps. Upon heating, the pristine graphene sheet shows clear wrinkling which is caused by mismatch between the imposed C-C graphene bond length of 1.42 Å compared to the distance of 1.44 Å resulting from the chosen ReaxFF potential.[38] To quantify the thermal wrinkling of the SiO_2 supported graphene sheet we calculate the surface roughness as the root mean squared deviation of the z coordinate of graphene C atoms to be 1.129 Å, which is good agreement with roughness of 1.35 ± 0.25 Å obtained from AFM scans of monolayer graphene, as reported by Diankov *et al.* [27] The average distance between the C atoms in graphene and the O-terminated surface of the substrate is calculated to be 3.20 Å, which is in close agreement with the value of 2.90 Å from DFT calculations.[45] To simulate isolated slab boundary conditions we rigidly fix the bottom 0.5 nm layer of atoms in the SiO_2 substrate throughout our simulations and designate the next 1.0 nm layer of atoms above this fixed region as the heatbath region, which equilibrates the temperature of the remaining atoms above it.

3.1.3 Hydrogen Deposition Algorithm

We accelerate the plasma-etching simulations by dividing the in-plane dimensions of the simulation box into 3 × 3 grids and simultaneously depositing nine H atoms randomly (one H atom within each cell) from 0.6 nm above the graphene sheet with velocities in the -*z* direction corresponding to kinetic energy of 1-30 eV. Each of these nine impacts are independent of each other, since the impact damage is highly localized due to the small mass of the H atom. Note that the kinetic energy is less than the E_{max}^{ReaxFF} of ~ 50 eV and hence within the allowable range for the ReaxFF potential. After the nine H atoms are deposited, the entire system is equilibrated without a thermostat for the first 6000 iterations (0.9 ps) to resolve the initial impact dynamics. We then switch on the thermostat in the heat-bath region for the next 16,000 iterations (2.4 ps), set to the target temperature of 300 ℃ using a Berendsen thermostat with a temperature damping constant of 7.5 fs, to remove the excess energy introduced by the energetic H atoms. It should be noted that this step simulates the natural process of heat dissipation in a real system where the H impacts are spaced μs apart. Finally, the graphene sheet is quenched to the target temperature of 300 ℃ for a further 2000 iterations (0.3 ps). The entire bombardment cycle is then repeated for the next nine H atom impacts. Any H atoms which are

reflected off the graphene sheet or pass through the 2.1 nm thick SiO_2 substrate to reach the boundaries of the MD simulations box in the z dimension are deleted. We use a fixed time step of 0.15 fs during both the bombardment as well as relaxation phase of the simulations. In a separate set of simulations we verified that the chosen time step of 0.15 fs is sufficiently small to capture the dynamics of H-C collision as well as to model the C-C bonds at the graphene edges up to a temperature of 700 ℃.

Our primary interest is in the etching of the graphene sheet caused by the energetic H atoms, and not by thermal fluctuations of the equilibrium state between the bombardment events. The choice of the 3.6 ps bombardment cycle period allows us to time accelerate the etching process to simulate 1800 H atom impacts (200 bombardment cycles) for each ion energy, which effectively represents a fluence of 2.6×10^{15} ions/cm^2. Etching of graphene nanoribbons at incident energies of 1 eV was continued to a fluence of 4.7×10^{15} ions/cm^2 due to the exceptionally low damage rate. Our simulations on the etching of the armchair (AC) and zigzag (ZZ) edges of the graphene sheet (Fig 3.2c, d) are performed five times for each ion energy, using different H atom random deposition seeds, in order to get sufficient statistics on the damage at the graphene edges.

3.2 Overview of the Effect of H Ion Energy

Fig 3.3 shows distinct transitions in the etching mechanisms with increasing ion energies for a graphene nanoribbon with exposed zigzag edges. At low ion energies of 1 eV, the H atoms can only bind to the edges of the graphene sheet to induce selective edge etching while leaving the basal plane undamaged. At ion energies of 5 eV, a large number of H atoms now bind to the top of the sheet and initiate basal plane etching. The hydrogenation of the top side of the sheet induces sp^2-to-sp^3 transition in hybridization of the C atoms; the sp^3 hybridized bond configuration causes the C atoms to displace 0.35 Å. At high fluence the collective effect induces visible warping of the graphene sheet as seen in Fig 3.3. At higher energies of 10 eV, H atoms have just sufficient energy to penetrate the graphene sheet and are chemisorbed on both sides of the sheet, inducing significant edge and basal plane damage. The graphene sheet remains flat due to the approximately equal rates of hydrogenation of the top and bottom side of the sheet. The

exact hydrogenation rates of the graphene are described in a later section. When the ion energy exceeds 25 eV, most of the H atoms now penetrate the sheet without causing damage and are embedded within the bulk SiO_2 substrate; a small fraction of H atoms which collide with the substrate atoms are reflected back and hydrogenate the bottom of the sheet, causing some basal plane etching.

3.3 Etching of Graphene Basal Plane

We first isolate the contributions of basal plane etching by simulating the energetic ion bombardment of fully periodic monolayer graphene sheets, without exposed edges (Fig 3.2b), supported on the SiO_2 substrate. We quantify the extent of basal plane damage for each ion energy by defining a damage parameter D_b as the fraction of broken C-C bonds in the graphene sheet.

There are several different methods of quantifying the damage in a distorted hexagonal crystal such as centrosymmetric analysis,[46,47] common neighbor analysis,[48] Voronoi analysis,[49] bond angle analysis,[50] neighbor distance analysis,[51] etc. Here, we define the lattice damage parameter D_b as the average coordination number of C atoms in the current MD step, accounting for the reformation of previously broken C-C bonds if the bond distance decreases to below the 1.7 Å cutoff distance (~20% bond stretch); $D_b = 0$ represents an undamaged sheet, while $D_b = 1$ implies full atomization of the graphene sheet with no C-C bonds remaining on the substrate.

The basal plane of graphene remains nearly undamaged ($D_b \sim 0$) at ion energies of 1 eV and 25 eV, but D_b displays a piece-wise linear relationship with the ion fluence ξ for ion energies in-between (Fig 3.4): an initial gentle slope corresponding to the nucleation of defects in the basal plane, followed by an abrupt transition to a much steeper slope at $\xi \sim 1.2 \times 10^{15}$ ions/cm^2 associated with the steady-state propagation of damage from these defect sites. Neglecting the nucleation period, we summarize in Fig 3.5 the steady-state basal plane etching rate per unit area, $\dot{D}_b = \rho\, dD_b/d\xi$, where $\rho = 3.8 \times 10^{15}$cm^{-2} is the area density of C atoms in graphene. Additionally, we subdivide the graphene sheet into four quadrants, and calculate $\dot{D}_b$ within each quadrant to quantify the statistical distribution of damage. Note that $\dot{D}_b$ is a non-

monotonic function of the ion energy: zero at 1 eV and below, peaks at ~ 10 eV, and approaches zero again at 30 eV and beyond, since the graphene sheet becomes completely transparent to the H ions.[52] We estimate that the damage to the basal plane remains negligible up to ion energies of 90-100 eV, beyond which sputtering is expected. However, such energy levels are not present in the low energy plasma treatment of graphene.[32]

We observe that the initiation of basal plane damage requires the chemisorption of H atoms on two closest-neighbor C atoms. In this regard, three C-H bond configurations are possible (Fig 3.6a), depending on whether the neighboring H atoms are both bonded to the top (TT) or bottom (BB) of the sheet, or one H atom on each side (TB). The TT and BB bond configurations are predominant at low ($\leq \sim 5$ eV) or high ion energies ($\geq \sim 20$ eV), while the TB configuration is typical at intermediate ion energy levels (~ 7-15 eV). The chemisorption of H atoms to the basal plane causes sp^2 to sp^3 transitions in the hybridization of the C atoms. An isolated H atom bonded to a C atom causes the neighboring C-C bond to stretch to 1.51-1.53 Å. For C-H bond pairs in the TT or BB configurations (Fig 3.6b-i), the C-C bond distance between these sp^3-hybridized C atoms further stretches to 1.68-1.70 Å, compared to C-C bond length of 1.42 Å for pristine graphene. These observations are comparable to previous DFT calculations.[40] The subsequent influx of H atoms causes the breaking of neighboring C-C bonds (A-B and C-D in Fig 3.6 b-ii and 3.6 b-iii) to form a C_2H_4 bond structure. The rotation of this rigid bond structure, due to its open tetrahedral configuration, causes the breaking of an additional two neighboring C-C bonds (E-F and E-G in Fig 3.6 b-iii). With further influx of H atoms, the C_2H_4 bond structure now separates to form dangling CH_2 and CH_3 groups, and the latter breaks off due to thermal vibrations to release a CH_3 radical (Fig 3.6 b-iv). The etching reaction is more straight-forward for chemisorbed H atoms in the TB configuration, where the C-H bond pairs are on opposite sides of the graphene sheet (Fig 3.6 c-i). The binding of an additional H atom to either one of these sp^3-hybridized C atoms breaks the neighboring C-C bonds in the process. This sp^3-hybridized C atom receives a third H atom from its neighbor to form a dangling CH_3 group (Fig 3.6 c-ii), which subsequently detaches due to thermal vibrations to release a CH_3 radical (Fig 3.6 c-iii). In both reactions, the CH_3 radical will subsequently form CH_4 by combining with the H radicals in the plasma chamber. Our findings are consistent with experiments which report presence of methane (CH_4) in the plasma chamber during hydrogen plasma etching of graphene.[29]

3.4 Hydrogenation of Graphene Basal Plane

Fig 3.7a shows the radial density function (RDF) for the C-H atoms in an H plasma treated graphene sheet. Note that a distinct peak at 1.11 Å indicates that the H atoms indeed form strong chemical bonds with the C atoms in graphene and are not just bound by van der Waals forces. Based on the RDF we use 1.45 Å as the cutoff distance for measuring the number of the chemisorbed H atoms. We determine the extent of TT, BB, and TB bond configurations at various ion energies by calculating the average number of chemisorbed H atoms per C atom at the top and bottom of the graphene sheet, denoted by H_t and H_b respectively. The 'top' and 'bottom' designation of a chemisorbed H atom is based on its relative z coordinate with respect to the C atoms to which it is bonded. We observe that both H_t and H_b increase linearly with ξ across all ion energies. We show the respective C-H bond formation rates defined as, $\dot{H}_t = dH_t/d\xi$ and $\dot{H}_b = dH_b/d\xi$, as well as the overall hydrogenation rate $\dot{H}_t + \dot{H}_b$ in Fig 3.7b. Observe that top-surface hydrogenation dominates at lower ion energies which promotes TT bond configurations, while bottom-surface hydrogenation is more prevalent at higher ion energies resulting in BB bond configurations. Initiation of bottom-surface hydrogenation occurs at ~ 3 eV, which corresponds to the DFT-calculated barrier energy of 2.50-2.86 eV for the penetration of a H atom through a graphene lattice.[43] Even though the overall hydrogenation rate $\dot{H}_t + \dot{H}_b$ peaks at ~ 5 eV, the maximum basal plane etching rate $\dot{D}_b$ occurs at ion energies of 10 eV; this coincides with $\dot{H}_t \approx \dot{H}_b$, which makes the formation of TB bond configurations most likely. Considering that ~ 5 H ions are required to etch off a single C atom in either the TT or BB configuration (Fig 3.6b), compared to ~ 3 H ions for the TB configuration (Fig 3.6c), the etching rates will be ~ 67% higher for the TB configuration, which explains the maximum etching rate at ~ 10 eV.

3.5 Isotropic vs Anisotropic Edge Etching

We next isolate the contributions of edge-etching by simulating the energetic ion bombardment of graphene nanoribbons with exposed zigzag or armchair edges on SiO_2 substrates. We quantify the edge damage parameter D_e as the number of etched C atoms

attributable to the presence of the exposed edges, per unit edge length. The edge region is defined as the narrow strip of graphene within distance d from the boundary atoms. The choice of d will affect the accurate calculation of D_e particularly at large ion fluence. For a strip that is too wide, basal plane etching can be expected within d. For a strip that is too narrow, some of the edge etching contribution will be neglected when damage progresses inwards from the edges beyond d. In order to minimize the error from these factors, we choose $d = 6.4$ Å in all our calculations. Note that D_e is related to the calculation of the basal plane damage parameter D_b within the strip by $D_e = \rho D_b d$. Our simulations show that D_e increases linearly with ξ for all ion energies and does not require an initial damage nucleation period, unlike basal plane etching, since the armchair or zigzag edges are pre-existing defects. However, the calculated edge-etching rates $\dot{D}_e = dD_e/d\xi$ are subjected to statistical variations, which are exacerbated by the short edge lengths modeled in MD. Hence, we perform a total of 5 independent simulations with different random seeds for depositing the H atoms, and obtain a statistical distribution of $\dot{D}_e$ comprising of 10 data points for each ion energy (2 edges on each side of the nanoribbon). We summarize in Fig 3.8 the average zigzag (red) and armchair (blue) edge-etching rates $\dot{D}_e$ as a function of the ion energy. Similar to basal plane etching, we find $\dot{D}_e$ to be highest at 10 eV. However, we continue to observe etching at the armchair and zigzag edges at 1 eV as well as at 30 eV, which suggests that selective edge etching will occur at these ion energies with no damage to the basal plane.

Our results in Fig 3.9 demonstrate distinct ion energy regimes for isotropic versus anisotropic etching. Between 1 and 5 eV, the average armchair and zigzag etching rates are similar with overlapping error bars. At ion energies of between 7 and 30 eV, however, armchair etching consistently proceeds faster than zigzag etching by ~ 15%, suggesting that the patterned holes should indeed be hexagonal (longest to shortest diagonals in a hexagon differ by ~ 15%) with zigzag-oriented edge structures. The shift from isotropic to anisotropic etching with increasing ion energy is explained by examining the damage mechanisms associated with zigzag and armchair etching in Fig 3.9. Etching of the zigzag edges at 1 to 5 eV predominantly occurs by hydrogenation of the edge atoms, which results in the formation and subsequent detachment of CH_3 groups (Fig 3.9a). At ion energies greater than 5 eV, incoming H atoms have sufficient energy to break the weaker inner C-C bonds to form C-H bonds, simultaneously unzipping a

chain of edge C atoms (Fig 3.9b). In contrast, etching of the armchair edges involves some component of momentum-induced breaking of inner C-C bonds at all ion energies (Fig 3.9c), since the higher stability of the triple-bonded C-C edge atoms inhibits direct etching of these atoms by hydrogenation.[53,54] Therefore, there are two competing effects: (a) higher reactivity of the zigzag edge atoms compared to armchair, due to presence of edge states near the fermi level,[55] (b) lower bond dissociation energy of the inner C-C bonds attached to the edge atoms in armchair edge compared to zigzag.[56] At ion energies of 5 eV and below, both these effects compensate each other to cause similar etching rates. At higher ion energies where the effect of (b) dominates, armchair etching proceeds faster than zigzag etching.

3.6 Role of SiO_2 Substrate

3.6.1 Amorphization of Exposed SiO_2

We analyze the role of the SiO_2 substrate supporting the graphene sheet during the H plasma etching simulations. Since our MD simulation use a fully reactive interatomic potential, reactions between Si, O and C, H can be captured. However, although we observe the presence of a small number of H_2O and O_2 molecules generated in the surface regions of the SiO_2 substrate, we do not observe any chemical reactions between the Si, O atoms and the C atoms of the graphene sheet. Our findings are in contrast with previous speculations by Diankov *et al.*, which claim that the substrate does not remain chemically inert but instead actively participates in the chemical reaction of graphene with hydrogen.[27] They base the claim on the observed cantilever phase lag of 1-5^o in the atomic force microscopy (AFM) scans of the covered and exposed regions of the SiO_2 substrate. However, an AFM cantilever phase lag is not necessarily indicative of chemical participation, but can be caused by local change in elastic properties, such as those accompanied by phase change. In our simulations of graphene edge etching (Fig 3.2c, d) we do observe slightly more transition in the SiO_2 atomic structure from a crystalline-to-amorphous in the regions where it is exposed to H plasma. Such a transition is well documented in crystals subjected to bombardment with energetic atoms.[57] Fig 3.10a shows the side view of the SiO_2 substrate after treatment with 13 eV H atoms at a fluence of $\sim 2.6 \times 10^{15}$ ions/cm^2. The

C and H atoms are removed from the MD box and the system by minimized using the conjugate gradient method. Transition from crystalline-to-amorphous phase is seen at greater depths for the SiO_2 in the exposed region than the covered region. The AFM phase image of the SiO_2 substrate post H plasma treatment of the supported graphene sheet is shown in Fig 3.10b.[27] The contrast between the phase in the covered and uncovered regions is in agreement with the crystalline-to-amorphous transition observed in our simulations.

3.6.2 Damage and Hydrogenation of Suspended Graphene

To fully understand the effects of the SiO_2 substrate on the etching and hydrogenation rate of the graphene sheet we perform the bombardment of energetic H atoms on a suspended monolayer graphene. The C atoms in the region near the supercell of the MD box are fixed to prevent the sheet from displacing due to the H impacts. The bombardment cycle is performed as described in section 3.1.3 but now does not require the SiO_2 thermal equilibration phase. It is accelerated to 9 H atoms per 1.2 ps, of which 0.9 ps is the bombardment phase (no thermostat) while the remaining 0.3 ps is relaxation phase (thermostat on graphene). Our results consistently show lower overall hydrogenation rates ($\dot{H}_t + \dot{H}_b$) for the suspended graphene sheet than for the SiO_2 supported graphene (Fig 3.11a). The range of ion energies which cause basal-plane etching ($\dot{D}_b$) is reduced from ~ 2-30 eV to ~ 2-20 eV in the absence of the substrate (Fig 3.11b). Hence, despite no apparent chemical participation, the SiO_2 substrate is responsible for the reflection of some of the more energetic H atoms which penetrate the sheet. The reflected atoms eventually chemisorb to the bottom of the sheet and contribute to the etching process.

3.6.3 H Recombination and Surface Transport

During our simulations we observe that the H atoms which enter the SiO_2 substrate occasionally recombine with each other to form H_2 molecules as shown in Fig 3.12a. Radial distribution function (RDF) analysis for H-H species within the substrate (Fig 3.12b) shows that the fraction of H_2 molecules increases with bombardment energy, indicating greater H-H recombination reaction within the substrate bulk. While the H atoms trapped within the SiO_2 voids are relatively stable and have very low diffusivity,[58,59] the H_2 molecules can diffuse out of the substrate but are inert and do not cause any damage to the graphene sheet. Finally, we remark

that the substrate also plays a vital role in the thermal transport of H radicals along the substrate's surface to hydrogenate the armchair or zigzag edges of the monolayer graphene sheet. ~ 60% of the CH and CH_2 edge-bonds in our H radical simulations are formed in this fashion.

3.7 Atomic-to-Continuum Scale Bridging

Our MD simulations capture the kinetics of early-stage plasma-etching, and have to be scaled to experimentally-relevant length- and time-scales. Ultimately, the hole-growth kinetics will be governed by the synergistic effects of basal plane and edge etching caused by the energetic H ions In order to predict the radius of a circular hole as a function of fluence assume that the radial expansion of the hole of radius from R to $R + dR$ requires the removal of $(\rho 2\pi R)dR$ carbon atoms by combined basal plane and edge etching. Edge etching by the energetic H ions will remove $\left(\dot{D}_e\ 2\pi R\right)d\xi$ carbon atoms, while simultaneously the cumulative basal plane etching contribution will remove $\left(\dot{D}_b\ \xi\ 2\pi R\right)dR$ carbon atoms. Here, we neglect the initial damage nucleation period of $\xi = 1.2 \times 10^{15}\ ions/cm^2$ for basal plane etching, which is short relative to the estimated etching duration of ~ 10^{17} to 10^{18} $\mathrm{ions/cm^2}$.[60]

In addition to the energetic H ions, the neutral H radicals will also contribute to the etching process. The H radicals have an equivalent thermal energy of ~ 0.026 eV at the temperature of 300 ℃, but have a density ~ 1,000 times that of the energetic ions.[30] We have separately exposed zigzag- and armchair-edged monolayer graphene to a relatively high fluence of H radicals of up to 1.2×10^{16} $\mathrm{radicals/cm^2}$. The simulations were performed by randomly inserting H atoms above the graphene/substrate in our simulation box with a kinetic energy of 0.1 eV (velocity in the -*z* direction), and applying the Berendsen thermostat to maintain a temperature of 300 ℃. We observe no hydrogenation of the basal plane of graphene even after the long exposure time. We therefore conclude that the thermal H radicals have insufficient energy to bind with the basal plane, and hence will have limited bearing on basal plane etching prior to substantial hole growth. Assuming an ion to radical density ratio of 1:1000, the chemisorption rate of H radicals at the armchair and zigzag edges of graphene will be orders-of-magnitude higher than that of the energetic ions, causing the exposed edges to be fully

hydrogenated to form CH_2 edge-type bonds. In our repeated simulation runs (5 sets for each edge type), we do not observe any CH_3 bonds forming at the hydrogenated zigzag or armchair edges, nor do we find any C-C bond breaking attributable to the presence of these H radicals. This implies that the thermal radicals at 300 ℃ have insufficient energy to break the respective C-C double or triple bonds for the zigzag and armchair edges. Nevertheless, it is conceivable that these H radicals will hydrogenate and eventually etch off the more unstable dangling bonds created at the edges by the energetic H ions. Assuming that the thermal H radicals will accelerate the edge etching damage caused by the energetic ions by a pre-factor α, we equate the total number of etched C atoms for radial expansion of the hole with the contributions from both basal plane and edge etching to obtain,

$$(\rho 2\pi R)dR = \left(\dot{D}_b\, \xi\, 2\pi R\right)dR + \alpha\left(\dot{D}_e\, 2\pi R\right)d\xi \tag{3.1}$$

rearranging Eqn 3.1 we obtain the integral,

$$R = \int_0^{\xi} \frac{\alpha \dot{D}_e}{\rho - \dot{D}_b\, \xi}\, d\xi \tag{3.2}$$

and consequently,

$$R = -\frac{\alpha \dot{D}_e}{\dot{D}_b}\, ln\left(1 - \frac{\dot{D}_b \xi}{\rho}\right) \tag{3.3}$$

both the basal plane and edge etching rates $(\dot{D}_b, \dot{D}_e)$ for different H ion energies are obtained directly from our MD simulations. However, the pre-factor α is unknown. Here, we estimate α based on the three distinct edge-etching mechanisms identified in Fig 3.9, herein termed as mechanisms 1 to 3. In mechanism 1, the sequential bonding of 3 H atoms leads to the etching of a single zigzag edge C atom. However, the graphene edge atoms will already be CH_2-terminated in the presence of thermal H radicals. Therefore, only a single energetic H atom will be required to etch off the edge C atom, and the actual edge etching rate for mechanism 1 will be $\sim 3\dot{D}_e$, i.e. $\alpha = \sim 3$. In mechanism 2, the breaking of each inner C-C bond attached to double-bonded zigzag edge atoms creates a strip of C atoms. Subsequent bombardment breaks off this strip to from dangling C-C bonds. Considering that the dangling C-C bonds will be etched off by the thermal H radicals, we estimate α for mechanism 2 to range from ~ 5/2 to 8/3. In mechanism 3, the breaking of each inner C-C bond attached to triple-bonded armchair edge atoms creates a

dangling chain of two C atoms which will be etched off by thermal radicals, implying that $\alpha = \sim 3$. For simplicity, we assume $\alpha = 3$ for mechanisms 1 to 3.

Results from this simple model demonstrate narrow ion energy bands of $\leq \sim 2$ eV and $\geq \sim 20$ eV where circular and hexagonal holes, respectively, can stably grow (Fig 3.13). Within the intermediate energy range of ~ 3 to 15 eV, basal plane etching proceeds so rapidly that the sheet simply disintegrates before distinct holes can develop. These results can explain the differing patterned graphene nanostructures in existing experiments (Fig 3.13). Low ion energies of ~ 1 eV are responsible for the selective edge etching of monolayer graphene (Fig 3.14a), as also evidenced by the low plasma power (20 W), and long downstream distance (40 cm) of the graphene sample.[29] At shorter downstream distance (30 cm) from the plasma source (20 W), slightly higher ion energies of ~ 2 eV are expected, which leads to combined edge and basal plane etching; the isotropic etching creates circular holes in the graphene basal plane (Fig 3.14b).[27] Our model further predicts that etching occurs rapidly at 2 eV, and quickly becomes unstable at ~ 3 eV. Interestingly, this is also reflected in the fast 40 nm/min etch rate reported experimentally, as well as the extensive, and at times unstable, basal plane etching seen in parts of the graphene sheet (arrows in Fig 3.14b). In fact, the same study reported complete disintegration of the sheet when shifted ~ 1 cm closer to the plasma source. At higher plasma power (50 W), stable anisotropic etching in the basal plane with rates of 6 nm/min were observed – these etching reactions were likely caused by ion energies of ~ 25 eV, which resulted in zigzag-terminated hexagonal holes (Fig 3.14c).[28]

Our MD simulations are performed at a fixed temperature of 300 ℃ which approximately corresponds to the optimal H_2-plasma etching rate in the experiments.[27–29] We remark that the observation of a maximum reaction rate at a given temperature ($\sim$ 300 ℃ for monolayer graphene) is typical of reactions between gaseous species and hot solid surfaces in which volatile products are formed.[61] Increasing temperature could increase the rate of hydrogen ion/radical recombination into molecules, leading to a suppression of the hydrogen ion/radical density at the graphene sample. Furthermore, the rate of hydrogenation as well as dehydrogenation of graphene is well-known to depend on temperature, which could influence the basal plane and edge-etching rates.[62]

3.8 Summary

Scalable and precise nanopatterning of graphene is an essential step for graphene-based device fabrication. Hydrogen-plasma reactions have been shown to narrow graphene only from the edges, or to selectively produce circular or hexagonal holes in the basal plane of graphene, but the underlying plasma-graphene chemistry is unknown. Here, we studied the hydrogen-plasma etching of monolayer graphene supported on SiO_2 substrates across the range of plasma ion energies using scale-bridging molecular dynamics (MD) simulations based on the reactive force-field potential. Our results uncover distinct etching mechanisms, operative within narrow ion energy windows, which fully explain the differing plasma-graphene reactions observed experimentally. Specific ion energy ranges are demonstrated for stable isotropic ($\sim$ 2 eV) versus anisotropic ($\sim$ 20-30 eV) etching within the basal plane of graphene, as well as for the pure edge etching of graphene ($\sim$ 1 eV). Understanding the complex plasma-graphene chemistry opens up a means for controlled patterning of graphene nanostructures.

3.9 Figures

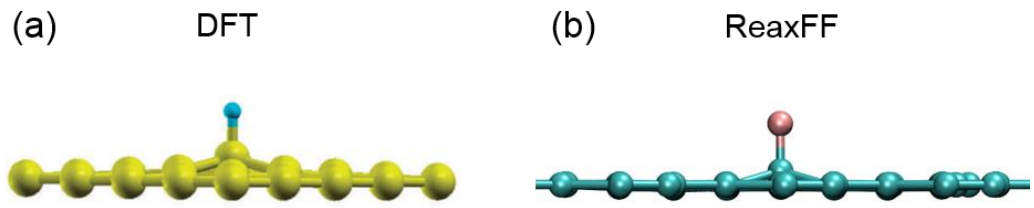

Fig 3.1: Transition in hybridization of graphene C atom from sp^2 to sp^3 due to chemisorbed H. The figure shows the local bonding as obtained from DFT, compared to our ReaxFF based MD simulations. [43]

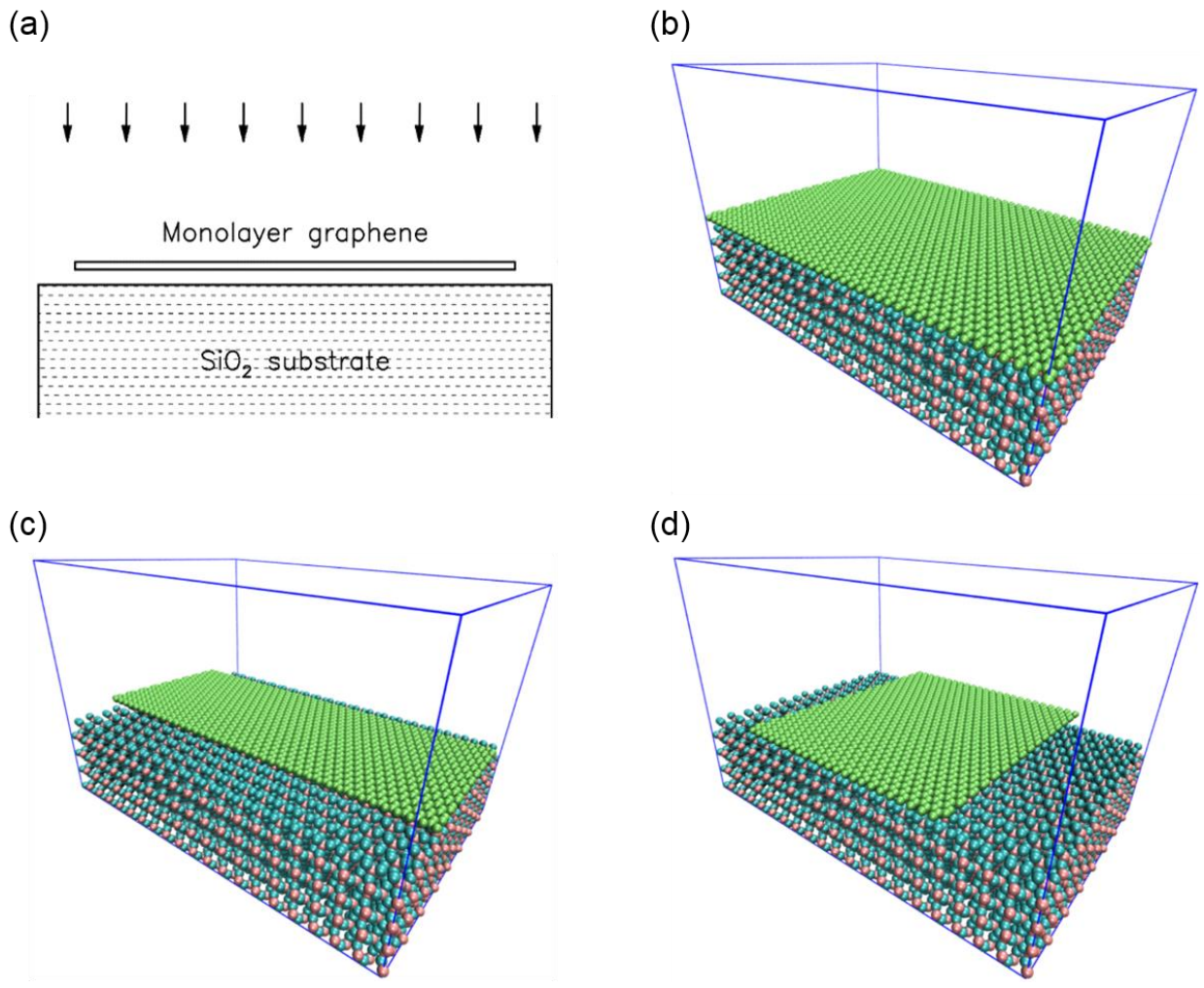

Fig 3.2: (a) Schematic for molecular dynamics modeling of the H plasma etching of monolayer graphene on SiO_2 substrate. Atomic configurations for (b) fully-periodic monolayer graphene without exposed edges, (c) graphene nanoribbon of 4.2 nm width with exposed zigzag edges, and (d) graphene nanoribbon of 5.8 nm width with exposed armchair edges. The C, Si, and O atoms are colored in green, pink, and blue, respectively. The simulation box, outlined in blue, is periodic in the in-plane (x-y) directions.

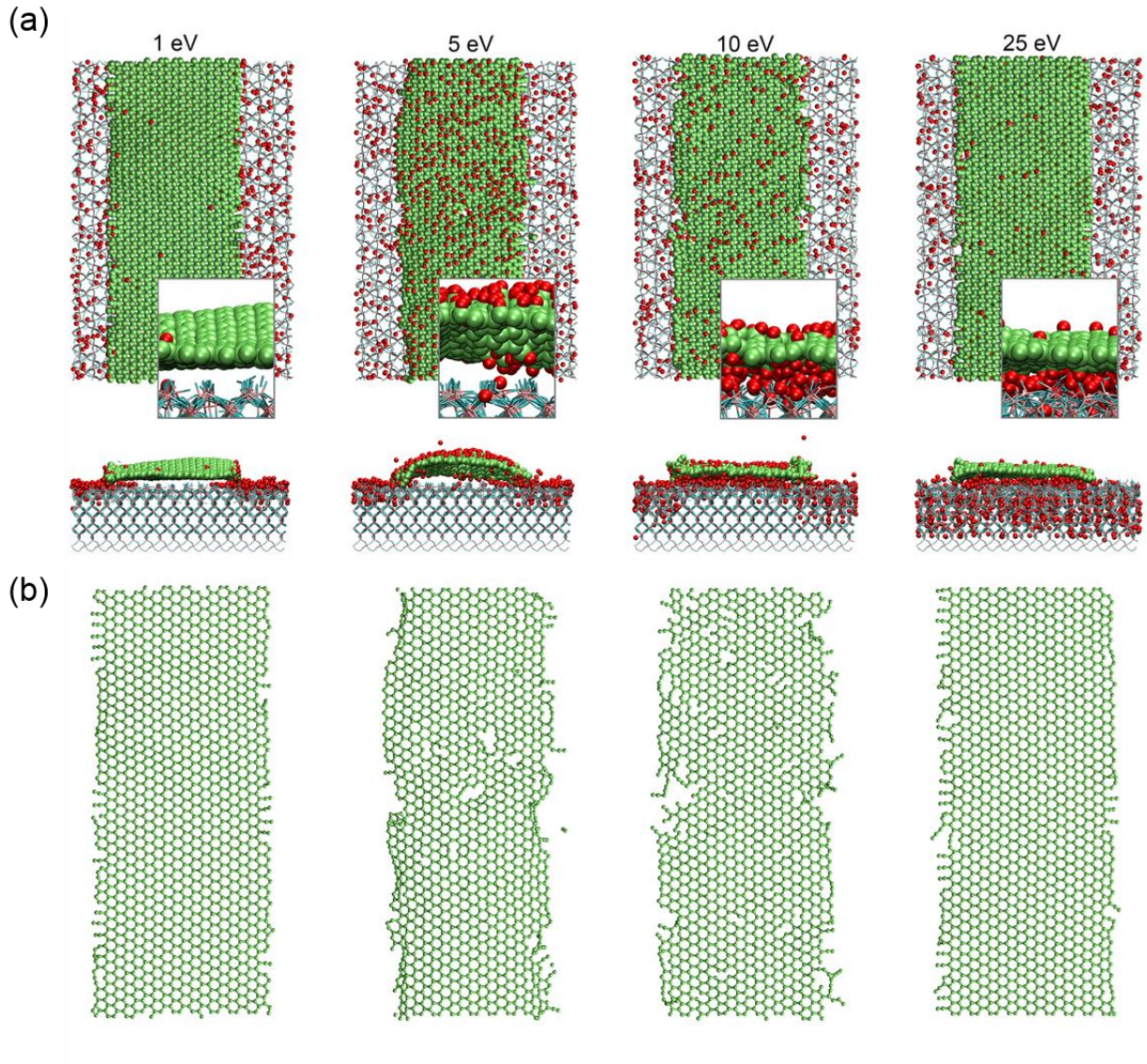

Fig 3.3: Edge and basal plane etching of graphene nanoribbons with exposed zigzag edges. The bombardment of H atoms was carried out at energies of 1, 5, 10, and 25 eV. a, Top and side view atomic configurations at a fluence of 2.1×10^{15} ions/cm^2, with red and green atoms denoting the H and C atoms, and interconnected lines representing SiO_2. Close-up views show the extent of hydrogenation at the top and bottom of each graphene nanoribbon. b, Atomic configurations, corresponding to the snapshots in (a), filtered to display only the C atoms and the C-C bonds of each graphene nanoribbon.

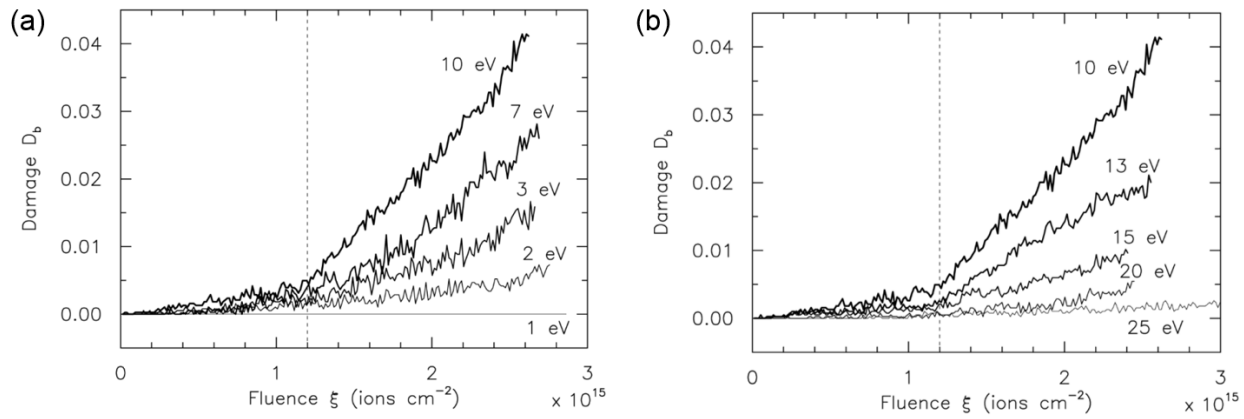

Fig 3.4: Evolution of basal plane damage D_b versus ion fluence ξ for monolayer graphene sheets subjected to ion energies of (a) 1 to 10 eV, and (b) 10 to 25 eV.

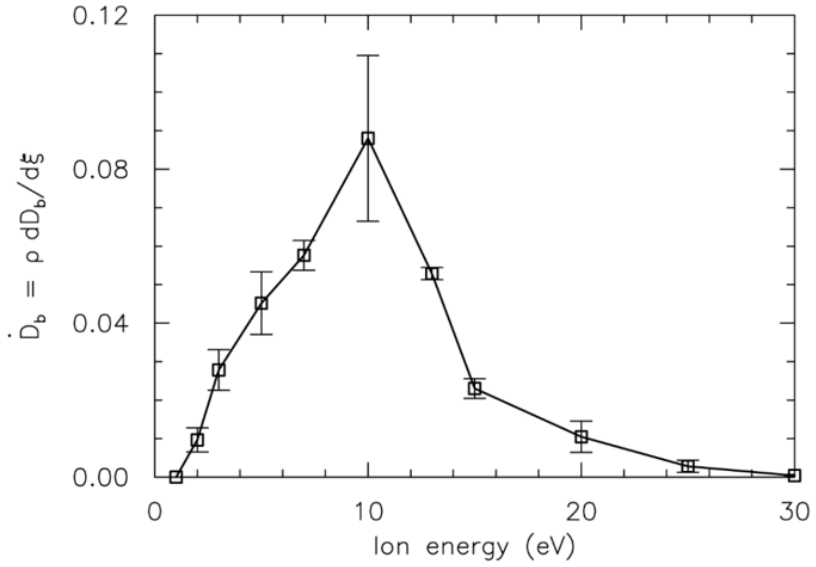

Fig 3.5: Summary of the steady-state basal plane etching rate per unit area, $\dot{D}_b$, versus the ion energy for monolayer graphene sheets. Error bars denote the unbiased standard error.

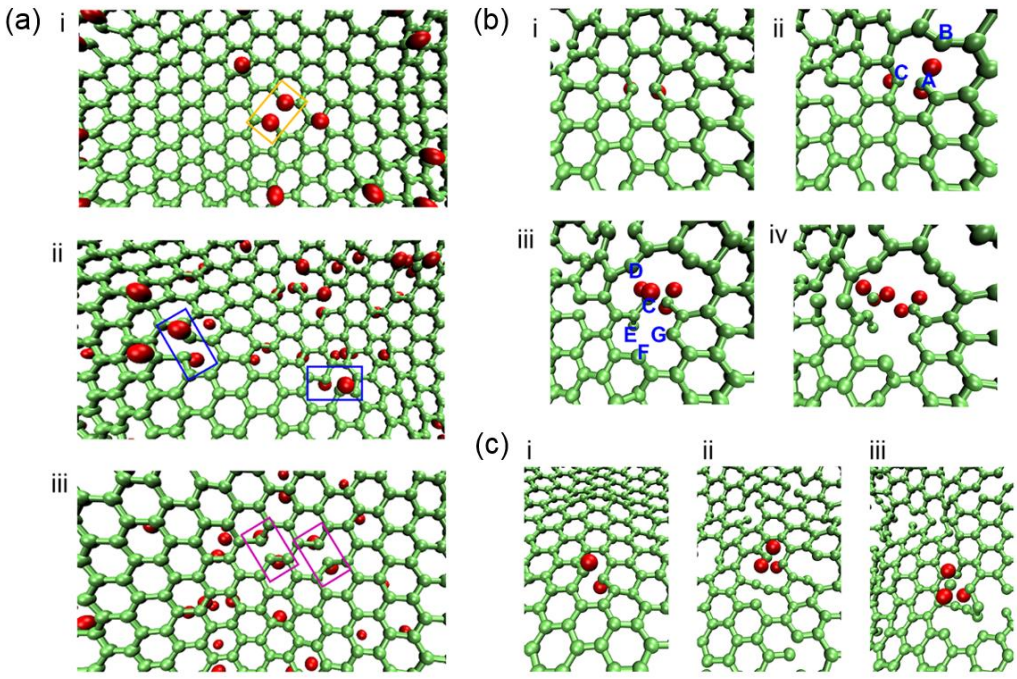

Fig 3.6: Mechanisms of basal plane etching of monolayer graphene sheets. (a) Three possible configurations of C-H bond pairs on closest-neighbor C atoms to nucleate basal plane damage: (a-i) top-top, (a-ii) top-bottom, and (a-iii) bottom-bottom configurations, taken at ion energies of 5, 10 and 15 eV, respectively. (b, c) Perspective views of the basal plane etching mechanisms initiated by the chemisorption of H atoms on a pair of closest-neighbor C atoms to form C-H bond pairs on the same side of the graphene sheet (b), and on opposite sides of the graphene sheet (c).

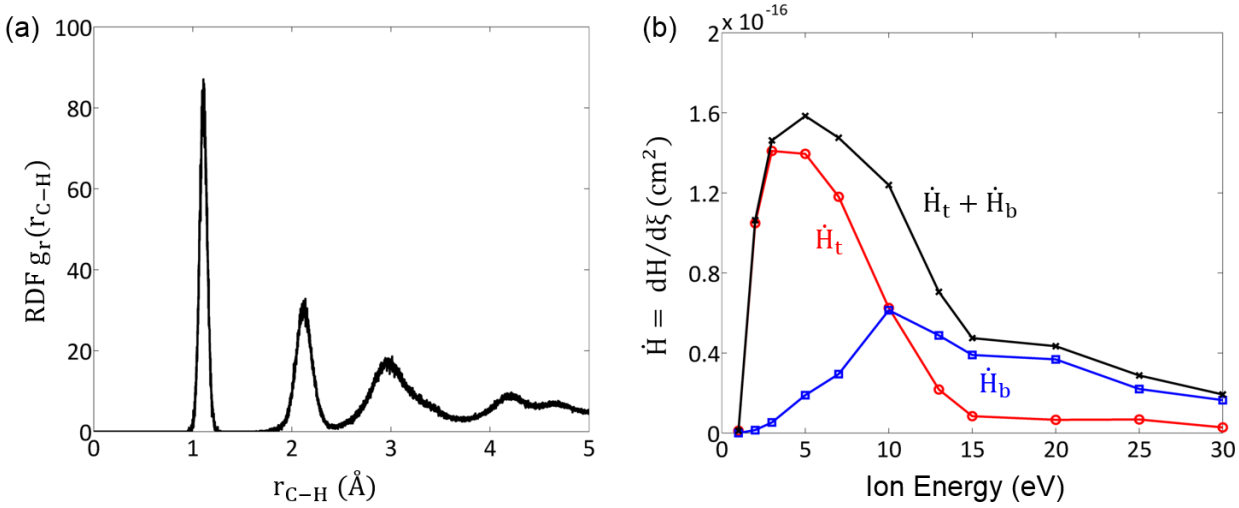

Fig 3.7: Hydrogenation of graphene sheet. (a) Radial distribution function analysis for C-H species after H plasma treatment at 10 eV. (b) Hydrogenation rates, $\dot{H}_t$ and $\dot{H}_b$, at the top and bottom surface of monolayer graphene and their combination, $\dot{H}_t + \dot{H}_b$, versus the ion energy.

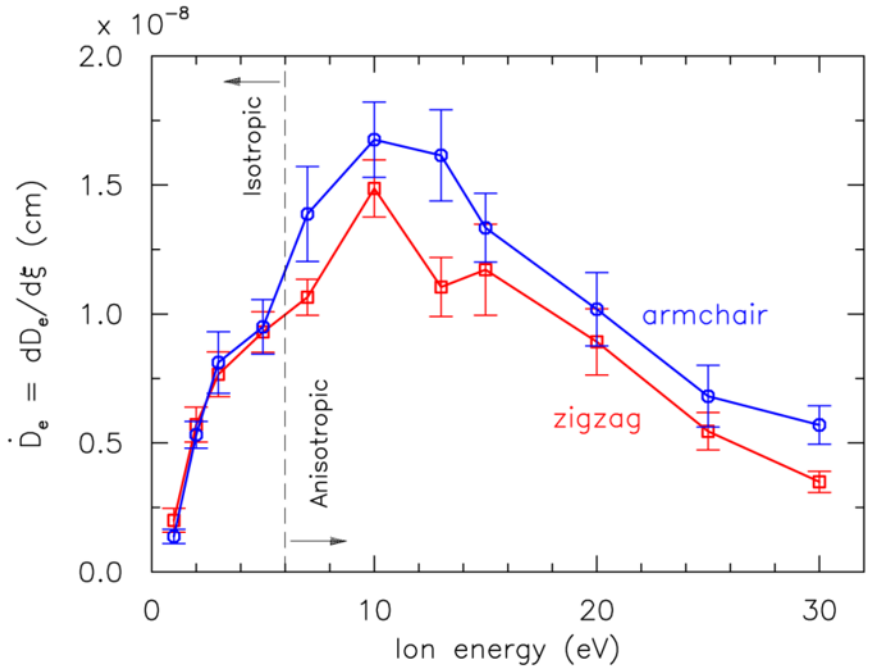

Fig 3.8: Summary of the zigzag and armchair edge etching rates per unit edge length, $\dot{D}_e$, versus the ion energy for graphene nanoribbons. Error bars denote the unbiased standard error.

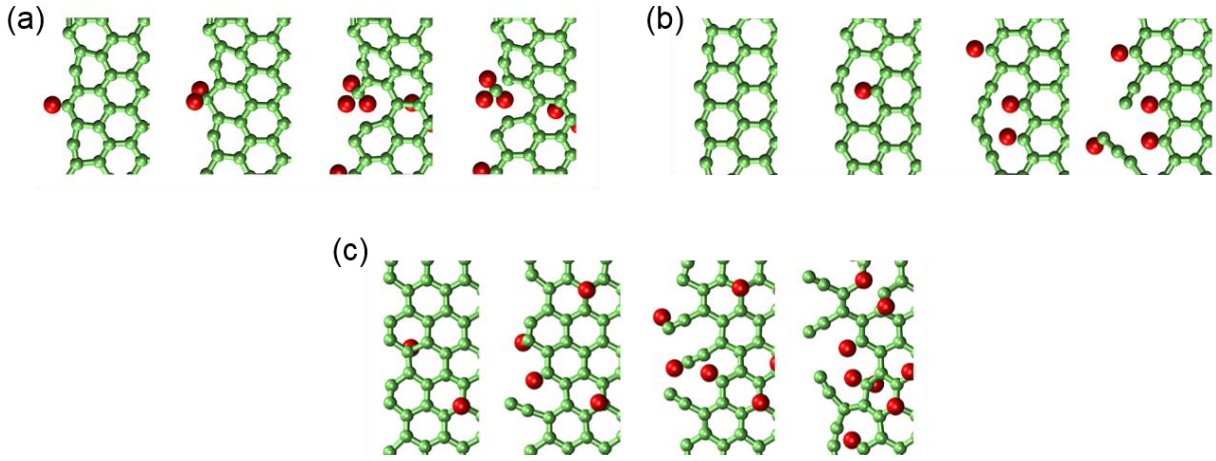

Fig 3.9: Mechanisms of edge-etching of graphene nanoribbons. (a, b) Zigzag edge-etching: (a) formation and detachment of CH_3 by direct hydrogenation of the edge atoms, and (b) unzipping of the double-bonded edge C atoms by breaking of the inner C-C bonds. (c) Armchair edge-etching: breaking of the inner C-C bonds attached to triple-bonded edge atoms.

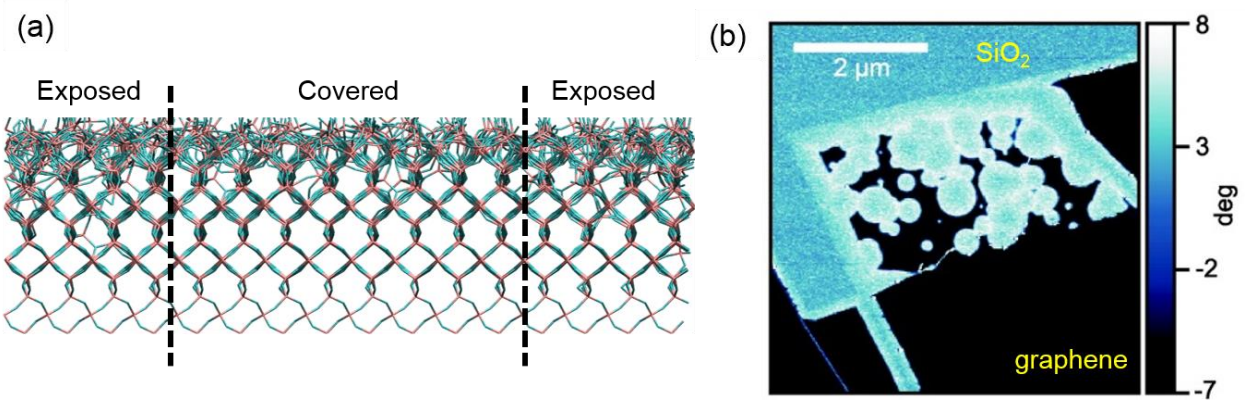

Fig 3.10: Crystalline-to-amorphous transition in the SiO_2 substrate during H plasma treatment (a) Side view of the SiO_2 substrate after treatment of the supported graphene with 13 eV H atoms. The Si and O atoms are minimized using the conjugate gradient methods after the C and H atoms are deleted. The exposed regions show a higher amount of amorphization than the covered region. (b) AFM phase image of the substrate after H plasma treatment.[27] A clear distinction is seen between the covered and exposed regions, with a lower phase angle indicates higher exposure time.

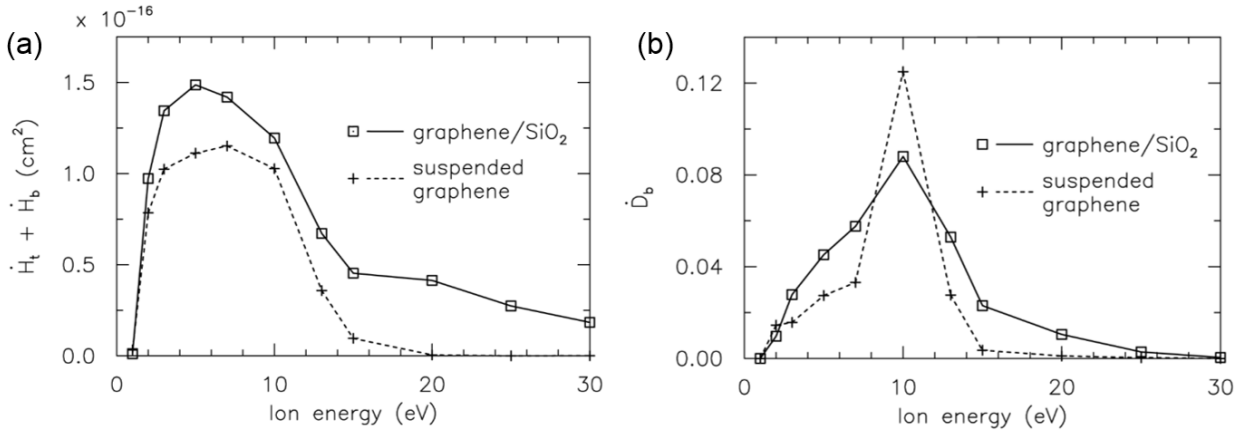

Fig 3.11: Role of the SiO_2 substrate. Comparison of the total hydrogenation rates (a) and the basal plane etching rates (b) between free-standing graphene and graphene supported on SiO_2.

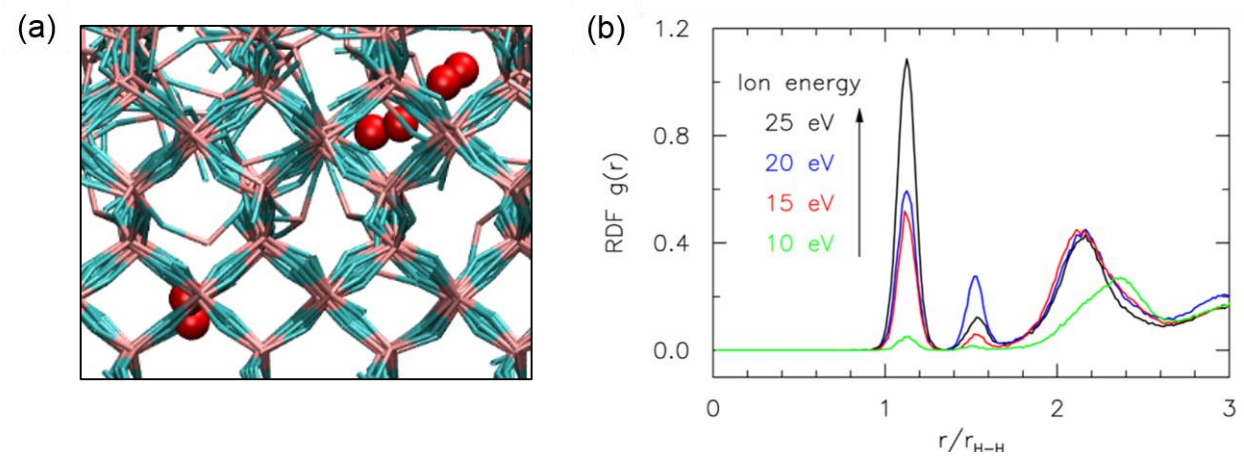

Fig 3.12: (a) H_2 molecules formed by H-H recombination within the SiO_2 substrate (b) Radial distribution function analysis for H-H species within the SiO_2 substrate; the interatomic separation distance r is normalized with respect to the equilibrium bond length of a H_2 molecule $r_{H-H} = 0.741$ Å.

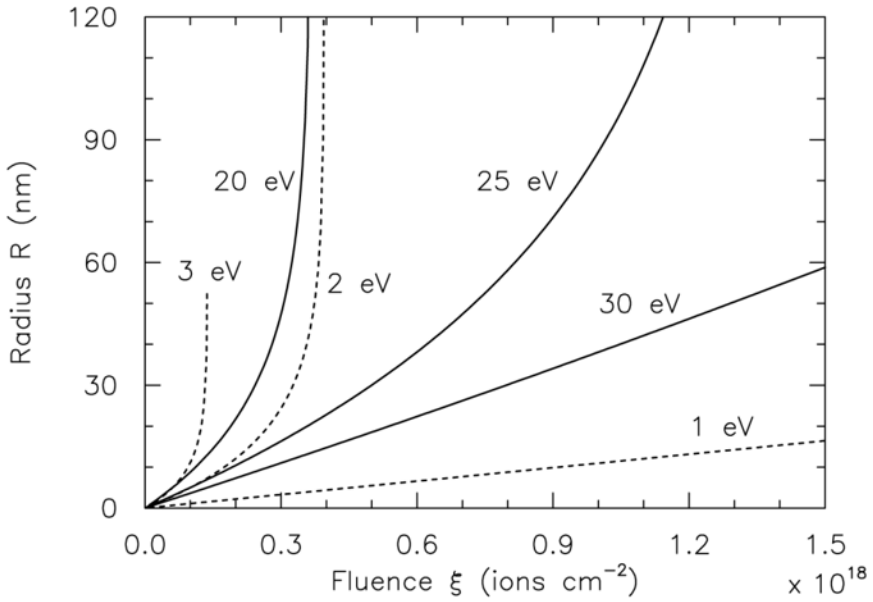

Fig 3.13: Kinetics of hole growth in the graphene basal plane. Hole growth radius R versus the ion fluence ξ caused by combined basal plane and edge etching, accounting for the synergistic effects of H ions and radicals. Isotropic and anisotropic hole growth denoted by dashed and solid lines respectively

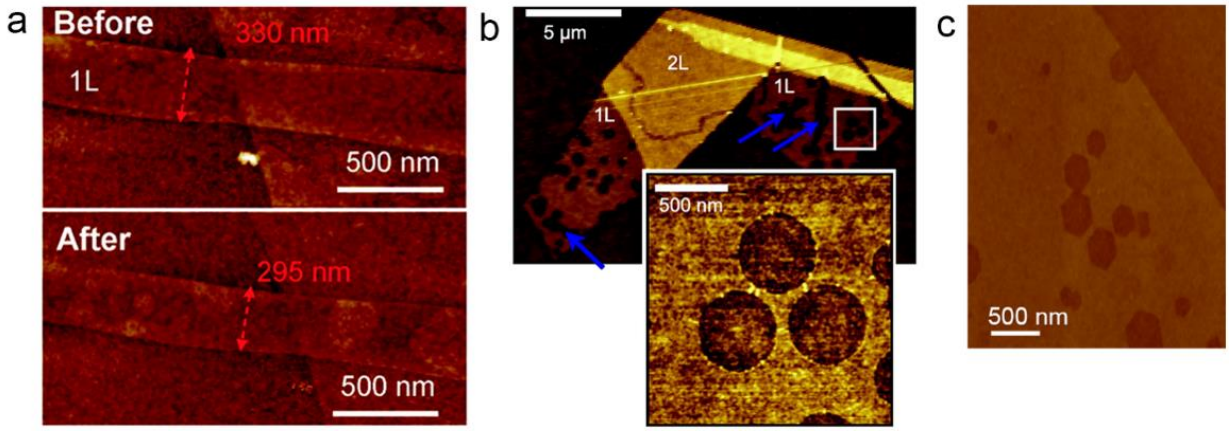

Fig 3.14: AFM topography imaging of three distinct graphene patterns from H_2-plasma etching of monolayer graphene on SiO_2 substrates, reproduced with permission: (a) selective edge etching,[29] and the formation of (b) circular[27] and (c) hexagonal holes[28] in the basal plane, resulting from estimated H ion energies of ~ 1, ~ 2-3, and ~ 25-30 eV, respectively

Chapter 4. Patterning of Multilayer Graphene[2]

We have shown in the previous chapter that three distinct mechanisms are observed in the hydrogen-plasma etching of monolayer graphene: (a) selective narrowing of graphene from the edges with no damage to the basal plane resulting in graphene nanoribbon,[29] and combined edge and basal plane etching to form either (b) circular holes[27] or (c) hexagonal holes[28] in the graphene basal plane. Molecular dynamics (MD) simulations on the hydrogen-plasma etching of monolayer graphene revealed specific H ion energy windows resulting in mechanisms (a)-(c): the ions have sufficient energy to react only with the graphene edges to cause selective edge-etching at low ion energies of ~ 1 eV, but can hydrogenate the basal plane and initiate basal-plane etching at higher ion energies. The simulations also reveal a sharp transition from isotropic to anisotropic edge-etching at ~ 5 eV, which explains the circular or hexagonal hole patterns reported in differing experiments for monolayer graphene. The hydrogen-plasma etching reactions are surprisingly different for multilayer graphene. Some have reported roughening and blister formation on the surface of multilayer graphene but with no visible etch pits.[60] Others have demonstrated 2D patterns of hexagonal columnar holes or 3D patterns of hexagonal stepped-edge holes in the basal plane of multilayer graphene and HOPG.[63] However, the formation of circular holes was never reported for multilayer graphene, even when the experimental conditions were identical to those resulting in circular holes for monolayer graphene. In addition, the edge-etching and hole growth rates for multilayer graphene were approximately three times slower than for monolayer graphene.[27–29]

In this chapter, we study the early-stages of hydrogen-plasma etching of multilayer graphene, across ion energy levels of 2-40 eV, using MD simulations based on reactive force-field (ReaxFF) potential. We uncover energy regimes for ion transmission to achieve targeted etching of the individual graphene layers within the multilayer structure. The etching rates obtained from MD are scaled to experimental length- and time-scales via a mechanistic model which incorporates the added contributions of hydrogen radicals and dehydrogenation effects. Our model predicts a transition in the hole growth pattern from columnar to stepped-edge type, which explains the etching patterns observed experimentally in multilayer graphene.

[2] Some of the results presented in this chapter have been previously published in the following publication: Harpale A. and Chew H.B. "Hydrogen-Plasma Patterning of Multilayer Graphene: Mechanisms and Modeling." *Carbon*, 117 (2017): 82-91

4.1 Computational Method

The plasma-etching of graphene is caused by the energetic bombardment of H^+, H_2^+, and H_3^+ ions with energies of up to ~ 45 eV. Regardless of the ion type, these energetic ions undergo dissociative recombination to form neutral, but energetic, H radicals near the graphene surface. For example, two possible branching reactions for the most prevalent ion type, H_3^+, are $H_3^+ + e \rightarrow H_2 + H$ or 3H.[34] Here, we directly simulate the energetic bombardment of H atoms on quad-layer graphene supported on SiO_2 substrate (Fig 4.1a). As before, our MD simulations are performed using LAMMPS. The atomic interactions between the Si, O, H, and C atoms are fully-governed by a reactive-force-field (ReaxFF) potential which consists of bond-order-dependent valence terms, position-dependent charge distribution, and non-bonded van der Waals and Columbic interactions.[38] This potential allows for continuous bond breaking and reforming, and potential chemical and physical reactions involving the SiO_2 substrate.

4.1.1 Simulation Setup

Our MD simulation box comprises of a 1.1 nm thick α quartz SiO_2 substrate which is oxygen terminated and with the (001) plane oriented normal to the vertical (*z*) axis (Fig 4.1b). We use a 1.1 nm substrate here compared to the 2.1 nm used in the etching of monolayer graphene, in response to our observation of the inertness of SiO_2 in the C, H reactions. Furthermore, due to larger thickness, a multilayer graphene sheet is expected to be a more impenetrable barrier to energetic H atoms, compared to a monolayer sheet, resulting in reduced interaction between the H and SiO_2. An ABA-stacked, quad-layer graphene sheet is modeled above the SiO_2 substrate, and the individual graphene layers are labeled L_1 to L_4 sequentially from the top. Our graphene-SiO_2 system is periodic in the in-plane (*x*-*y*) directions. The 11.1 × 10.8 × 6.1 nm^3 dimensions of the MD simulation box are chosen to minimize the lattice mismatch strain between graphene and SiO_2 (~ 0.07%). The reduction in computational cost afforded by the thinner 1.1 nm SiO_2 substrate, allows us to use a larger graphene sheet compared to the monolayer simulations. We fix the bottom 0.5 nm thick slab of SiO_2 atoms throughout our simulations, and designate the next 0.5 nm thick slab above as the heat bath. All of our simulations are conducted with a time step of 0.15 fs. Prior to initiating the bombardment sequence, we subject the graphene-SiO_2 system to an NVT ensemble maintained at a temperature

of 300 ℃ by a Berendsen thermostat for 1.5 ps; this temperature is typical of plasma-graphene etching experiments. Throughout our simulations, the graphene layers maintain their ABA stacking configurations with interlayer spacing of ~ 0.34 nm which corresponds to that of HOPG.

4.1.2 Hydrogen Deposition Algorithm

We divide the in-plane dimensions of the MD simulation box into a 4 × 4 grid and simultaneously deposit one H atom per cell (16 in total) randomly from 0.6 nm above the top graphene layer L_1; each H atom has initial velocity in the -*z* direction corresponding to kinetic energy of 2 to 40 eV. Because of the relatively large in-plane dimensions of the simulation box, each of the 16 impact locations on the multilayer graphene sheet are sufficiently separated and can be considered as independent events. After initiating this deposition process, we equilibrate the entire system without a thermostat for the first 0.9 ps to resolve the initial impact dynamics. Thereafter, we switch on the thermostat in the heat-bath region and set it to the target temperature of 300 °C for the next 2.4 ps, before quenching the graphene sheet to 300 °C for 0.3 ps. The entire bombardment sequence is then repeated for the next 16 H atom impacts. This choice of the 3.6-ps bombardment cycle period allows us to time accelerate the etching process to simulate over 225 bombardment cycles (3,600 H atom impacts), which effectively represents a fluence of ~ 3.0×10^{15} $\mathrm{ions/cm^2}$. This time-accelerated approach, however, considers only the contribution of energetic H ions to the etching process and cannot account for longer-time-scale events, specifically, the effects of hydrogen radicals and temperature-induced dehydrogenation. These longer time-scale effects will be incorporated in our mechanistic model.

4.2 Surface and Subsurface Basal Plane Etching

Depending on the ion energy, H atoms impinging on each graphene layer L_1 to L_4 can hydrogenate the layer, get transmitted through the layer without causing damage, or get reflected back. Fig 4.2 shows the top and cross-sectional views of the atomic configurations at four ion energies (10, 17, 23, and 28 eV) with a fluence of 1.5×10^{15} ions/cm^2. Our results demonstrate a distinct shift in both the depth and spread of damage with increasing ion energy.

Hydrogenation is confined to both sides of the top graphene layer L_1 at 10 eV, but is shifted to layer L_2 at 17 eV. At even higher energies, damage becomes more diffused and spreads between layers L_2 and L_3 at 23 eV, and across layers L_2 to L_4 at 28 eV with substantial number of H atoms penetrating the SiO_2 substrate.

Fig 4.3a shows the atomic configurations for the respective graphene layers L_1 to L_4 at the ion energy of 17 eV with a fluence of 3.0×10^{15} ions/cm^2, filtered to display only the C-C bonds. Observe that the bulk of the damage is concentrated on layer L_2, with some localized C-C bond breaking in layer L_1. However, the basal planes of layers L_3 and L_4 remain pristine. The etching process in L_1 and L_2 initiates with the chemisorption of H atoms on two closest-neighbor C atoms, akin to that observed for monolayer graphene. This results in three possible C-H bond configurations, as shown in Fig 3b: two neighboring C-H bonds both on the top-side (TT) or bottom-side (BB) of the graphene layer, or one C-H bond on each side (TB). Regardless, the hydrogenation process in all three configurations causes sp^2 to sp^3 transitions in the hybridization of the closest-neighbor C-C bond, and locally stretches the bond. The damage on layer L_2 at 17 eV initiates from all three possible C-H bond configurations (Fig 4.3b), though the TB bond configuration is most prevalent. Below 17 eV, most of the H atoms cannot penetrate layer L_2; any damage on L_2 largely initiates from a TT bond configuration. Above 17 eV, the ions are now transmitted through the layer and a higher percentage hydrogenate the bottom of L_2, initiating damage from a BB bond configuration. Fig 4.3c and d show the typical damage progression from TB and TT (or BB) bond configurations, where continued hydrogenation breaks the sp^3 hybridized C-C bonds to first form CH_2 groups, and later, dangling CH_3 molecules which break-off easily to form CH_3 radicals. These basal-plane etching mechanisms are consistent across all graphene layers and at all ion energy levels.

We trace the effects of ion energy on the progression of damage D_b within the basal plane of graphene layers L_1 to L_4 in Fig 4.4. Here, D_b is defined as the fraction of broken C-C bonds within each graphene layer, using a C-C bond cut-off distance of 1.7 Å which corresponds to 20% maximum bond stretch. Hence, $D_b = 0$ for pristine sp^2-bonded graphene layer, while $D_b = 1$ implies complete disintegration of the graphene layer with no C-C bonds remaining. Observe that D_b has a bilinear relationship with the ion fluence ξ across all graphene layers and at all ion energy levels. The initial gentle slope of D_b with respect to the ion fluence ξ corresponds to the

nucleation of defects on the graphene basal plane. The steeper slope that follows is associated with the steady-state propagation of defects from these damage nucleation sites. The latter is of interest since the ion fluence of 1.2×10^{15} ions/cm^2 for damage nucleation is relatively short compared to the actual fluence of $\sim 5 \times 10^{18}$ ions/cm^2 in typical hydrogen-plasma experiments (flux of 1.5×10^{15}ions/(cm^{2}s) and exposure time of ~ 50 min).[60]

Fig 4.5 summarizes the steady-state damage rate, $\dot{D}_b = \rho \, dD_b/d\xi$, for the respective graphene layers, where $\rho = 3.8 \times 10^{15} \, cm^{-2}$ is the number density of C atoms in pristine monolayer graphene. The error bars denote the distribution of damage within each layer, and are obtained by dividing each graphene layer equally in four quadrants, and calculating the standard error associated with $\dot{D}_b$ within each quadrant. For all four graphene layers, $\dot{D}_b$ is a non-monotonic function of the ion energy which peaks at 10, 17, 23, and 28 eV for layers L_1 to L_4, respectively. At ion energies of $< \sim 10$ eV, hydrogenation is confined to the top layer L_1 and the etching process resembles that of monolayer graphene. At slightly higher ion energies of ~ 13 eV, H atoms now have sufficient energy to penetrate L_1 and cause etching of L_2. At ~ 17 eV, $\dot{D}_b$ now peaks at layer L_2 with 4-folds faster etching rate than L_1, suggesting that selective etching of L_2 occurs at this ion energy. Note that $\dot{D}_b$ becomes more diffused at even higher energies of $\sim$ 25-28 eV, resulting in the concurrent etching of layers L_2 to L_4, each with comparable etching rates. Such high ion energies, however, are still below the required energy levels of 90-100 eV to cause sputtering, and the H atoms are transmitted through layer L_1 without causing damage.

4.3 Analysis of Subsurface Etching Rate

The etching mechanisms for graphene layers L_1 to L_4 are self-similar. Each layer exhibits the same $\dot{D}_b$ profiles, reaching the peak damage at a particular ion energy which is phase-shifted by 5-7 eV with respect to the previous layer. In addition, we observe, from the etching mechanism described above, that the evolution and progression of damage on a particular graphene layer is self-similar for all layers. We verify that the barrier energy of ~ 0.47 eV for C-H bond formation is unchanged across all four graphene layers. Hence, the kinetic energy of the H atoms transmitted through L_1 can be seen effectively as the incident energy for the graphene

sheet comprising of the subsurface layers L_2, L_3, and L_4. By treating each graphene layer as a filter which absorbs some energy from the transmitting H atoms we formulate an equation to determine the etching rate $\dot{D}_{b,i+1}(E)$ from $\dot{D}_{b,i}(E)$. To do so we perform a separate set of simulations with a suspended monolayer graphene sheet to determine the influence of a single layer on the kinetic energy of H atoms.

4.3.1 H Ion Transmission, Reflection and Chemisorption

Consider a H ion incident normally on the graphene surface with initial energy E_0. The transmission of this energetic ion through the graphene lattice changes both the ion's kinetic energy, E_T, and polar angle of its velocity, θ_T. In a multilayer structure, the ion subsequently impacts the next graphene layer with this new incident energy E_T and off-normal polar angle θ_T. We perform a series of H atom bombardment simulations on a single graphene layer to establish the relationship between E_0 versus (E_T, θ_T). We model a 11.1 × 10.8 × 6.1 nm^3 MD simulation box which is periodic in the in-plane (*x*-*y*) directions. The graphene layer is equilibrated at the temperature of 300 °C, and is supported by a reflective wall which is transparent to H atoms and will not influence the transmission dynamics. A H atom is inserted 3.0 nm above the graphene layer with randomly chosen x,y coordinates, and initial velocity in the normal (–*z*) direction corresponding to the incident kinetic energy E_0 of 2 eV to 40 eV. The position and velocity of the H atom is tracked for 0.7 ps as it impacts the graphene layer. Based on its *z* coordinate the H atom is classified as either transmitted, reflected or absorbed and its kinetic energy is recorded. It is then deleted from the simulation box the process is repeated for 2,000 H atoms to obtain the transmitted ion energy and angular distributions, $f_T(E_T; E_0)$ and $f_\theta(\theta_T; E_0)$, respectively.

The $f_T(E_T; E_0)$ and $f_\theta(\theta_T; E_0)$ distributions in Fig 4.6a and 4.6b are obtained by applying a kernel-smoothing on the histogram using the optimal bandwidth and a normal kernel. The curves are normalized such that the area under each curve equals the transmission probability of an ion with energy E_0 through the graphene layer. The mean values of the transmitted ion energy $\bar{E}_T$ and polar angle $\bar{\theta}_T$ are shown in Fig 4.6c and 4.6d respectively, with the error bars denoting the standard deviation σ of the sample. Note that $\bar{E}_T \sim 0$ when H ions have just sufficient energy to penetrate the graphene layer at $E_0 = 10\ eV$. At higher energies, $\bar{E}_T$ linearly scales with E_0, with comparable distribution width (σ) across all E_0. On the other hand,

the transmitted ions have a high $\bar{\theta}_T$ of $\sim 40°$ with significant scatter in the data ($\sigma \pm 20°$) at $E_0 = 10$ eV, which decays to $\sim 20°$ with $\sigma \pm 10°$ beyond $E_0 > 20$ eV. During the plasma treatment of multilayer graphene these transmitted ions impact the next graphene layer with the off-normal polar angle θ_T. Hence, we study the effects of the incident polar angle θ on the probability of chemisorption, transmission, or reflection of the energetic ion. Our results (Fig 4.7) show that off-normal polar angles of $\theta \leq 20°$ have no influence on the chemisorption, transmission, or reflection probabilities across all ion energies. For $\theta > 30°$, however, the chemisorption probabilities for $E_0 \leq 10$ eV and transmission probabilities for $E_0 > 10$ eV are significantly reduced, resulting in a corresponding increase in the reflection probabilities.

4.3.2 Formulation and results

The basal plane etching rate of the L_{i+1} layer, $\dot{D}_{b,i+1}$, can be traced from that of the L_i layer, $\dot{D}_{\mathrm{b,i}}$, knowing both the transmitted ion energy and polar angle distributions, f_{T} and f_{θ} (Fig 4.8). Hence, $\dot{D}_{\mathrm{b,2}}$, $\dot{D}_{\mathrm{b,3}}$, …… $\dot{D}_{\mathrm{b,n}}$ of an n-layer graphene sheet can be iteratively traced from the etching rate of the top layer, $\dot{D}_{\mathrm{b,1}}$, obtained from MD simulations. For simplicity, we consider only the effects of change in ion energy $f_{\mathrm{T}}(E_{\mathrm{T}}; E_0)$, and introduce an empirical prefactor γ to account for off-normal incident angle:

$$\dot{D}_{b,i+1}(E_o) = \gamma \int_0^{\infty} \dot{D}_{b,i}(E)\, f_T(E; E_o)\, dE \tag{4.1}$$

The blue curves in Fig 4.8 are the projected damage rates for $\dot{D}_{\mathrm{b,2}}$ to $\dot{D}_{\mathrm{b,4}}$ in layers L_2 to L_4, neglecting off-normal angular effects of the ions ($\gamma = 1$). Compared to the MD-measured $\dot{D}_{\mathrm{b}}$ values denoted by open symbols, the projected results are in very good agreement in the post-peak regime for all three layers L_2 to L_4, but consistently over-predicts $\dot{D}_{\mathrm{b}}$ in the pre-peak regime; the extent of over prediction increases from layers L_2 to L_4 and is attributed to off-normal angular effects. Prior to impacting the i^{th} graphene layer, ions in the pre-peak regime of $\dot{D}_{\mathrm{b,i}}$ have ion energies of ≤ 10 eV with estimated off-normal polar angles of up to $\bar{\theta}_{\mathrm{T}} + \sigma \sim 60°$ (Fig 4.7d). As shown in Fig 4.7a, off-normal polar angles $> 30°$ will significantly reduce the chemisorption probability in this pre-peak ion energy regime, which explains the observed deviation in the projected results in Fig 8. In contrast, the more energetic ions (> 10 eV) in the

post-peak regime have off-normal polar angles of $< 30°$ (Fig 4.7d), which have limited effect on the absorption and transmission probabilities (Fig 4.7). We correct for this over-estimation in the projection of $\dot{D}_{b,2}$ for graphene layer L_2 by setting $\gamma = 0.55$ for the pre-peak regime and $\gamma = 1$ in the post-peak regime, as shown by the red curve in Fig 4.8. Using the same values of γ for the subsequent layers, we find the corrected projections in layers L_3 and L_4 in Fig 4.8b and 4.8c to also be in good agreement with MD predictions, which confirms that the angular effects are self-similar.

4.3.3 Discussion

We derived an equation to calculate the basal plane etching rate of layer L_{i+1} layer, $\dot{D}_{b,i+1}$, from the L_i layer etching rate, $\dot{D}_{b,i}$. We assumed individual graphene layers to interact with the H atoms separately without interlayer effects. The equation is used iteratively to obtain the basal plane damage rate $\dot{D}_{b,2}$, $\dot{D}_{b,3}$ and $\dot{D}_{b,4}$ from $\dot{D}_{b,1}$ and compared with the MD calculated values. The prefactor γ is required to adjust for the reduced damage caused by the off normal incident on the subsurface layers. We fit the curve for $\dot{D}_{b,2}(E)$ with MD derived value to obtain,

$$\gamma = \begin{matrix} 0.55\ for\ E \leq E_{peak} \\ 1\ for\ E > E_{peak} \end{matrix} \tag{4.2}$$

The assumptions in the derivation of this equation are as follows:

- The energy damping effects of a single graphene layer does not change with hydrogenation or damage in that layer. The calculation of $f_T(E_T; E_0)$ and $f_\theta(\theta_T; E_0)$ involves a graphene sheet which remain pristine throughout the simulations.
- The effect of the wrinkling of the graphene sheet is negligible.
- H radicals which are trapped in the graphene interlayer regions, but not chemisorbed on the sheet, do not interfere with the etching reaction.
- The effects of long time scale thermal processes are negligible.
- The effects of H atoms reflecting back from the graphene layers neighboring to the target layer is negligible.

- The damage rate is an additive function of the ion energy. For instance, if the H atoms have energy of E_1 and E_2 with equal probability, the damage rate should be $\left(\dot{D}_b(E_1) + \dot{D}_b(E_2)\right)/2$.

4.4 Surface and Subsurface Hydrogenation

H atoms impinging on the multilayer graphene sheet either chemisorb on the top or bottom side of one of the layers or become intercalated between graphene layers as thermal H radicals. To quantify the extent of hydrogenation of the graphene layers, we define H_t and H_b as the number of chemisorbed H atoms per C atom on the top and bottom side of each graphene layer (C-H bonds cutoff of 1.45 Å) respectively. We observe that similar to monolayer graphene, the value of H_t and H_b increases linearly with ξ for each layer. Fig 4.9 shows the hydrogenation rates as $\dot{H}_t = dH_t/d\xi$ and $\dot{H}_b = dH_b/d\xi$ as a function of ion energy for the four layers. The hydrogenation on layers L_1 occurs at equal rates on its top and bottom sides ($\dot{H}_t \approx \dot{H}_b$) at energy of 10 eV which corresponds to its maximum basal plane damage rate. However, in the subsurface layers we consistently observe $\dot{H}_t > \dot{H}_b$ at peak basal plane damage energies of 17 eV, 23eV and 28eV for L_2, L_3 and L_4 respectively. A fraction of the H atoms which are chemisorbed to the top side of the subsurface layers are removed before they can contribute to graphene etching. To quantify this phenomena we define a dehydrogenation parameter for top and bottom side each layer DH_t and DH_b respectively, as the cumulative number of C-H bonds broken per C atoms. Note that H_t and H_b represent the current number of C-H bonds on the graphene layer which DH_t and DH_b are the cumulative number of bonds broken after being formation at a given fluence. We observe that DH_t and DH_b also increase linearly with ξ at all the layers. We define their rates as $D\dot{H}_t = dDH_t/d\xi$ and $D\dot{H}_b = dDH_b/d\xi$, which are shown in Fig 4.9. For subsurface layers there is significant dehydrogenation on the top side for lower effective ion energies (large $D\dot{H}_t$). The constant removal of chemisorbed H atoms explains the trend of $\dot{H}_t > \dot{H}_b$ at peak damage energies in subsurface layers ($L_2 - L_4$).

4.5 Blister Formation and Interlayer H-H Recombination

In addition to the hexagonal hole patterns observed in experiments on multilayer graphene (Fig 4.10c), corrugated patterns of ripples and valleys with low density of surface defects were reported for HOPG after hydrogen plasma exposure (Fig 4.10a), with measured ion-surface impact energies of ~ 12.6 eV.[60] Interestingly, we observe similar surface blisters for our multilayer graphene structures at comparable ion energy levels. Fig 4.10b shows the underside of layer L_1 subjected to ion energy of 15 eV at a fluence of 3.0×10^{15} ions/cm^2; the atoms are colored by the relative atomic displacements in the out-of-plane (z) direction, and the H_2 molecules sandwiched between layers L_1 and L_2 are shown in red. Observe that the surface blister patterns (colored in blue) closely correlates with the clusters of H_2 molecules. These H_2 molecules are formed not from thermal-desorption processes which are beyond the MD time-scale, but from intercalated H radicals, trapped between layers L_1 and L_2, interacting with chemisorbed H atoms via the Eley-Rideal recombination mechanism.[64] Fig 4.10c shows H desorption caused by the combination of an intercalated H radical (labeled R) with a chemisorbed H atom in a TB configuration on layer L_2, and the formation of a H_2 molecule. The experiments reported that the blisters gradually diminished during port treatment annealing, presumably due to the H_2 gas diffusing out though the edges of the multilayer graphene sheet. We calculate the number of H_2 molecules in the interlayer regions and observes that they increase linearly with fluence. Bombardment with 15 eV H atoms results in the peak H_2 formation rate of 4.4×10^{14} cm^{-2} at the end of the simulation, in reasonable agreement with previous estimate of 2.8×10^{14} cm^{-2} by Waqar *et al.*[65]

4.6 Multilayer Edge Etching

Once sufficient localized basal-plane etching occurs to form well-defined holes in the graphene layers, damage then progresses more rapidly from the hole edges. Depending on the ion energy, holes could develop on the exposed surface or the subsurface interior layers of multilayer graphene. To quantify the zigzag and armchair edge-etching rates of both these configurations, we perform H atom bombardment simulations on a tri-layer graphene structure,

comprising of graphene nanoribbons either at the top of (L_1), or sandwiched between (L_2), two fully-periodic graphene layers. For both these L_1 and L_2 configurations, the exposed edges of the graphene nanoribbon are oriented in either the zigzag or armchair configuration. The periodic MD simulation boxes of these four model configurations are shown in Fig 4.11a. To reduce the computational cost, the tri-layer graphene structure is supported by a 6-12 LJ wall (black outline in Fig 4.11a), in-place of SiO_2, with the parameters $\sigma_{LJ} = 0.253\ nm$ and $\epsilon_{LJ} = 0.408\ kcal/mol$. We carry out the H atom bombardment sequence using the same procedure outlined in section 4.1.2.

To quantify the edge-etching rate, we define the damage parameter D_e as the number of broken C-C bonds per unit edge-length, within a distance of $d = 0.8$ nm from the zigzag or armchair edges. Note that $D_e = \rho D_b d$ within the edge region. Unlike the bilinear relationship between D_b and the ion fluence ξ in Fig 4.11, we observe that D_e increases linearly with ξ without requiring a nucleation period, since hydrogenation occurs readily with the graphene edges. Due to the relatively small number of edge C atoms in our MD box, we perform 5 sets of independent simulation runs using different deposition seeds. The average armchair and zigzag edge-etching rates $\dot{D}_e = dD_e/d\xi$ are shown in Fig 4.11b and 4.11c for nanoribbons in the L_1 or L_2 configurations respectively, with error bars denoting the standard error. Interestingly, the armchair and zigzag etching rates for nanoribbons in either the L_1 or L_2 configurations are almost equal, with overlapping error bars, across all ion energy levels. This is strikingly different from the etching of monolayer graphene on SiO_2, where distinct transition from isotropic to anisotropic etching was reported at ~ 5-7 eV. This suggests that the differing van der Waals interaction between the targeted graphene nanoribbon and the underlying substrate (e.g. SiO_2 or a second graphene layer), and potentially the ion-substrate interaction, could significantly influence the edge-etching rates. The edge-etching mechanisms for the armchair and zigzag edges, however, are similar to monolayer graphene. As shown in Fig 4.11d and 4.11e, etching occurs by breaking of the interior C-C bonds close to the exposed armchair or zigzag edges to cause local unzipping of graphene chains (red arrows), followed by hydrogenation of the dangling C bonds (blue arrows) which break off to release CH_3 molecules. Our results for multilayer graphene imply that the competing effects of (a) lower energy of the inner C-C atoms on the armchair edges compared to the zigzag edges, versus (b) higher reactivity of the zigzag

edge atoms compared to the armchair edge atoms, balances out to achieve almost equal zigzag and armchair etching rates.[55,56]

4.7 Atomic-to-Continuum Scale Bridging for Multilayer Graphene

Our MD simulations capture the atomic-scale etching process associated with the energetic H ions, but cannot account the effects of H radicals and temperature-dependent dehydrogenation which occur at much longer time-scales. The H radicals have a density 10-100 times that of the energetic H ions.[30] Unlike the energetic ions, however, these radicals with thermal energy of ~ 0.026 eV at 300 ℃ cannot overcome the barrier energy of 0.5 eV to hydrogenate the C atoms in the graphene basal plane, nor can they react with CH_2 edge groups to form CH_3. Nevertheless, given the high density of H radicals, it is likely that these thermal radicals will readily hydrogenate the edge C atoms or dangling bonds of graphene to form CH and CH_2 groups. Thus, these H radicals will accelerate the edge-etching rates $\dot{D}_{\mathrm{e}}$ obtained from MD by a factor α, which ranges from 1 to 3. Note that $\alpha \cong 3$ for complete saturation of the zigzag or armchair edges to form CH_2 groups, while $\alpha = 1$ implies the absence of thermal radical effects. In addition, hydrogenation of the graphene basal plane has been shown to be reversible in samples subjected to hydrogen plasma for short time duration, prior to the formation of irreversible CH_2 and CH_3 groups. [62,66–68] Raman spectroscopy shows that a hydrogenated bi-layer graphene sheet experiences an 80 % drop in the density of C-H groups as the temperature increases from 50 ℃, where limited dehydrogenation occurs ($I_D/I_G = 2.6$), to the optimal plasma-etching temperature of 300 ℃ ($I_{\mathrm{D}}/I_{\mathrm{G}} = 0.5$). Although our MD simulations are also performed at 300 ℃, no C-H bond dissociation associated with thermal dehydrogenation is observed, akin to experimental measurements at 50 ℃, since this process lies beyond the time-scales accessible by MD. Consequently, with the absence of thermal dehydrogenation our MD simulations over-predict the basal plane etching rates by a factor of approximately 5.

Consider the radial expansion of a hole of radius R_j to $R_j + dR_j$ in the basal plane of an n-layer graphene sheet due to hydrogen plasma etching, where $j = 1\ to\ n$ denote the index of the

individual graphene layers L_j from top to bottom. The total number of C atoms removed from combined basal plane and edge etching can be expressed as

$$\left(\rho 2\pi R_j\right)dR_j = \left(\beta \dot{D}_{b,i}\, \xi\, 2\pi R_j\right)dR_j + \left(\alpha_j \dot{D}_{e,i}\, 2\pi R_j\right)d\xi \tag{4.3}$$

where $\dot{D}_{b,i}$ and $\dot{D}_{e,i}$ are the basal-plane and edge etching rates from MD, and the index i denotes the evolving count of graphene layers located directly above the (x,y) coordinates of layer L_j. We introduce the pre-factor $\beta = 0.2$ in Eqn 4.3 to account for dehydrogenation effects at 300 ℃, and include the layer-dependent pre-factor α_j to account for H radicals effects.

As an example, we simulate the hole growth process in a bi-layer graphene sheet on SiO_2 at ion energy of 2 eV. We divide each graphene layer into axisymmetric radial elements and solve Eqn 4.3 numerically using finite difference. The number of C atoms within the radial elements decreases with fluence during the etching process, and we delete the element once this number reaches zero. At any instant when a radial element of layer L_1 is removed, the index i for $\left(\dot{D}_{b,i}, \dot{D}_{e,i}\right)$ of the corresponding radial element directly below changes from 2 to 1 as that element in layer L_2 is now directly exposed to the plasma.

Fig 4.12a shows the evolution of the hole radii in graphene layers L_1 and L_2 as a function of the ion fluence ξ. We assume both graphene layers to have initial columnar holes of 5 nm radius. We first set $\alpha_1 = 1$ for the top layer and $\alpha_2 = 3$ for the bottom, with the rationale that thermal transport of H radicals along the exposed SiO_2 substrate will more likely hydrogenate the exposed hole edges of the bottom graphene layer L_2 than the layer L_1 above. At ion energy of 2 eV, basal plane and edge etching will be confined to the exposed layer, i.e. $\dot{D}_{b,2} \approx \dot{D}_{e,2} \approx 0$. Hole recession first occurs in layer L_1, which exposes elements bounding the hole in layer L_2. The index i of these newly exposed elements now changes from 2 to 1, thus initiating basal-plane and edge etching of these elements in L_2. Since the edge-etching rate of layer L_2 is 3 times faster than layer L_1 due to hydrogen radical effects ($\alpha_2/\alpha_1 = 3$), the expanding hole in layer L_2 rapidly catches up with the hole in layer L_1 and stops expanding. Hence, the hole growth rate in graphene layer L_2 will be limited by that of the top layer L_1, which results in columnar-type hole patterns (Fig 4.12b, top). After a fluence of 1.0×10^{18} ion/cm^2, the cumulative damage from basal plane etching on L_1 now dominates over damage introduced by edge-etching, and leads to rapid unstable hole growth in L_1. The hole growth rate also increases in L_2 due to combined

basal plane and edge etching, though the hole in L_2 continues to grow stably. This process leads to stepped-edge hole structures (Fig 4.12b, bottom). Based on a typical experimental flux of $\sim 1.5 \times 10^{15}$ ions/(cm^{2}s), the critical treatment time for columnar to step-edge transition is $\sim$ 11 min. We remark that such stepped-edge patterns can develop much earlier if the H radical effects are similar for both layers ($\alpha_1 = \alpha_2 = 3$ in Fig 4.12a). Both these columnar and stepped-edge hole patterns have been reported in hydrogen plasma-etching of multilayer graphene (Fig 4.12c).

4.8 Summary

We study the atomic-scale etching mechanisms of multilayer graphene, and the subsequent formation of nanopores, when exposed to downstream hydrogen plasma. Our molecular dynamics simulations based on reactive force-field potential reveal precise energy regimes for the transport of ions through, and selective etching of, individual graphene layers within the multilayer structure. Etching initiates with hydrogenation of the graphene basal plane, followed by localized C-C bond breaking which leads to the formation of CH_2, and subsequently, unstable CH_3 bond configurations. We establish the basal plane and edge etching rates of the individual graphene layers as a function of ion energy, and introduce a micromechanics model to predict the 3D-patterned pore structure at experimental length- and time-scales. Our results demonstrate the development of columnar holes in multilayered graphene, which transition to stepped-edge holes at higher fluence due to cumulative effects of basal-plane etching. The contributions of thermal radicals and dehydrogenation effects on the hole growth process are discussed.

4.9 Figures

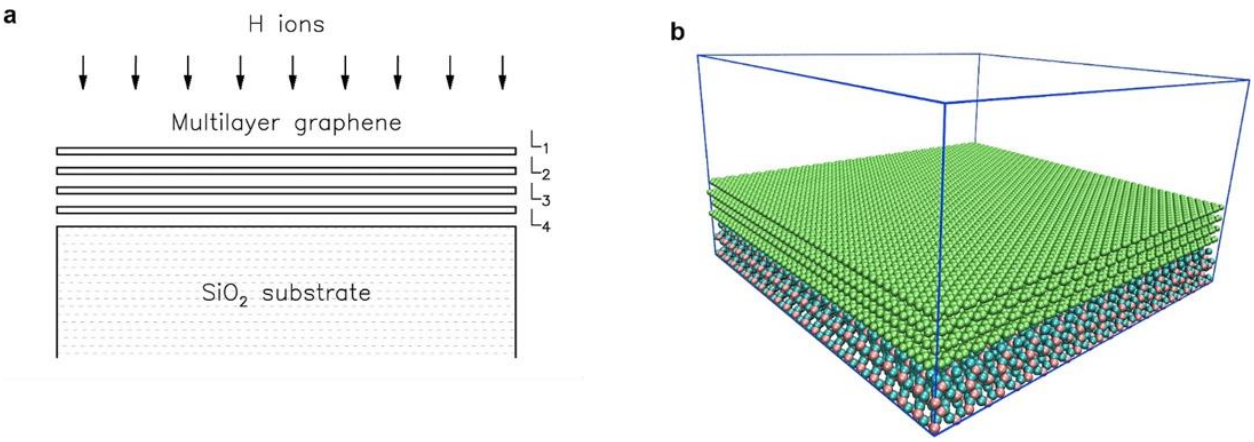

Fig 4.1: (a) Schematic of the energetic bombardment of H ions on quad-layer graphene supported on SiO_2 substrate; individual graphene layers labeled L_1 to L_4 sequentially from the top. (b) Initial atomic configuration of a quad-layer graphene sheet on SiO_2. The C, Si, and O atoms are colored in green, pink, and cyan, respectively. The MD simulation box, outlined in blue, is periodic in the in-plane directions.

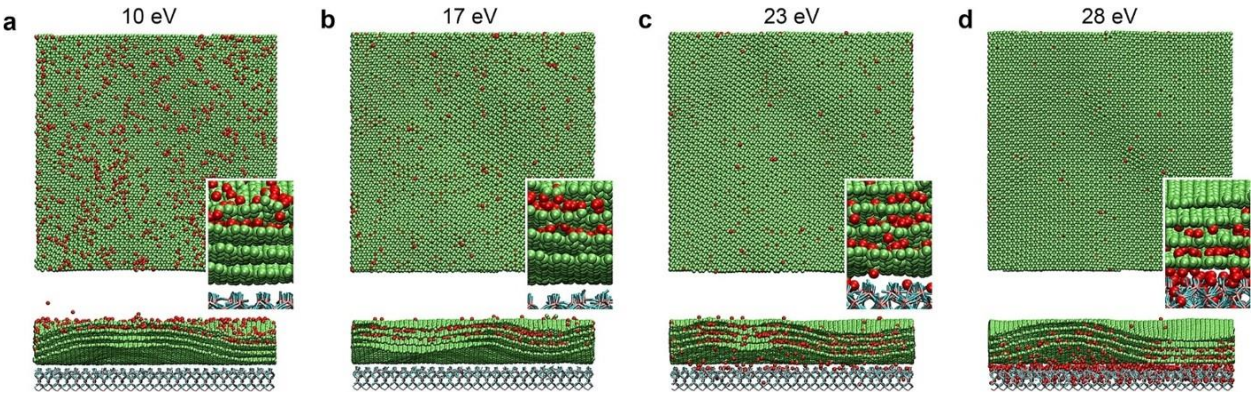

Fig 4.2: Top and side view atomic configurations of basal plane etching of quad-layer graphene on SiO_2, subjected to ion energies of (a) 10 eV, (b) 17 eV, (c) 23 eV, and (d) 28 eV. The snapshots are taken at a fluence of 1.5×10^{15} ions/cm^2. The H and C atoms are colored in red and green, respectively, while the SiO_2 substrate is represented by interconnected pink and cyan bonds. Close-up views show the extent of hydrogenation of graphene layers L_1 to L_4

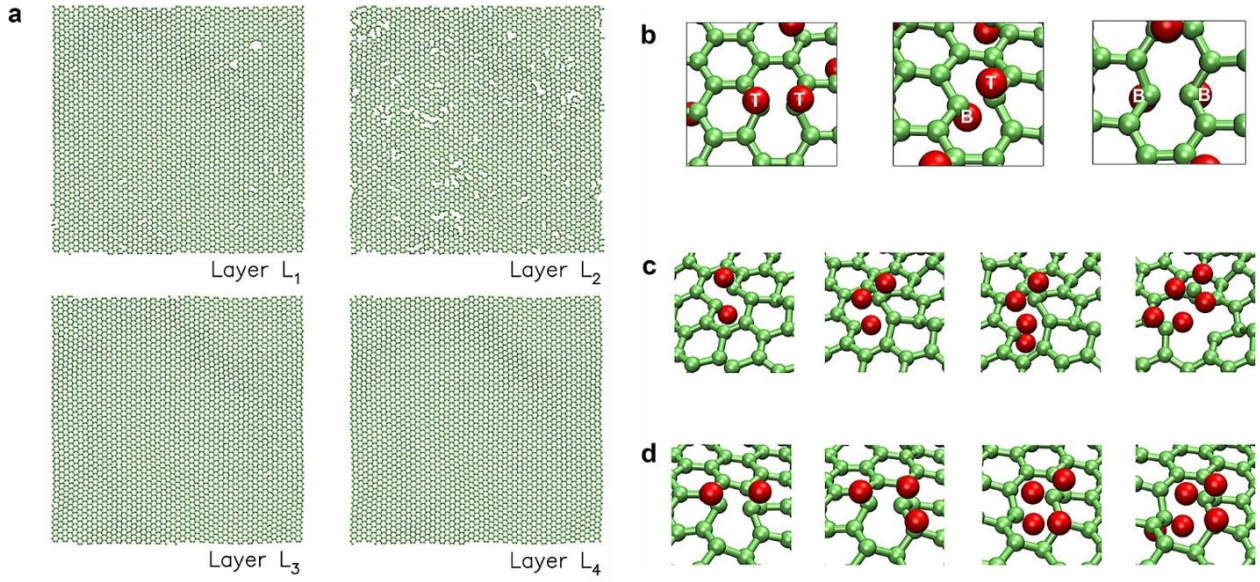

Fig 4.3: Mechanisms of basal plane etching of quad-layer graphene at ion energy of 17 eV. (a) Snapshots of atomic configurations of graphene layers L_1 to L_4 at a fluence of 3.0×10^{15} ions/cm^2, filtered to display only the C atoms and the C-C bonds. (b) Initiation of basal plane etching by the formation of C-H bond pairs on closest-neighbor C atoms in top-top (TT), top-bottom (TB), and bottom-bottom (BB) bond configurations. (c, d) Atomistic process of basal plane etching initiating from C-H bond pairs in a TB (c) or TT (d) bond configuration.

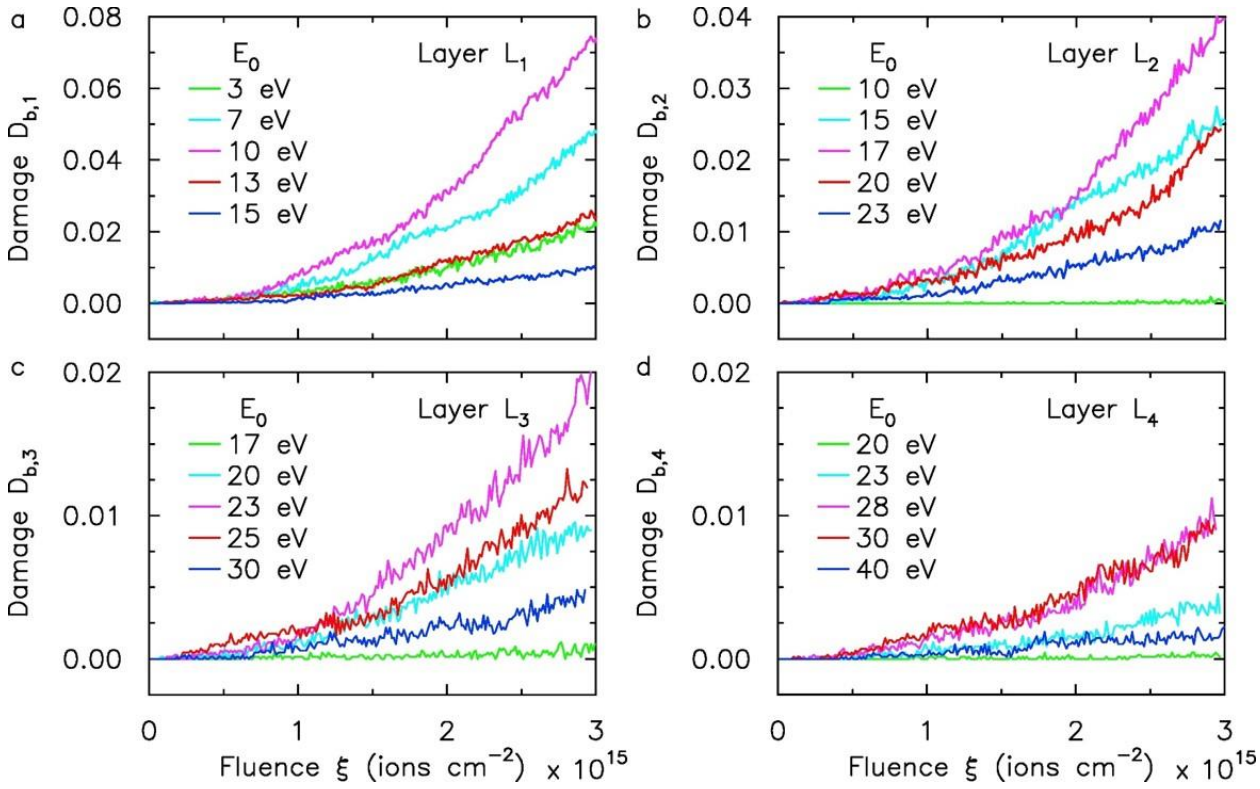

Fig 4.4: Evolution of basal plane damage D_b versus ion fluence ξ for the individual graphene layers L_1 to L_4 within the quad-layer graphene sheet, subjected to ion energies of 3 to 40 eV.

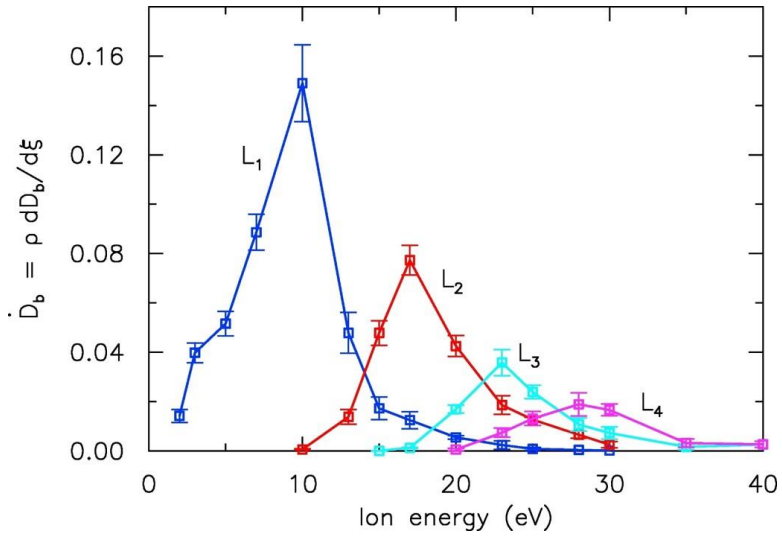

Fig 4.5: Summary of the steady-state basal plane etching rate per unit area, $\dot{D}_b$, versus the ion energy for the individual graphene layers L_1 to L_4 within the quad-layer graphene sheet. Error bars denote the standard error.

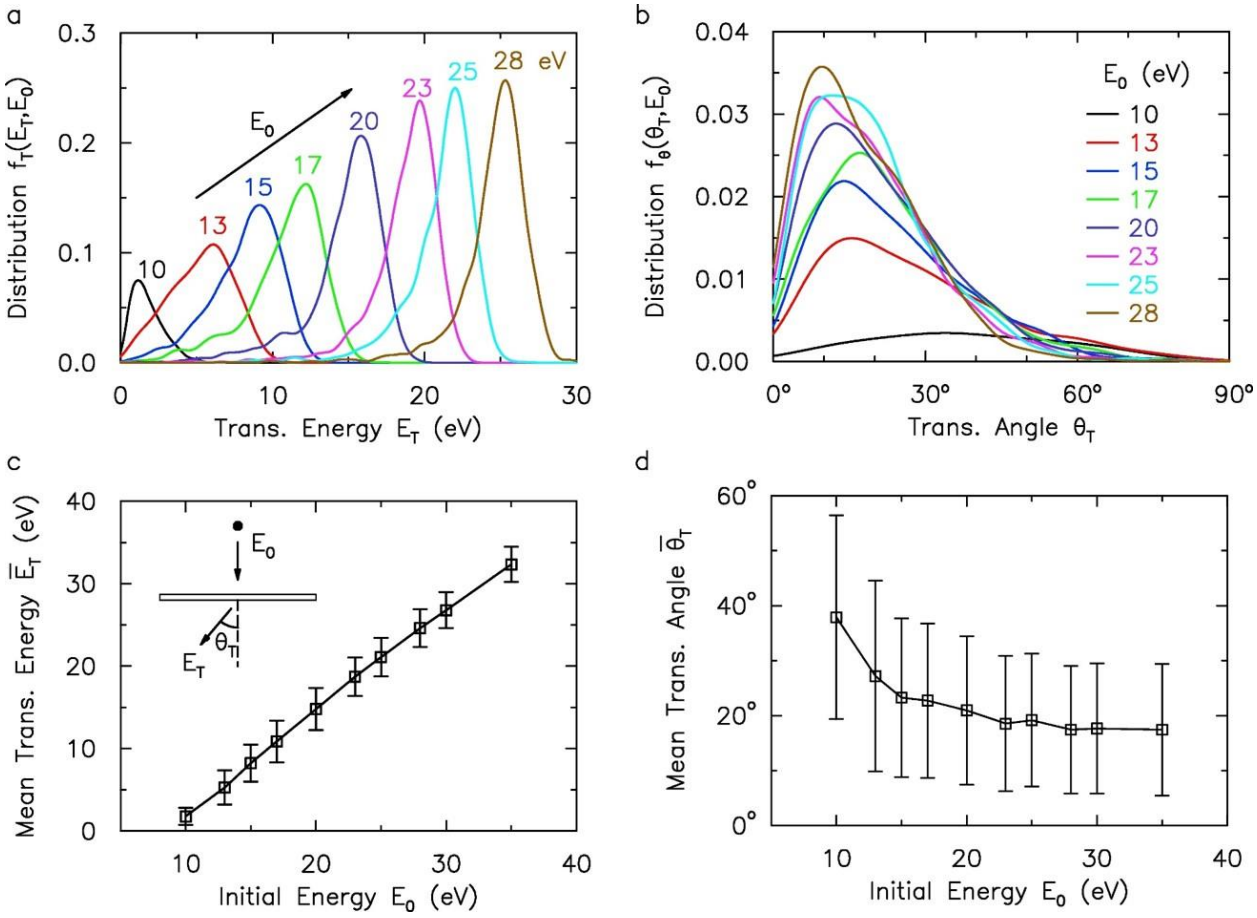

Fig 4.6: (a, b) Distributions of the (a) transmitted ion energies, and (b) off-normal polar angles, normalized by the ion density, for ions incident normally to a graphene layer with initial energy E_0. (c, d) Mean transmitted ion energy (c), and polar angle (d) as a function of E_0. Error bars in (c, d) denote the standard deviation σ of the sample.

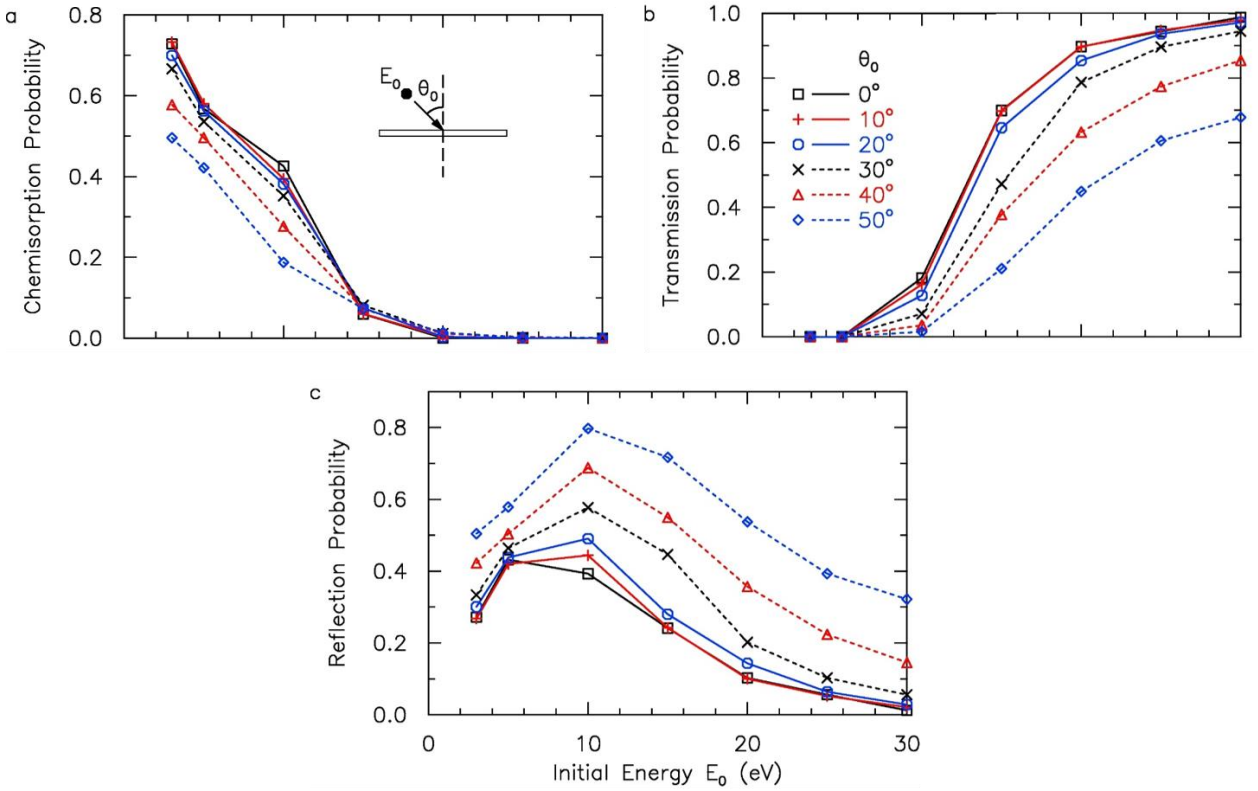

Fig 4.7: Probability of (a) chemisorption, (b) transmission, and (c) reflection of H ions incident on a graphene layer with initial energy E_0, and off-normal polar angle θ_0.

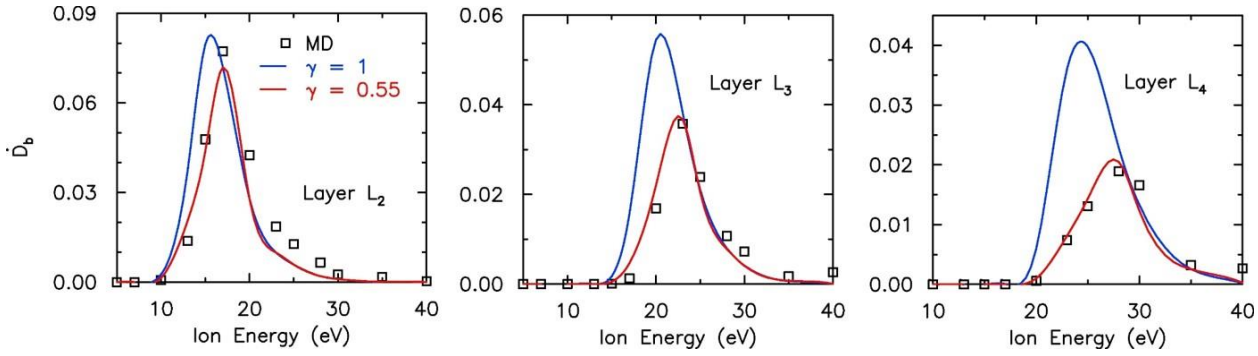

Fig 4.8: Basal plane etching rates in graphene layers L_2 to L_4 projected from the MD etching rate $\dot{D}_{b,1}$ in layer L_1, with (red curve) and without (blue curve) off-normal angular correction (γ). Open symbols denote the results from MD.

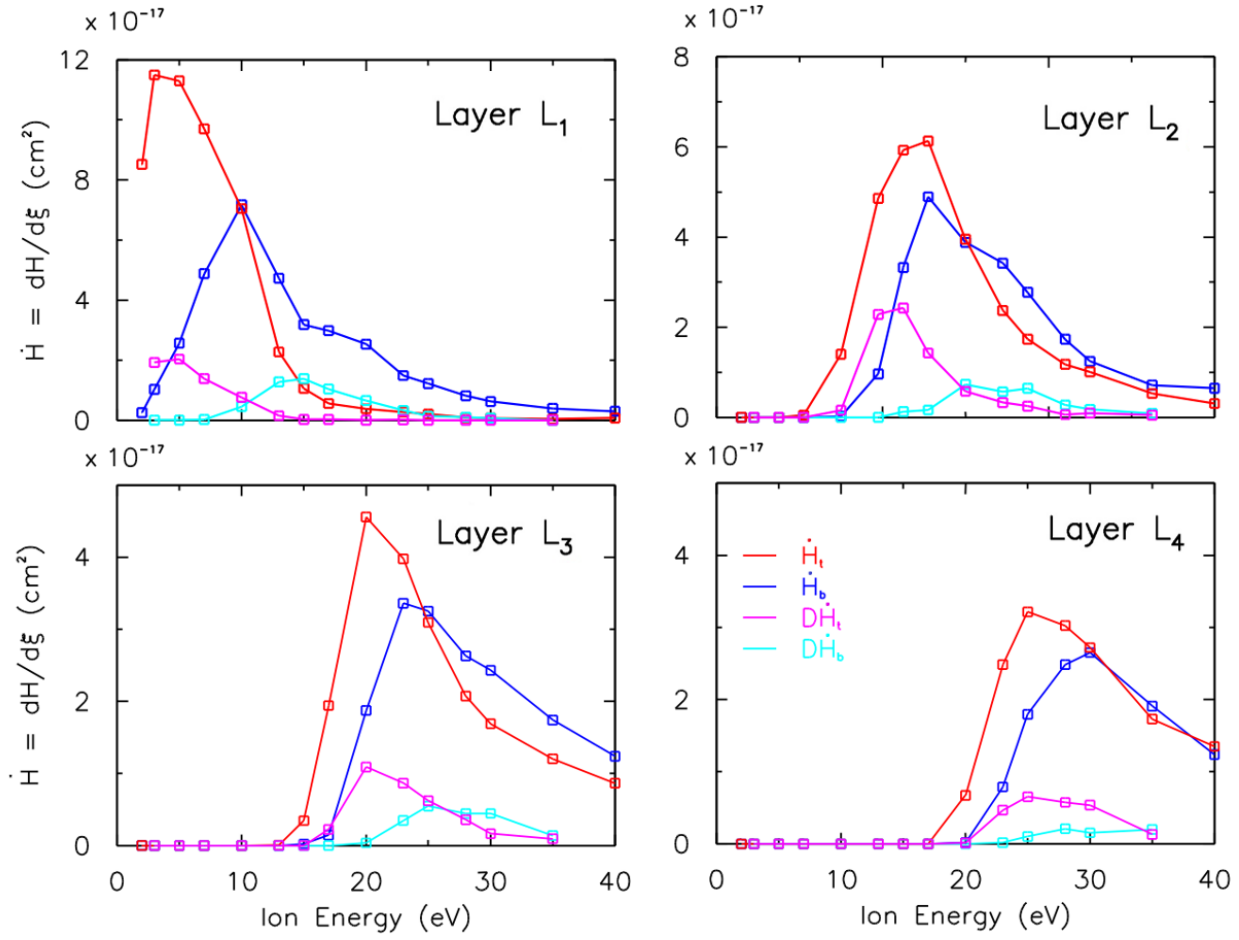

Fig 4.9: Red and blue curves denote the hydrogenation index of the top and bottom sides of the 4 layers in the quad layer graphene sheet respectively. The magenta and cyan curves represent the net dehydrogenation on the top and bottom sides of the graphene layers respectively. The dehydrogenation is determined by counting the number of formerly chemisorbed H atoms which are removed from the graphene layers.

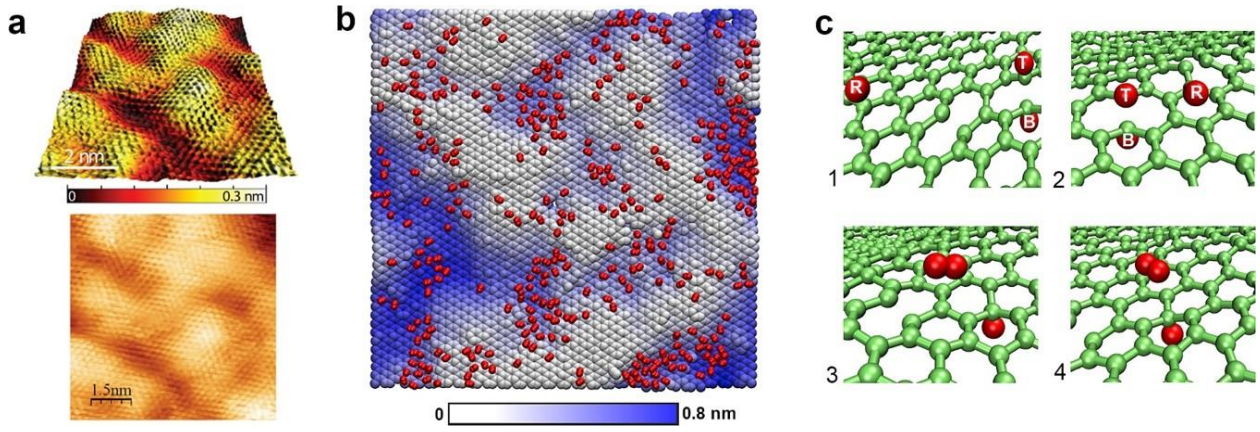

Fig 4.10: Subsurface clustering of H_2 molecules. (a) STM imaging of corrugated patterns of ripples and valleys with low density of surface defects on HOPG after hydrogen plasma exposure.[60] (b) Underside of layer L_1 of the quad-layer graphene sheet subjected to ion energy of 15 eV at a fluence of $3.0 \times 10^{15}\ ions/cm^2$. C atoms are colored by the relative out-of-plane displacements. H_2 molecules in the interlayer region are shown in red. (c) Formation of a H_2 molecule in the interlayer region between layers L_1 and L_2 caused by the combination of an intercalated H radical (R) and a top chemisorbed H atom (T) on layer L_2.

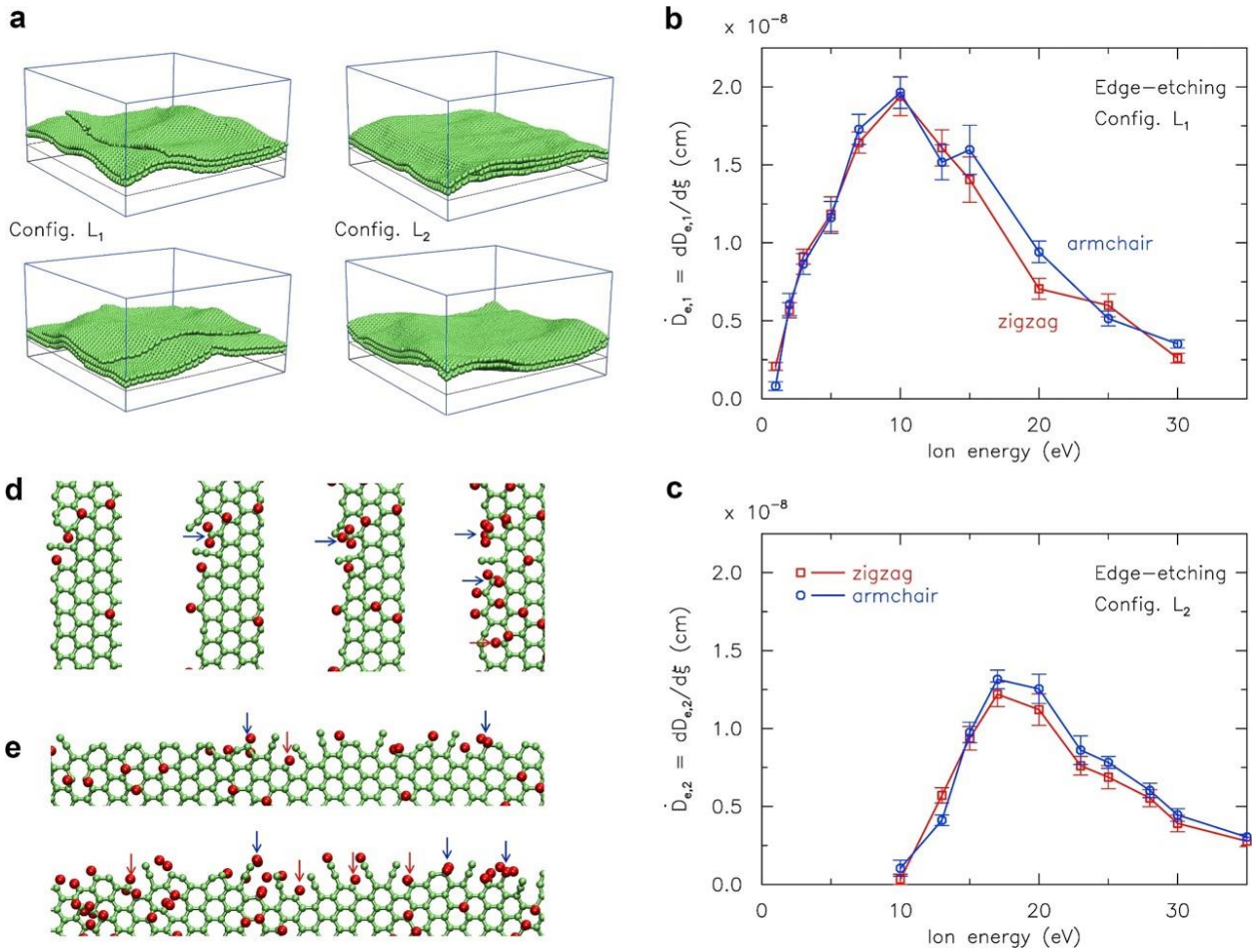

Fig 4.11: Edge-etching of multilayer graphene. (a) Atomic configurations for graphene nanoribbon with exposed zigzag (upper) or armchair (lower) edges, supported by (left) or sandwiched between (right) two fully-periodic graphene layers. (b, c) Summary of the zigzag and armchair edge-etching rates per unit edge length, $\dot{D}_e$, versus the ion energy for exposed (b) and sandwiched (c) graphene nanoribbons. Error bars denote the standard error. (d, e) Mechanisms of zigzag (d) and armchair (e) edge-etching by direct hydrogenation of edge C atoms (blue arrows) or breaking of inner C-C bonds attached to edge C atoms (red arrows).

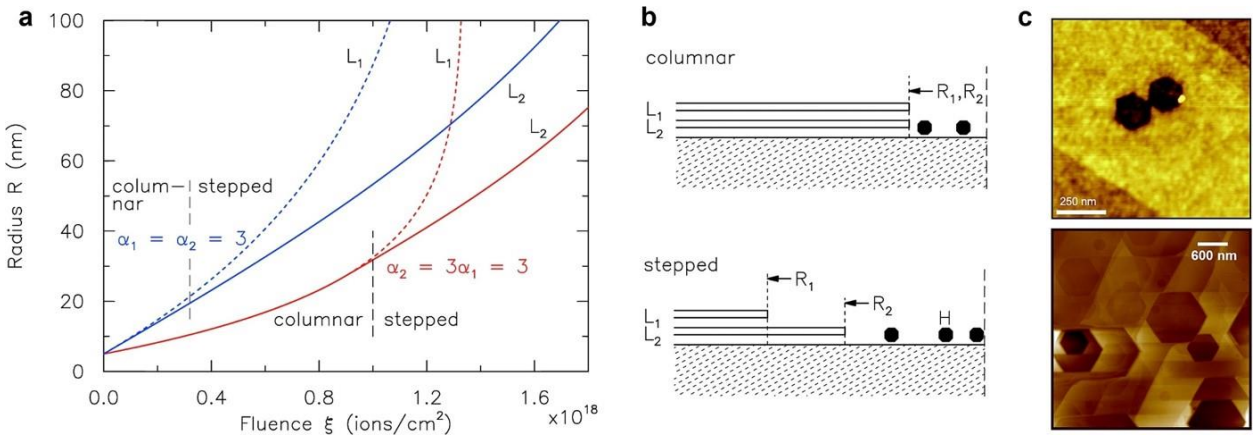

Fig 4.12: Kinetics of hole growth in the basal plane of multilayer graphene. (a) Hole growth radius *R* versus the ion fluence *ξ* for a two-layer graphene sheet. (b) Schematic of the transition from columnar to stepped-edge hole pattern. (c) AFM topography imaging of columnar hole patterns in few-layer graphene (upper), and stepped-edge holes in HOPG, after hydrogen plasma exposure.[28]

Chapter 5. Thermal Effects and Dehydrogenation

In our simulations so far, we have examined the effects of H ion energy on the different mechanisms of graphene etching and explained the experimental observations. However, MD simulations are limited in the duration of time that can be modeled due to femtosecond order time step necessary to resolve atomic vibrations. Consequently, the total duration of time simulated so far is in the order of nanoseconds compared to the experimental time scale of minutes. This ~ 9 order difference in time scales fundamentally limits MD simulations, as they cannot be used to capture slow processes. Thermal diffusion is one of the most common processes which are typically beyond the timescale of MD simulations. The diffusion occurs when a system oscillates within a local minimum in the phase space for long durations of time, with infrequent and instantaneous jumps between states. For the case of hydrogenated graphene, breaking of C-H bonds represents an infrequent event. Experiments have shown that graphene treated with hydrogen plasma for a short duration of time undergoes dehydrogenation which is detected by the reduction in the D band peak in the Raman signature. The graphene can in fact be restored to its initial pristine state under certain plasma conditions, typically when treated for a short duration. In addition to thermal dehydrogenation, combination of thermal radicals in the plasma and chemisorbed H atoms on the graphene surface via the Eley-Rideal process also contributed to surface dehydrogenation.[64]

Luo *et al.* performed short duration plasma treatment of monolayer and multilayer graphene to study the role of temperature, treatment time, and number of layer on the dehydrogenation kinetics.[62] Graphene samples were prepared by mechanical cleaving from HOPG and were place on an SiO_2 substrate. These samples which contained regions of graphene ranging in number of layer from one (monolayer) to five were hydrogenated for 1 min. The H_2 gas ionized by a plasma source operating at 10 W with a gas pressure of 1 Torr. The ratio of the D band to the G band in the Raman signature was used to determine the number of H bonds on the graphene. Following the plasma treatment, the samples was heated at a rate of 50 ℃/min to a desired annealing temperature. Fig 5.1a shows the D band to G band ratio for monolayer graphene as a function of time. From the near exponential decay profile during annealing at the end of the plasma treatment, we can conclude that 1st order kinetics govern the dehydrogenation process. The authors examine the role of annealing temperature and plasma power (5 W and 15

W) on the dehydrogenation characteristics. From Fig 5.1b they can observe that dehydrogenation is faster at higher H concentration (mechanism I) suggesting the H-H surface interactions (Langmuir – Hinshelwood mechanism)[69] play a significant role. Further the dehydrogenation rates are lower for sheets which are exposed to the plasma for a longer duration, indicating that H atoms involved in CH_2 and CH_3 bonds are less likely to dissociate as compared to the early state CH bonds.

Several experimental groups studying the etching of graphene by hydrogen plasma report that the etching rate peaks at ~ 300-400 ℃ and decreases with further increase in temperature, usually being completely suppressed beyond ~ 700 ℃.[27–29] Interestingly, this phenomena has also been observed for hydrogen plasma etching of graphene supported on copper,[70] as well as for other 2D materials such hexagonal boron nitride (hBN)[71]. The non-monotonic etching rate profile can be explained by an interplay between two competing effects: Increase in C-C bond breaking rate with temperature versus decrease in hydrogen coverage with temperature due to dehydrogenation. In other words, if we imagine that H atoms to be somehow 'locked' on the graphene sheet once deposited, the etching rate should display an increasing profile with temperature. In reality, however, the H atoms are free to dissociate from the C atoms and do so with increasing rate at higher temperature. For temperature beyond 700 ℃, the dehydrogenation rate might be so high that deposited H atoms dissociate and are removed from the graphene before they can play a role in the C-C bond breaking. Thus, in order to understand the temperature effects, we must quantify the C-H dissociation kinetics.

In this chapter we use high temperature MD simulations to accelerate the infrequency C-H bond dissociation and obtain the activation energy and exponential pre-factor of the associated process using the Arrhenius law. Our simulations are performed on a pre-treated, free standing hydrogenated graphene sheet with interactions between C and H atoms governed by the ReaxFF potential. Next we compare the activation energy of graphene dehydrogenation obtained from high temperature MD simulations to Nudged Elastic Band (NEB) calculation.[72] NEB is also used to calculate the barrier energy for H surface diffusion and H-H recombination via the Langmuir – Hinshelwood mechanism. Based on the activation energy obtained from NEB and MD we comment on the viability of time-scale extension using accelerated MD methods in chapter 6.

5.1 Kinetics of Dehydrogenation in Monolayer Graphene

5.1.1 Simulations Setup

We model a hydrogenated graphene sheet in a 10 × 10 × 8 nm^3 MD box which is periodic in the in-plane (*x*-*y*) dimensions and fixed in the *z* directions. The graphene sheet was hydrogenated by first selecting a certain percent of C atoms in a pristine lattice and placing an H atoms at a distance of 1.1 Å, on either the top of the bottom side with equal probability. The system is then subjected to energy minimization using the conjugate gradient method to allow the hydrogenated C atoms to undergo sp^2 to sp^3 transition. Note that the equal sided pre-hydrogenated sheet is modeled to represent graphene exposed to 10 eV H plasma, which also produces equal sided hydrogenation as shown in chapter 2. The graphene sheet is placed in the simulation box with a 4 nm thick vacuum layer in the *z* direction on either side. The C atoms in the system are heated to a temperature ranging from 2100-2700 ℃ using a Berendsen thermostat for 225 ps. For each temperature we considered graphene sheets with different extents of pre-hydrogenation, where 4-14 % of C atoms are hydrogenated. Each case is repeated ten times with different set of initially saturated C atoms (by changing the random seed). We calculate the number of C-H bonds in the system during the simulations (cutoff = 1.45 Å). Due to thermal dehydrogenation this number is expected to decrease with time from the initial value. H atoms which are desorbed and leave the simulations box are ignored. Note that the elevated temperature of 2100-2700 ℃ is chosen to accelerate the dehydrogenation process to capture sufficient statistics within the relatively short 225 ps simulation. During the high temperature dehydrogenation simulations, the graphene sheet remains intact with the exception of a few C-C bonds broken due to the initialization of H atoms on neighboring C atoms. To ensure we do not gather erroneous hydrogenation data of a highly damaged sheet, an error message is triggered if more than 5 % of the C-C bonds are broken, and the simulation results are discarded.

5.1.2 Activation Energy and Pre-exponential Constant

Over the course of the MD simulations we observe that the number of C-H bonds decrease with time in an exponentially decreasing fashion as governed by 1st order kinetics. Fig 5.2 shows the graphene sheet before and after the heating in MD. The number of C-H bonds denoted by $N^{CH}(t)$ is expected to decrease as,

$$log[N^{CH}(t)] = log[N_o^{CH}] - kt \tag{5.1}$$

where, N_o^{CH} is the initial C-H bond count and k is the reaction rate constant. For each temperature (2100 to 2700 ℃) and each initial H concentration (4 % to 14 %) we repeat the simulations for ten independent cases. By fitting the least square error linear regression on the MD derived $N^{CH}(t)$ and taking the slope we obtain the value of k. We determine the reaction rate for a given temperature by taking the average over the simulations performed as different initial H concentrations (over the ten runs for each initial H concentration). Fig 5.3a shows the plot of $log[N^{CH}(t)]$ versus time (t) for the various initial H concentrations subjected to temperature of 2100 ℃. The system is expected to follow the Arrhenius law. Hence, we can write,

$$log(k) = log(B) - \frac{E_a}{RT} \tag{5.2}$$

From the plot of $log(k)$ versus $1/T$ shown in Fig 5.3b, we obtain the activation energy $E_a = 1.523$ eV and pre-exponential constant $B = 4.527 \times 10^{12}\ 1/\mathrm{s}$. Our findings are in agreement with previous DFT and experimental calculations which report the dehydrogenation barrier energy to be between 1.1-1.32 eV.[68,73–76]

5.1.3 Surface H-H Recombination and Thermal Dehydrogenation Mechanism

During high temperature MD simulations we observe three mechanisms governing the transition of the H atoms on the graphene sheet: thermal desorption, surface hopping and Langmuir – Hinshelwood recombination, as shown in Fig 5.4a. The first two mechanisms (hop and desorb) are governed by 1st order kinetics which the Langmuir – Hinshelwood (LH) recombination mechanism is governed by 2nd order kinetics since it involves two H atoms. Fig

5.4b shows the removal of two H atoms and the formation of H_2 molecule during the MD simulations on the graphene surface. Previous experiments by Hornekar *et al.* have reported H_2 dimer formation as via LH mechanism on graphene surfaces.[73] Fig 5.4c shows the SEM image of dimer formation during thermal annealing of graphene after 1 min of plasma treatment.

Since we assumed purely 1st order kinetics in the previous section, we determine the role of LH mechanism by calculating the number of H atoms which are removed by recombination with a neighboring H atoms. Fig 5.5a show the percent of LH contribution as a function of initial H concentration. These results are expected since H atoms are more likely to be in closer proximity with increasing H concentration, thus increasing the frequency of recombination. We examine the effect of the LH mechanism on the chemical kinetics of dehydrogenation by calculating the activation energy E_a as a function of initial H concentration (Fig 5.5b). Observe that E_a increases monotonically with H concentration from 1.393 eV to 1.681 eV suggesting that the LH mechanism represents a higher barrier process than thermal desorption. Since during hydrogen plasma treatment the H surface coverage is expected remain low, we must consider the chemical kinetics obtained from MD simulations with low initial concentration (4%) of H atoms. Thus the true activation energy for the dehydrogenation process is $E_a = 1.393$ eV and the corresponding pre-exponential constant is $B = 3.465 \times 10^{12}\ 1/\text{s}$.

5.2 Nudged Elastic Band (NEB) Analysis

Nudged Elastic Band (NEB) is a method for calculating the barrier energy and the minimum energy path (MEP) between two neighboring transition states in a system.[77] The MEP is defined as the path along which forces on the system act only along the direction of the path. The maxima along the MEP are saddle points in the potential energy surface of the system. Barrier energy is defined as the difference between the energy of the initial state and largest maxima point along the MEP. NEB involves first identifying the initial and final states of interest and constructing an initial MEP by evenly dividing the straight line join them. A spring interaction is added between consecutive images in the MEP to mimic an elastic band. The optimization involved modifying or 'nudging' the coordinates of the images to minimize the sum of the total energy, defined as the sum of the energy of the states and the elastic energy stored in

the springs. Here, we use a variant of the NEB called the Climbing Image Nudged Elastic Band method (CI-NEB)[72] which divides the methods into two steps: 1) the MEP is calculated using regular NEB, 2) The current image with the highest energy on the MEP is then displaced to move to the top of the saddle point using the barrier climbing methods described by Henkelman.[72]

We use the CI-NEB to calculate the static barrier of H desorption, H hopping and H-H recombination (LH mechanism) on monolayer graphene. A total of 56 replicas are used between the initial and final states for all three simulations. The spring between consecutive images are assigned a spring constant (for parallel nudging force) of 69.47 $pN/Å$. Damped dynamics with a time step of 0.5 fs and energy tolerance of 10^{-10} kcal/mol is used to minimize the total energy for each iteration. Damped dynamics is superior to the conjugate gradient method, since it reduces the likelihood of the MEP getting stuck in local maxima. The reaction coordinate is defined as the fractional distance along the optimized MEP. Fig 5.6 shows the potential energy along the reaction coordinated for the three dehydrogenation mechanisms considered. The barrier energies for hopping (Fig 5.6a), desorption (Fig 5.6b) and recombination (Fig 5.6c) are 2.64 eV, 2.69 eV and 2.18 eV respectively.

The static barrier energy of 2.69 eV obtained from NEB is significantly higher that the dehydrogenation barrier energy of 1.393 eV calculated from high temperature MD simulations. Although Fig 5.3b shows that the dehydrogenation kinetics obey the Arrhenius law very well for temperature between 2100 ℃ and 2700 ℃ the curve may not remain linear at lower temperatures. The NEB barrier represents the activation energy of the system as the temperature approaches 0 K. Hence the graphene dehydrogenation is a process which has temperature dependent chemical kinetics and does not truly follows the Arrhenius law over a wider range of temperatures of interest. The implications of this conclusion are discussed in more detail in chapter 6.

5.3 Summary

High temperature MD simulations were used to examine the kinetics and mechanism of the thermal dehydrogenation on monolayer graphene. The H atoms were shown to undergo desorption by thermal vibrations as well as surface recombination via the Langmuir – Hinshelwood (LH) mechanism. We obtained the activation energy $E_a = 1.393$ eV and pre-exponential constant $B = 3.465 \times 10^{12}\ 1/\mathrm{s}$, for low initial H coverage of 4 %. The extent of thermal dehydrogenation was shown to increase monotonically with increasing H coverage due the increasing contribution of the LH recombination mechanism. The role of the LH recombination mechanism was also confirmed by calculating the fraction of chemisorbed H atoms which recombine to form H_2 over the duration of the MD simulations. Nudged Elastic Band (NEB) analysis was performed to obtain the static barrier energy of thermal desorption, hopping and LH recombination mechanism. The NEB barrier of 2.69 eV deviated significantly from the MD calculated activation energy of 1.393 eV.

5.4 Figures

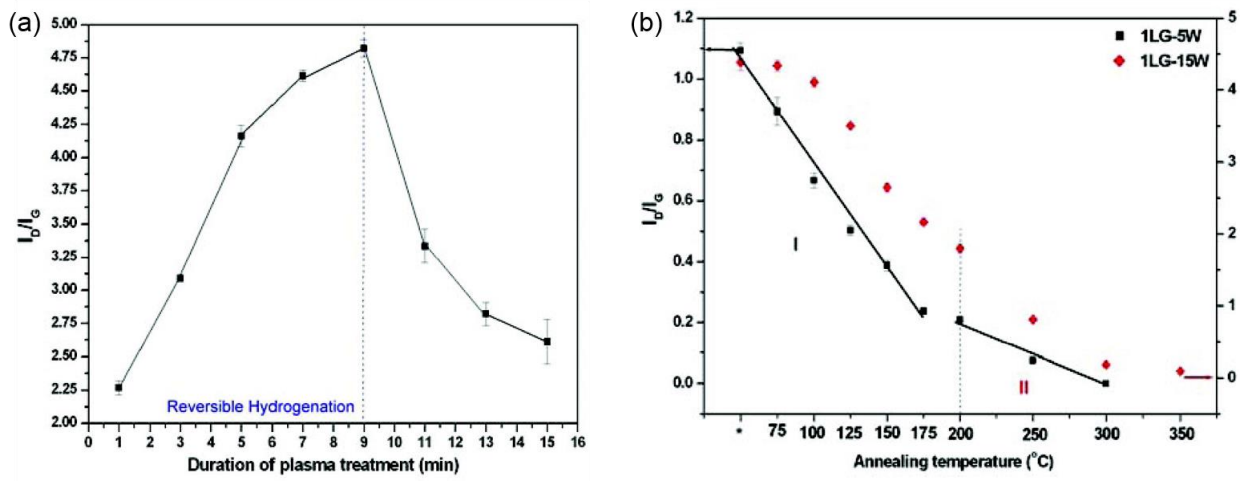

Fig 5.1: Experimental observations of thermal dehydrogenation in graphene.[62] a) The ratio of D and G band in the Raman spectrum of hydrogen plasma treated graphene showing reversible hydrogenation. b) Influence of ion energy on the reversibility of hydrogenation. The 15 W treatment which results in lower hydrogenation shows a lower drop in I_D/I_G ratio.

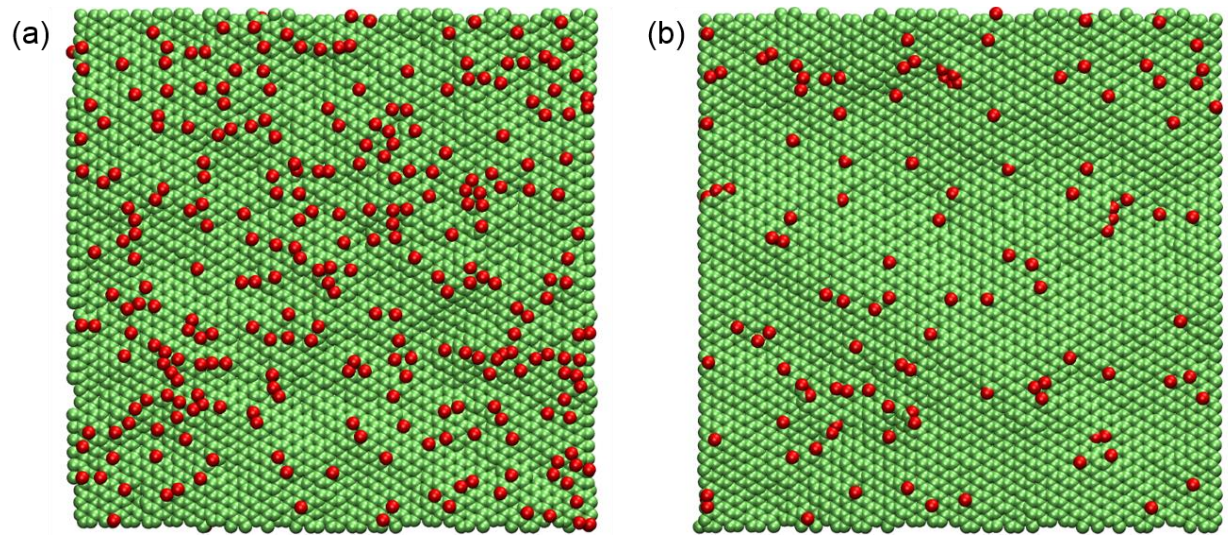

Fig 5.2: MD screenshot showing the chemisorbed H atoms on a monolayer graphene sheet before (a) and after (b) annealing at 2300 ℃ for 225 ps. The initial H coverage is 14 %. H atom are colored red while the C atoms are colored green.

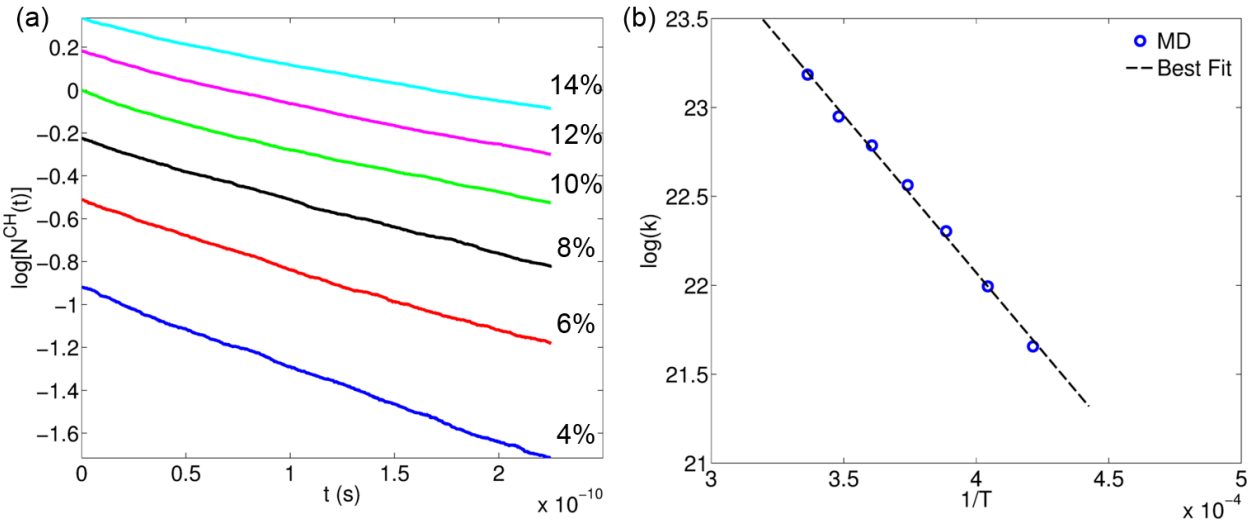

Fig 5.3: Kinetics of graphene dehydrogenation. a) The log of number of C-H bonds versus simulations time for various initial H concentration during high temperature MD simulations at 2100 ℃. The curves follows a linear profile as expected from a 1st order reaction. b) The plot of $log(k)$ versus $1/T$ along with the best fit linear regression. The activation energy and pre-exponential constant is obtained from the slope and y-intercept of the best fit line.

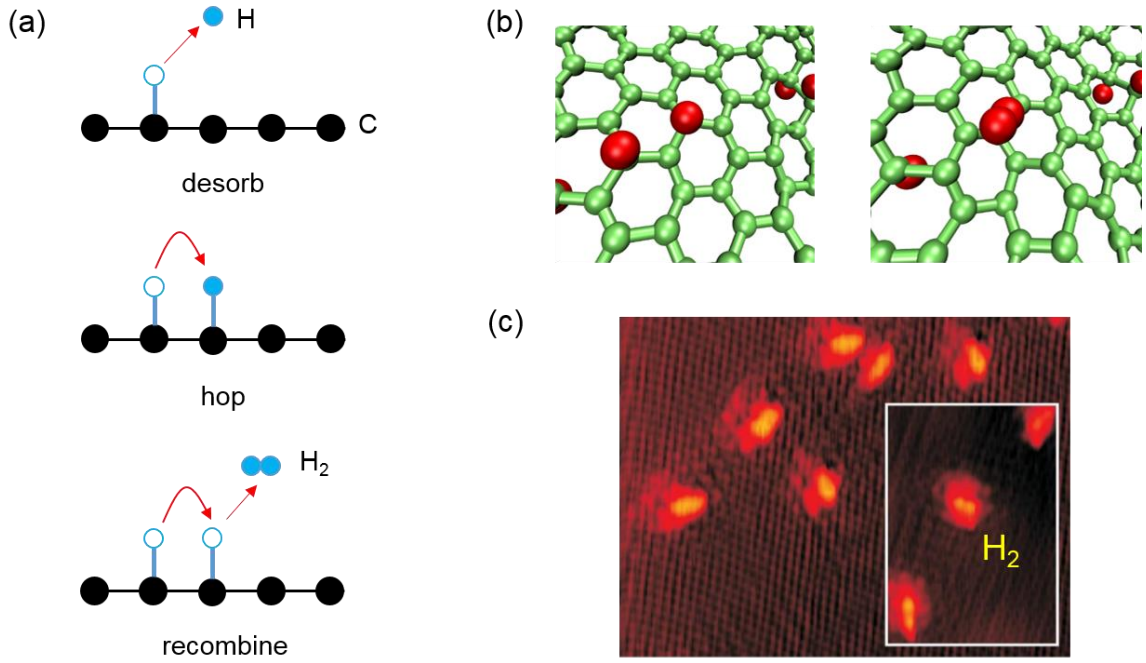

Fig 5.4: Mechanisms of graphene dehydrogenation. a) Schematic showing desorb, hop and recombine mechanism active during high temperature MD simulation. b) MD screenshot showing the LH recombination mechanism of surface H on graphene. c) SEM images of annealed graphene showing LH recombination and the subsequent formation of H_2 molecule.[74]

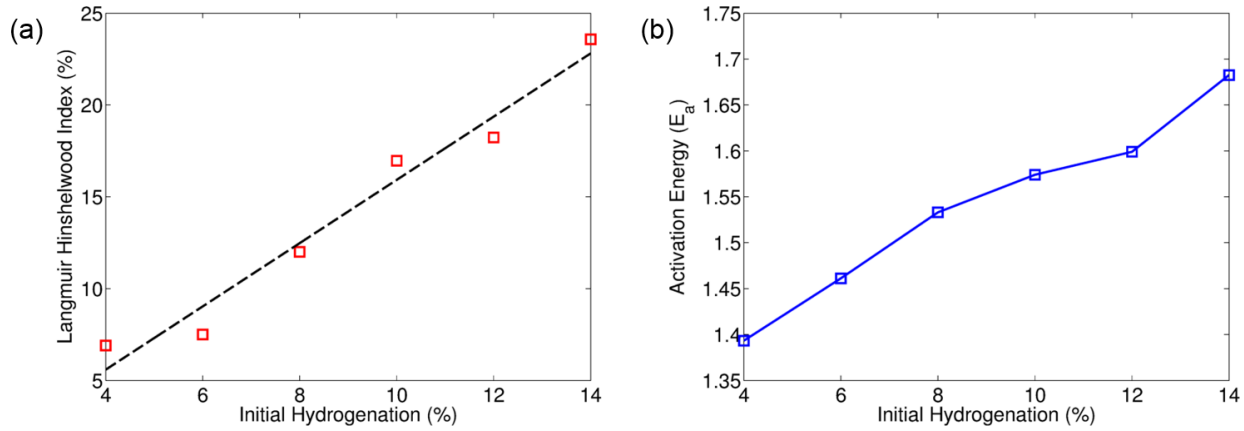

Fig 5.5: a) LH recombination index as a function of initial H concentration. The LH recombination index is defined as the percent of H atoms which are removed from the graphene due to surface recombination. b) Activation energy as a function of initial H concentration. The monotonous increase in a) and b) suggests that the LH mechanism has a higher barrier energy that the pure thermal desorption.

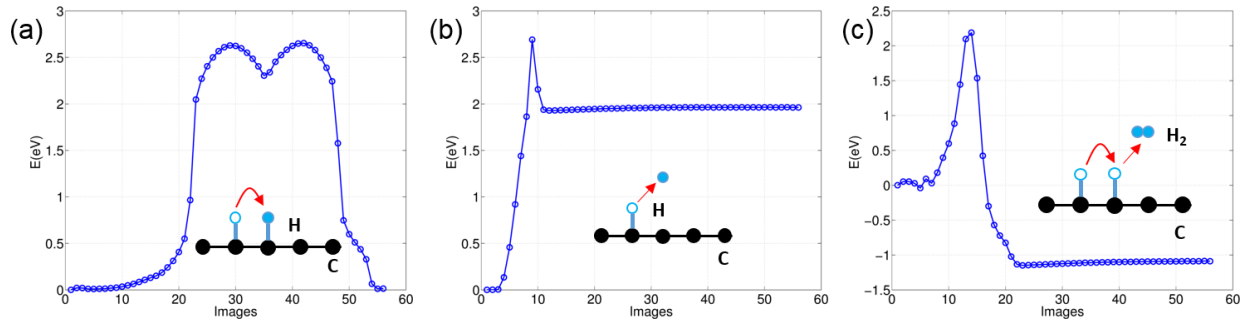

Fig 5.6: Energy of the images along the MEP path obtained by NEB analysis of three mechanism of dehydrogenation, namely hop (a), desorb (b) and recombine (c).

Chapter 6. Future Work and Limitations: Graphene Patterning

In this chapter we discuss some possible avenues of research in the field of hydrogen plasma patterning of graphene. The primary focus of the discussion is the '*time-scale*' limitations of MD simulations and its implications on the role of temperature effects. We also briefly discuss limitations of the classical assumption of MD simulations and possible quantum effects which may affect the accuracy of our MD predictions.

The long standing limitation of MD simulations is the requirement of a femtosecond scale time step to account for thermal vibrations of the atoms.[78] With the current computational capabilities, MD simulations are limited to time-scales of several nanoseconds, and length-scales of several hundred nanometers. While we have addressed the length-scale limitations through micromechanics modeling (section 3.7 and 4.7), the time-scale limitations have not been fully addressed. Phenomena like diffusion, surface annealing and vapor deposited film growth which play a crucial role in many processes of interest occurs over a time-scale of seconds or minutes.[79] These slow processes involve systems where atoms are trapped in local potential energy minima (transition states) for long durations of time with infrequent and instantaneous jumps between discrete transition states. The periods of inactivity in local potential energy basins does not provide any information about the long term evolution of the system but consumes the majority of the simulations time. In the hydrogen plasma graphene system, the C-H and C-C bonds breaking represent such discrete transitions. In the previous chapter we examined the kinetics of the C-H bonds dissociation by raising the temperature of the MD simulations to 2100-2700 ℃. The simplistic approach of high temperature MD is, however, only viable for single step reaction of H desorption. It is not possible for instance, to obtain the kinetics of C-C bond dissociation by high temperature MD simulations. The reason for this is that the process of C-C bond dissociate involve a complex reaction involving multiple steps of CH, CH_2 and CH_3 formation, followed by thermal dissociation of the CH_3. Voter *et al.* showed that simply raising the temperature of a multistep reaction in MD skews the relative ratios of the reaction rates and produces incorrect and unphysical dynamical evolution.[80]

Methods such are parallel replica dynamics (PRD),[81] bond boast method,[82] hyperdynamics[83] and temperature accelerated dynamics (TAD)[80] have been proposed to accurately accelerate MD simulations. A key underlying assumption of all these methods called

'*harmonic Transition State Theory*' (*hTST*).[84] It states that the potential energy landscape must be approximated by a collection of potential basins in which the system vibrated close to the minimum energy position.[84] The range of vibration must be small enough for each state to be approximated as vibrations in a harmonic well. In other words, the stretching of the bonds must be small enough that they can be approximated as linear springs which only discretely and infrequently break and reform. Perez *et al.* suggested that metallic systems follow the assumption of *hTST* up to approximately half of their melting temperature.[85] In general this assumption is a good approximation for the potential surface formed by ordered crystals or interstitial adatoms. It is however, not known if the thermal processes on hydrogenated graphene, which are of interest to us, can be approximated by *hTST*. A consequence of the *hTST* assumption is that the activation energy of a single step process is temperature independent. From the discrepancy between the dehydrogenation activation energy from high temperature MD (1.393 eV) and the static NEB calculation (2.69 eV) we can conclude that the C-H bonds dissociation does *not* follows *hTST*. The light mass of the H atoms and planar nature of the graphene sheet results in large vibration of the H atoms in the C-H basin which likely violate the assumption of bond linearity. Consequently, none of the time acceleration methods can be applied to the hydrogen plasma graphene system. Hence, a possible avenue for future research is the development of a time-acceleration scheme which does not rely on *hTST* and can be applied to amorphous materials. Such a method applied to the hydrogen plasma patterning of graphene will allows for a complete exploration of the flux, energy and temperature phase space and tremendously improve the predictive capacity of atomic scale simulations.

Finally, we discuss the assumption of classical treatment of atoms which is universal to all MD or accelerated MD simulations. It is often uncritically assumed that a collection of atoms are governed purely by classical equation of motion without regards to the dual wave-particle nature.[18,86,87] MD simulations cannot access the quantum states of a systems, but the role of quantum effects can be examined by calculating the De-Broglie wavelength λ of the constituent atoms using the following equation,[88]

$$\lambda = \frac{h}{\sqrt{2\pi m k_B T}} \tag{6.1}$$

For the classical assumption to be valid, λ must be smaller than the typical bond length (~ 1.5 Å), or lattice spacing, and ideally should be much smaller than the bond length.[88] Using Eqn 6.1 it can be shown that this is only valid for systems involving heavy atoms at high temperature (or velocities). Since the hydrogen graphene simulations involve the light H atom, it is very likely that some physics of phenomena is fundamentally beyond the scope of classical MD simulations. For instance, an H atom vibrating at a temperature of 300 ℃ has a De Broglie wavelength of $\lambda = 0.729$ Å, which is smaller than the C-C bonds distance of 1.42 Å but of similar order of magnitude. However, during the bombardment phase of the simulation, the kinetic energy range of ion bombardment (1-30 eV) corresponds to a De Broglie wavelength of 0.02-0.11 Å, implying that the assumptions of classical MD simulations holds well during the bombardment phase.

In Fig 6.1, we highlight the region of the temperature-atomic mass plane where λ is less than the 0.2 Å (sufficiently small to be considered much less than lattice spacing). Note that even for heavier atoms such as Si, the critical temperature below which classical assumption can be comfortably applied is reasonably high, ~ 272 K. Hence, further critical investigation into the role of non-classical phenomena in MD simulations should be performed to improve the fidelity of MD simulations.

6.1 Figures

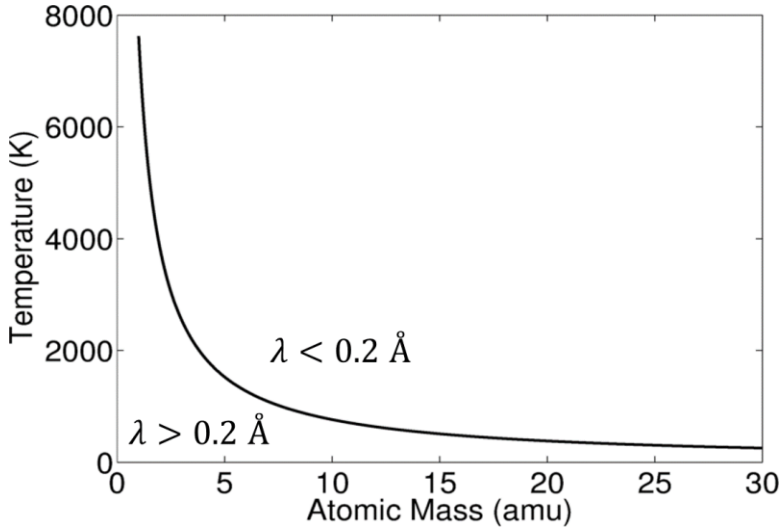

Fig 6.1: Regions in the temperature-atomic mass plane where the De Broglie wavelength transition 0.2 Å.

PART II: PYROLYSIS MODELING OF POLYMER BASED ABLATIVE THERMAL PROTECTION SYSTEM

Chapter 7. Background: Ablative TPS

In part II (chapter 7-11) of this dissertation we shift our focus from controlled plasma patterning of graphene to erosive effect of plasma on material surfaces. Here we consider the example of ablation of spacecraft thermal protection system (TPS) due to atmospheric plasma which is generated by shock heating of ambient gases during high speed re-entry. TPS is the barrier that shields a spacecraft from the high heating loads encountered during the atmospheric re-entry phase. TPS can be non-ablating or ablating. In the non-ablating TPS, a major portion of the impinging heat is reflected and re-radiated, but the TPS does not undergo appreciable changes in mass or properties. Comparatively, the ablating TPS can withstand much higher heat loads through the process of phase change and mass loss. More specifically, in an ablating TPS, the heat triggers the thermal decomposition of the material close to the surface which sublimates from solid to gas in an endothermic process which absorbs some of the thermal energy.[89] More importantly, the pyrolysis gas generated from the material decomposition provide transpiration cooling and pushes the heated shock layer away from the surface, effectively reducing the incident heat flux. Because of the sacrificial nature of the ablating TPS, a critical design parameter is the minimum required TPS thickness for a given heat load. Continuum-level thermal response models have been proposed using heat flux from the trajectory as boundary conditions, and the required TPS material thickness have been obtained by integrating the total heat load. More sophisticated mechanism-based models also include the contributions of solid-to-gas transitions of the phenolic resin, the thermal properties associated with the charring layer, as well as transpiration cooling effects from blowing gases.[90]

For our analysis we consider AVCOAT, which is an ablating TPS materials manufactured for use in NASA's next generation of manned space exploration vehicle – Orion.[91] Part II (chapter 7-11) of my PhD research focuses on using ReaxFF-based MD simulations coupled with mechanism-based continuum models to characterize the thermal response of the AVCOAT TPS.

In this chapter, we describe the microstructure of the composite AVCOAT TPS and prior research on the pyrolysis of phenolic resin reported by thermogravimetric analysis (TGA) experiments and ReaxFF-based MD simulations.

In chapter 8, we model the crosslinked phenolic resin molecular structure using a thermosetting algorithm in MD. A non-reactive PCFF potential is used to define crosslinks between the monomers. We then switch to the ReaxFF potential to obtain the chemical kinetics of the crosslinked phenolic resin pyrolysis. The role of the silica fibers is also examined.

In chapter 9, we develop a mesoscale model which uses the chemical kinetics obtained in chapter 8 to determine the effective surface recession rate of the phenolic microballoons in AVCOAT, as a function of temperature.

In chapter 10, we develop a continuum scale material response model based on 1D heat transfer which can reach experimentally relevant length- and time-scales. We validate the model by direct comparison with previous arc jet and wind tunnel experiments and use it to obtain the surface temperature and char thickness for the AVCOAT TPS during re-entry.

In chapter 11 we describe the future direction for research in this field, and some preliminary results for the modeling of the microstructure of the char resulting from phenolic resin pyrolysis.

7.1 Microstructure of the AVCOAT TPS

AVCOAT is a multiphase composite material made up of hollow phenol formaldehyde resin (phenolic) microballoons held together by novolac epoxy binder and reinforced by chopped silica fibers as shown in Fig 7.1.[92] The resulting composite has a 25% fiber mass fraction and a porosity of 50%. The chemical structure of the phenolic resin consists of phenol molecules connected to each other via methylene (CH_2) bridges which substitute the hydrogen at the ortho and para positions resulting in an amorphous network of interconnected rings. The novolac epoxy binder functions as a glue binding the phenolic microballoons and the silica fibers.[93]

7.2 Thermogravimetric Analysis for Phenolic Resin Pyrolysis

Thermogravimetric analysis (TGA) was performed by Trick *et al.* to quantify the mass change during pyrolysis, as a function of temperature.[94] They developed a kinetics model for the pyrolysis of phenolic/carbon pre-peg SC1008/T300 to study the manufacturing process of carbon/carbon components. From the weight loss plot of the material during high temperature treatment they predicted the reaction rates and activation energy. The reactions was shown to be proceed in separate stages which were classified by the difference in reaction rates from changes in the pyrolysis mechanism. The sample was heated from room temperature to 800 ℃ in an inert nitrogen environment at heating rates of 0.5, 1.0 and 10.0 ℃/min. Fig 7.2a shows the percent of resin remaining at various temperature for the three heating rates. From the derivative of the curve the mass loss dM/dT for heating rate of 0.5 ℃/min is shown in Fig 7.2b.

Using first order decomposition kinetics the authors attempted to reconstruct the mass loss curve as a sum of independent reactions. For each individual reaction the mass loss is governed by,

$$\int_{\xi_i}^{\xi} \frac{d\xi}{1-\xi} = \int_{T_i}^{T} \left\{ \frac{T}{dT/dt} A e^{-\frac{E}{RT}} \right\} dT \tag{7.1}$$

where, ξ is the extent of reaction at temperature T defined as the fraction of mass removed,

$$\xi = \frac{m_o - m}{m_o - m_e} \tag{7.2}$$

They decomposed the mass loss curves into four reactions, and obtained activation energy (E) of of 17.7 kcal/mol, 23.4 kcal/mol, 18.5 kcal/mol, and 47.5 kcal/mol, and the pre-exponential constant (A) ranging from 6.33×10^2 to 3.96×10^8 $1/min$. The first stage was suggested as the initial water loss, while the final stage resulted in the disintegration of the phenolic rings. The constants were shown to be independent of the heating rates. The authors acknowledge that the consensus between experimental studies of phenolic pyrolysis is poor. To illustrate the point, they use their data on previous kinetics models proposed by Anderson[95] and Friedmann[96] to obtain an activation energies of 14-160 kcal/mol and 15-170 kcal/mol respectively.

The wide disparity between the activation energies obtained from the various TGA experiments is due to variations in the techniques used to obtain mass loss curves as well as differing compositions of the material studied. More recent TGA studies have reported a three-stage pyrolysis process, with activation energies of 52.2 kcal/mol, 64.9 kcal/mol and 72.9 kcal/mol, respectively.[97] Similar activation energies were obtained by William *et al.* for high density phenolic nylon (47.7 kcal/mol) and AVCOAT 5026-H/CG (23.5 to 25.5 kcal/mol).[98] Although TGA experiments have been used for calculating the chemical kinetics of pyrolysis they cannot provide detailed quantitative understanding of the complex pyrolysis mechanisms.

7.3 Molecular Dynamics Simulations of Phenolic Resin Pyrolysis

Atomistic mechanisms associated with pyrolysis of the phenolic resin have been studied using ReaxFF-based molecular dynamics (MD) simulations. Jiang *et al*. and Desai *et al.* subjected an uncrosslinked phenolic formaldehyde resin to temperatures of 2750 to 3250 K in MD to simulate the initial stages of pyrolysis.[99,100] The simulation temperatures greatly exceed the temperatures in TGA experiments, but were adopted to computationally accelerate the pyrolysis reactions due to limitations of the MD time-scale. They demonstrated that the primary reaction product was H_2O, formed by the β elimination mechanism, while secondary products included H_2, C_2H_2, and CO. Using the number of H_2O molecules generated in the periodic MD box as the extent of reaction, Jiang *et al*. obtained the activation energy and pre-exponential constant to be 27.61-40.95 kcal/mol and $1.8 \times 10^{14}\ s^{-1}$ respectively. Fig 7.3a shown the plot of $\log(k)$ vs $1/T$ obtained from their MD simulations. The calculations assumed that the phenolic resin pyrolysis can be reduced to a single 1st order reaction, with the reaction rate following the Arrhenius law. The authors note that the elimination of H_2O from the phenolic resin chains resulted in the formation of new C-C bonds, marking the initial stages of carbonizing. Desai *et al.* replicated the simulations of Jiang *et al*., to obtained a similar composition of pyrolysis products, and an activation energy and pre-exponential constant of 24.88-34.45 kcal/mol and $1.59 \times 10^{14}\ s^{-1}$ respectively, as shown in Fig 7.3b. More recent MD simulations by Qi *et al.* demonstrated that pyrolysis of the phenolic resin at 3500 K resulted in much smaller polymer fragments than at lower temperatures of 2500 K.[101]

7.4 Figures

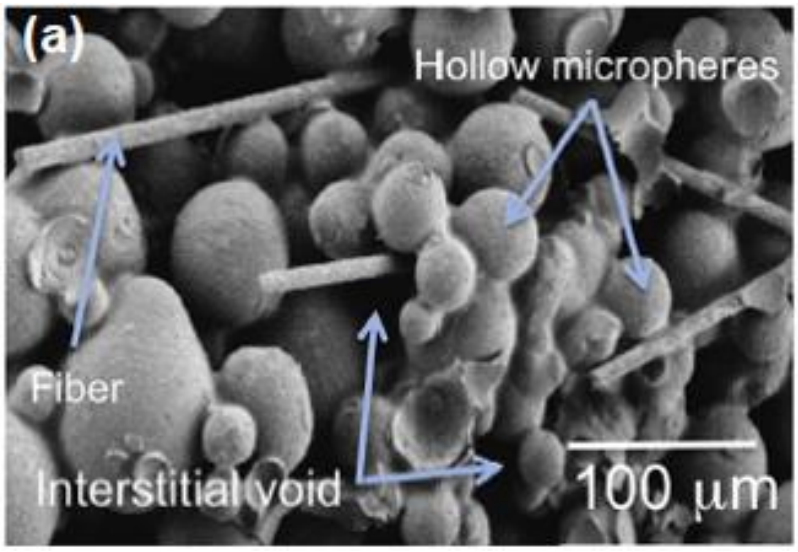

Fig 7.1: Scanning electron microscopy image of AVCOAT microstructure, comprising of a mixture of silica fibers and phenolic microballoons.[93]

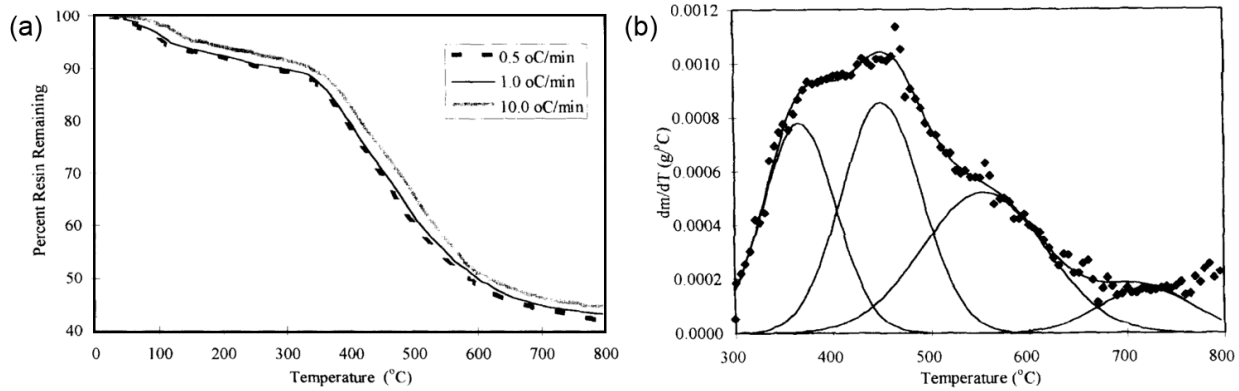

Fig 7.2: Thermogravimetric analysis of phenolic/carbon pyrolysis.[95] (a) Percent of resin remaining as a function of temperature during heating to 800 ℃ at rates of 0.5 ℃/min, 1.0 C/min and 10.0 ℃/min. (b) Rate of mass loss at heating rate of 0.5 ℃/min, and the four separate reaction curves which are fit to the rate of mass loss. The diamonds represent the data points from experiments.

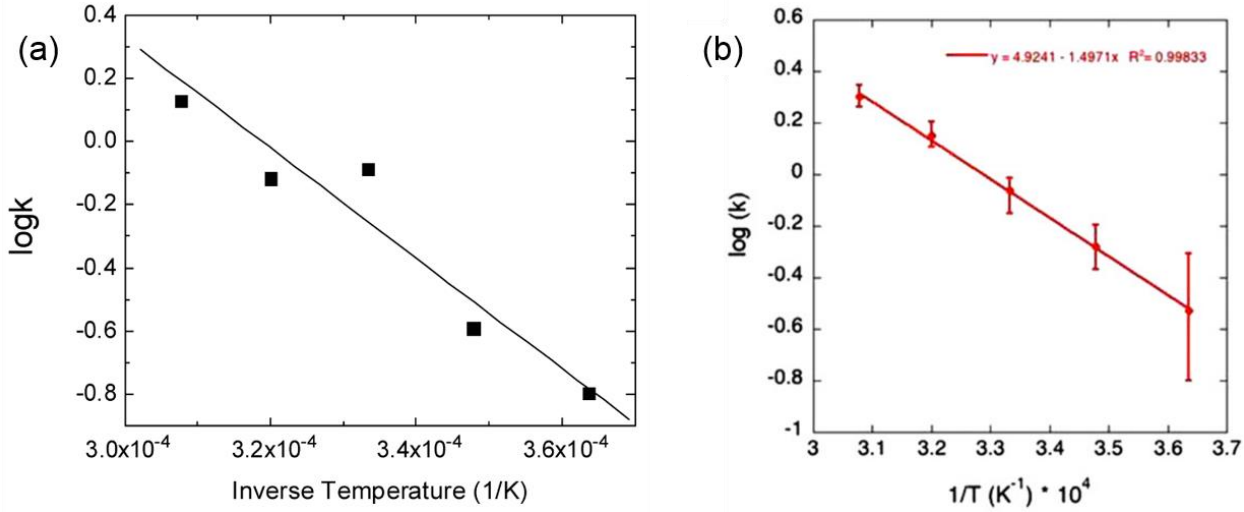

Fig 7.3: Log of reaction rate, defined as the H_2O formation rate versus inverse temperature during phenolic resin pyrolysis obtained by ReaxFF-based MD simulations by (a) Jiang *et al.*[100]and b) Desai *et al.*[101]

Chapter 8. MD Simulations for the Modeling and Pyrolysis of AVCOAT[3]

As aforementioned, AVCOAT is a polymer-based foam composite, which is composed of a porous matrix and chopped silica fibers. The matrix is in the form of microballoons made of a highly crosslinked polymer called phenol formaldehyde resin (or phenolic resin), glued together by a novolac epoxy binder.[93] In this chapter, we focus on quantifying the pyrolysis of the phenolic resin using MD simulations.

8.1 Modeling of Crosslinked Phenolic Resin

The atomic structure of the phenolic resin used in AVCOAT has a high degree of crosslinking which strongly influences its thermal and mechanical properties.[102–105] The amount of crosslinking plays an important role in the rate and composition of the char formation during resin pyrolysis.[106] The structure of the phenolic resin consists of phenol molecules connected to each other via methylene (CH_2) bridges which substitute the hydrogen at the ortho and para positions resulting in an amorphous network of interconnected rings as shown in Fig 8.1a.[107] Previous experimental and first principle calculations have shown that the para and ortho positions on the phenolic rings are equally reactive while the meta position is almost completely unreactive during curing.[108–110] Therefore in our simulations only crosslinking at ortho and para positions is considered.

All our simulations are performed using the open source package LAMMPS.[37] The modeling of the thermoset phenolic resin is achieved by using explicit bond formation algorithm on a pre-polymer mix of phenolic rings and methylene bridges mimicking the actual curing process of thermoset polymers.[111] We use the Polymer Consistent Force Field (PCFF) type potential for describing the interatomic interactions during the curing stage since they allow explicit bond definitions.[112] Non bonded interactions consist of LJ and coulombic terms. The parameters for the C, H and O interactions were obtained from the open source software

[3] Some of the results presented in this chapter have been previously published in the following publication: Harpale A., Sawant S.S., Kumar R., Levin, D. and Chew H.B. "Ablative Thermal Protection Systems: Pyrolysis Modeling by Scale-Bridging Molecular Dynamics" *Carbon,* 130 (2018): 315-324

'XenoView', a multi-purpose molecular builder and the cross terms are obtained from 'sixthpower' mixing rules.[113]

We first construct a simulation cell containing two phenol rings and three CH_2 molecules as shown in Fig 8.1b. The hydrogens on the ortho and para positions of the phenol rings are deleted to create reactive sites for crosslink formation. The system is replicated 10 × 10 × 6 times to create an ordered array of 1200 rings and 1800 CH_2 molecules in a simulation box of dimension 20.0 × 20.0 × 6.0 nm^3. Since each ring can form a maximum of three additional bonds while each CH_2 can bond with two C atoms, the stoichiometric ratio 2:3 of phenolic rings to CH_2 molecules chosen here maximizes the crosslinking efficiency. Periodic boundary conditions are implemented in the *x* and *y* direction while reflecting walls are enforced in the z direction. The wall prevents the bonded molecules from straddling the *z* axis, which will be a matter of importance when the vacuum layer is introduced in the *x* direction to model the slab boundary conditions. The system is heated to 1000 K for 1000 ps using the Berendsen thermostat with damping constant of 50 fs in, to randomize the positions and orientations of the phenol rings in the pre-polymer mix. The density is raised from the current 0.25 g/cc to the target density of 1.20 g/cc by deforming the simulation box in the x and y dimensions resulting in a simulations box of dimensions 5.5 × 5.5 × 6.0 nm^3. The compression is performed gradually over 1000 ps with the temperature maintained at 1000 K to mitigate any local residual stress. Finally, the pre-polymer mix is subjected to the curing stage for another 1000 ps. Bonds are added between the reactive sites in the ortho and para positions of the phenolic rings and the C atoms on the CH_2 molecules. Every 10 steps the distance between all possible bonding C atoms is checked and a permanent bond is added is it less than the cutoff of 0.3 nm. The bonds formation is constrained to prevent a CH_2 molecule from saturating more than one site on the same phenol rings (self-linking). Self-linking of chains limits the number of terminal rings and reduces crosslinking efficiency. Due to the difference between the C-C bond creation cutoff of 0.3 nm and the equilibrium distance of 0.152 nm, each newly created bond adds 1854 kcal/mol of energy to the system. In order to prevent spikes in temperature a Berendsen thermostat is implemented on the phenolic rings, set to a target temperature of 800 K. The final atomic structure is minimized using the conjugate gradient method. We determine that a total of 1117 new C-C bonds are formed during the curing stage. A time step of 0.2 fs is used during the simulation. Fig 8.2 shows the C atoms and C-C bonds in the MD box before and after the curing stage.

The efficiency of the algorithm is measured by the degree of crosslinking achieved at the end of the curing stage. While various methods have been previously used to characterize a crosslinked polymer, we define the degree of crosslinking as the fraction of reactive sites on the phenolic rings that are saturated by C-C bonds.[107,114,115] Fig 8.3a shows the degree of crosslinking increases rapidly during the curing stage, reaching a steady state value of $D = 0.931$. For comparisons, based on our definition, a phenolic resin consisting of a purely linear chains (ortho-ortho-novolac) has a degree of crosslinking of $D \sim 0.66$ while a fully bridged system has a value of $D = 1$. We also track the size of the largest cluster during the curing stage and observe that it percolated the length of the simulation box. During polymer condensation reaction the gel point is identified as the time instance when the second largest cluster in the system reaches its peak size and begins to shrink.[116] In our simulations the gel point is reached within the first 100 ps of the curing stage. At the end of the curing, the largest cluster contains 99.64 % of the atoms in the system. After the simulation the atoms which are not connected to the largest cluster are deleted. It should be noted that while the polymerization algorithm described here is derived from the mechanism of thermosetting of phenol in the presence of formaldehyde, it does not attempt to capture the kinetics of the process. Using a non-reactive potential and bond creation technique, our goal is simply to obtain the final molecular configuration of the crosslinked phenolic resin.

8.2 Chemical Kinetics of Phenolic Resin Pyrolysis

After the curing process, we adopt a reactive-force-field (ReaxFF) potential, in place of the PCFF potential, to allow for dynamic bond breaking and reformation during pyrolysis of the phenolic resin.[117] This ReaxFF potential has been specifically calibrated to simulate high temperature gas phase oxidation of hydrocarbons, and has been extensively validated against quantum mechanical (QM) calculations. We insert a 12-15 nm thick vacuum layer in the *z* direction of the simulation box to model the free-surface of the phenolic resin (Fig 8.3b). We minimize the system using the conjugate gradient method and equilibrate it at a temperature of 300 K. We impose a (small) bi-axial pressure of 10 atm at 300 K for 12.5 ps along the *x* and *y* directions of the simulation box to allow minor atomic reconfigurations and mitigate local

residual stresses. The density of our phenolic resin model system is observed to reach a steady-state value of 1.25 g/cc, which is in good agreement with previous studies.[105]

Endothermic pyrolysis occurs when a thermoset phenolic resin sample is heated at high temperatures. To study the pyrolysis kinetics, we fix the bottom 0.5 nm layer of atoms and subject the 5 nm thick slab of atoms above to the targeted pyrolysis temperature (500 to 2300 K) which is maintained by a Berendsen thermostat for 500 ps. The atoms very close to the surface (0.5 nm) are not included in the thermostat to prevent local temperature fluctuation caused by higher compliance at the surface. Over the course of the simulations the Berendsen thermostat was reassigned every 15.0 ps to exclude the fragments which dissociate from the main cluster of atoms in order to prevent spurious deviations from the target pyrolysis temperature. The time step is fixed at 0.25 fs during the entire simulation. During the pyrolysis, the bonds in the phenolic resin gradually dissociate. The fragments released from the decomposition diffuse within the bulk and diffuse out of the surface toward the $+z$ direction. The top 3.0-6.0 nm of the simulations box is designated the reservoir where the atomic fragments are trapped (larger reservoir used for higher temperatures).). A combination of a unidirectional region ('*oneway*' command in LAMMPS) and a reflecting wall is used to implement the reservoir region in the simulation box.[37]

Fig 8.4 shows snapshots of the atomic configurations of the phenolic resin at temperatures of 500 K to 1500 K after 500 ps of heating, and at temperatures of 1800 K to 2300 K after 250 ps of heating. Longer time simulations were conducted for the former because of the significantly slower pyrolysis reactions. Observe that the phenolic resin remains stable at temperatures of 500 K, while pyrolysis fragments are only observed at temperatures of 800 K and above. This suggests that pyrolysis of the phenolic resin starts at temperatures of ~ 500 K to 800 K, in agreement with TGA data which report the onset of mass loss of phenolic resin at ~ 500 K.[95] Increasing number of pyrolysis fragments are observed at higher temperatures. No appreciable recession of the surface is observed during the MD simulations at temperatures of up to 2000 K. Time-trace of the pyrolysis fragments at 1800 K shows that these fragments, comprising of mostly 2-3 atom clusters, originate homogeneously from within the bulk, with no preferential dissociation at the resin surface. At temperatures of 2300 K, which is in the range of the maximum reentry temperatures experienced by the surface of ablative TPS, larger clusters of

the phenolic resin (>10 atoms) are now removed from the surface to form incipient surface cracks, which suggests the onset of surface spallation. Our simulations show that these larger clusters typical of spallation originate from nearer the surface, while smaller 2-3 atom clusters typical of pyrolysis fragments originate deeper in the polymer. Hence, our MD simulations reveal distinct transitions in the pyrolysis mechanisms with temperature: from onset of pyrolysis at ~ 500 K to 800 K, to potentially the onset of spallation at ~ 2300 K and beyond.

The pyrolysis process initiates with the formation of a large number of H_2O molecules, produced by two predominant mechanisms. In the first mechanism shown in Fig 8.5a-i, –OH functional groups on neighboring phenolic rings interact at high temperatures, breaking one O–H bond in the process (labeled in red) to allow the other –OH group (labeled in blue) to react with the released H atom to form H_2O and a C-O-C ether linkage. The second mechanism is the well-established β elimination process shown in Fig 8.5a-ii, where the –OH functional group on one phenolic ring (labeled in blue) combines with a H atom on adjacent or remote CH_2 bridge sites (labeled in red) to release H_2O. Similar H_2O formation mechanisms have been reported for pyrolysis of an uncrosslinked phenolic resin.[99] These MD simulation results closely-corroborate with TGA data which detect the presence of water vapor during early-stage pyrolysis of the phenolic resin.[94]

We trace the evolving number of H_2O molecules released by pyrolysis of the phenolic resin model at 1800 K in Fig 8.5b, as well as the total number of C, H, and O atoms released and trapped within the reservoir during the pyrolysis simulation in Fig 8.5c. The count of the number of H_2O molecules released appears to saturate at ~ 400 ps (Fig 8.5b). However, the number of C atoms released still continues at a constant rate (Fig 8.5c), implying that the pyrolysis reaction has now transitioned to the steady-state dissociation of C-C bonds. The removal of –OH functional groups and –H atoms to release H_2O during early-stage pyrolysis significantly weakens the C-C bonds within the phenolic ring network (Fig 8.6a). Continued heating breaks these weakened C-C bonds, opening up the phenolic ring to form linear polymer sections (Fig 8.6b). Subsequent breaking of C-C bonds within the polymer chain network releases C-C fragments (Fig 8.6c).

We quantify the kinetics of pyrolysis by condensing the process into a single first order reaction. Since the final stages are characterized by C-C bonds breaking we define the extent of reaction using the average coordination number of the C atoms in the system. The values decrease in an exponential fashion as the reactant concentration decreases. The reaction rate constant at each temperature is calculated by fitting a least error exponential function. The term in the exponent is used to calculate the reaction rate constant, $r(T)$. Based on the Arrhenius equation the reaction rate varies with temperature as,

$$r(T) = Be^{-E_a/(RT)} \tag{8.1}$$

where E_a is the activation energy, *R* is the universal gas constant, *B* is the exponential pre-factor, and *T* is the pyrolysis temperature. Note that during the calculation of the number of C-C bonds the entire system is considered, without excluding the 3-5 nm reservoir at the top of the simulation box. Since the C-C bonds can release fragments containing intact bonds, the methods is not biased towards the position of the C-C bond in the polymer chain. In other words, a bond dissociation towards the terminal end of the polymer chain (which will release a small fragment) will result in the same decrease in the total bonds count as a dissociation further away from the terminal chain (resulting in a large fragment).

Fig 8.7 shows the near-linear variation of $\ln(r)$ versus $1/T$ as obtained from our MD simulations, which suggests that the rate of pyrolysis, defined by the rate of C-C bond breaking, indeed follows the Arrhenius relationship. From the slope and *y*-intercept of the best fit line we obtain activation energy and exponential pre-factor of $E_a = 42.5$ kcal/mol and $B = 5.24 \times 10^{12}$ s^{-1}, respectively. Our calculated E_a value is quantitatively in good agreement with those obtained from TGA analysis of the final pyrolysis stages of carbon-phenolic composite (47.5 kcal/mol)[94], high-density phenolic nylon (47.7 kcal/mol)[98], and AVCOAT 5026-H/CG (23.5-25.5 kcal/mol)[98]. Notably, our activation energy for phenolic pyrolysis is slightly elevated compared to previous MD simulation results of Jiang *et al.* (27.6-41.0 kcal/mol)[99] and Desai *et al.* (24.9-34.5 kcal/mol)[100] presumably because of the absence of crosslinking in these prior studies. Furthermore, these MD studies primarily focused on the early stages of pyrolysis, and adopted the rate of removal of H_2O molecules rather than C-C bond dissociation as the criterion to quantify the reaction rate. We remark that raising the temperature of the complex multistep

reaction to 2750-3250 K to accelerate the pyrolysis rates in MD, compared to actual pyrolysis temperatures of 500-2300 K, could have triggered the onset of other thermal decomposition reactions, such as spallation.[80]

8.3 Thermochemical Properties of Phenolic Resin

In this section we use MD simulations to calculate the thermochemical properties, specifically, the thermal expansion coefficient (α^r), heat of pyrolysis (h_p^r), thermal conductivity (k^r) and specific heat capacity (C_p^r). By comparing these parameters to experimentally reported values, we validate the transferability of the ReaxFF potential for modeling of phenolic resin. Further, some of the parameters calculated here will be used to inform larger scale models in later chapters.

For the calculation of thermal expansion coefficient (α^r), we consider the fully periodic MD box containing the crosslinked phenolic resin. The potential is switched from PCFF to ReaxFF, but the vacuum is not introduced in the *z* direction. We equilibrate the periodic system using a NPT ensemble with pressure of 1 atm and temperature ranging from 200-800 K for 12.5 ps. Fig 8.8a shows the specific volume of the phenolic resin obtained from MD at various temperatures. From the slope of the curve the linear thermal expansion coefficient is calculated to be $\alpha = 56.24 \times 10^{-6}\ \mathrm{K}^{-1}$ in close agreement with the experimental value of $(55 \pm 5) \times 10^{-6}\ \mathrm{K}^{-1}$ reported by Mottram *et al.*[118]

We use the direct method to estimate the thermal conductivity (k^r) of phenolic resin.[119] The goal is to extract the temperature profile using MD simulations for an equivalent 1D problem which can be compared with its analytical solution. A 12 nm long (along the *z* axis) periodic MD box containing crosslinked phenolic resin is first heated to 100 K for 10 ps using the Berendsen thermostat. At a time instant defined as $t = 0$ the ends (1 nm of each side) are set to 0 K using the Berendsen thermostat, which the temperature control over the rest of the MD box is removed. Due to conduction the entire 12 nm system will gradually cool down to 0 K, as heat flow (into the quenched ends). Since the heat flow is purely in the *z* direction, this can be modeled using 1D conduction equation. The temperature of the center of the block (1 nm wide

strip) is monitored and plotted again time as shown in Fig 8.8b. By solving the 1D heat equation we calculate the temperature of the center of the rod,

$$T(t) = \frac{4T_o}{\pi} e^{-\frac{\pi^2 k^r t}{C_p^r \rho^r L^2}} \tag{8.2}$$

For $T < T_o/2$. Where $T_o = 100\ K$ is the initial temperature of the material. By fitting the exact solution to the MD derived curve we obtain, $k^r = 0.279$ W/mK. Experiments performed by Mottram *et al.* on phenolic SC-1008 composites obtain thermal conductivity ranging from 0.21 to 0.37 W/mK.[120,121] Note that the method described here assumes the phenolic resin to be homogenous and isotropic, with a thermal conductivity which is independent of temperature.

For estimating the heat capacity $\left(C_p^r\right)$, the temperature of the resin in the MD box is raised from 0 K to 900 K over 150 ps using a Berendsen thermostat. The total internal energy (Q) is measured as the net internal energy per units mass. The heat capacity defined as, $C_p^r =$ dQ/dT, is computed to be 3280.7 J/kgK. Titov *et al.* estimate the heat capacity of the gaseous pyrolysis product to be 2093.4 J/kgK.[122] Since we model the solid phenolic resin here, the value of thermal conductivity is expected to be higher.

Heat of pyrolysis $\left(h_p^r\right)$ is calculated as the difference of net potential energy per unit mass between the pyrolysis products in the reservoir and the initial system. The difference is calculated at three points during the pyrolysis simulations, at $\mathrm{t} = 50, 100, 150$ ps for pyrolysis temperature of 1500 K, 1800 K and 2000 K. From the average of the nine data points we obtain, $h_p^r = 1578.5 \pm 153.04$ KJ/Kg**.**

8.4 Structure and Role of Silica fibers

The simulations so far consider the pyrolysis of phenolic resin without considering the silica fibers which constitute the reinforcement in AVCOAT. It is believed that the silica fibers remain inert during the AVCOAT pyrolysis and are removed by mechanical ablation of the flow instead of thermal decomposition. To test this hypothesis we perform pyrolysis simulations on

silica using a methods which is similar to those described in section 8.2. Silica fibers in AVCOAT are in the form of amorphous SiO_2. We generate the amorphous SiO_2 atomic structure using the liquid-quench methods, typically employed for generating glassy systems. A 4.2 x 4.9 x 5.2 nm crystalline alpha quartz lattice is generated in a fully periodic MD simulation box. The Si and O atoms are governed by same the ReaxFF potential, employed in Part I of the dissertation.[38] The system temperature is linearly ramped using the Berendsen thermostat from 300 K to 6000 K over 60 ps to melt the SiO_2 and hence break the ordered arrangement of the atoms in the crystal. We then gradually reduce the temperature down to 300 K over 90 ps to allow the Si-O bonds to reform, in a disordered manner which results in an overall amorphous configuration. The pressure in the box is equilibrated using the NPT ensemble to relieve any residual stresses. Fig 8.9 shows the initial (crystalline) and final (amorphous) SiO2 atomic structure.

For the pyrolysis simulation the *z* boundary condition is switched from periodic to fixed and a vacuum of 5.0 nm is introduced in the *z* direction to model a free slab. The bottom 0.5 nm are held fixed to model a bulk and the next 3.0 nm are set as the heat bath. The system is first equilibrated for 75 ps, at 373 K to mitigate any surface stresses. The heatbath is then set to a temperature of 1000-5000 K for 150 ps to determine the pyrolysis properties of the SiO_2. We observe that unlike the phenolic resin, the amorphous SiO_2 melts before any visible surface degradation. Very few atomic fragments are generated at temperature less than 4500 K, over the 150 ps duration. However as the temperature reaches 5000 K, the entire system sublimates with fragments uniformly dispersed in the MD box. From this finding we confirm the inertness of the silica fiber in AVCOAT at re-entry temperatures, with gradual softening and melting being the relevant mechanism of removal during re-entry as previously speculated.[90]

8.5 Summary

In this chapter, we model the atomic structure of the crosslinked phenolic resin, which is commonly used as matrix material for ablative TPS, using the PCFF potential by adding explicit bonds between the phenolic rings. The polymer was then subjected to temperatures of 500 – 2300 K using MD simulations employing the reactive force field potential (ReaxFF), to

determine its pyrolysis kinetics. The activation energy and rate constant for thermal decomposition was obtained as $42.54\ /\mathrm{mol}$ and $5.24 \times 10^{12}\ \mathrm{s}^{-1}$ respectively, in agreement with previous experimental and theoretical findings. The role of the silica fibers was examine by first modeling an amorphous SiO_2 structure using the liquid quench methods, follows by high temperature MD simulations. We demonstrated that the silica fibers remain inert at pyrolysis temperatures.

8.6 Figures

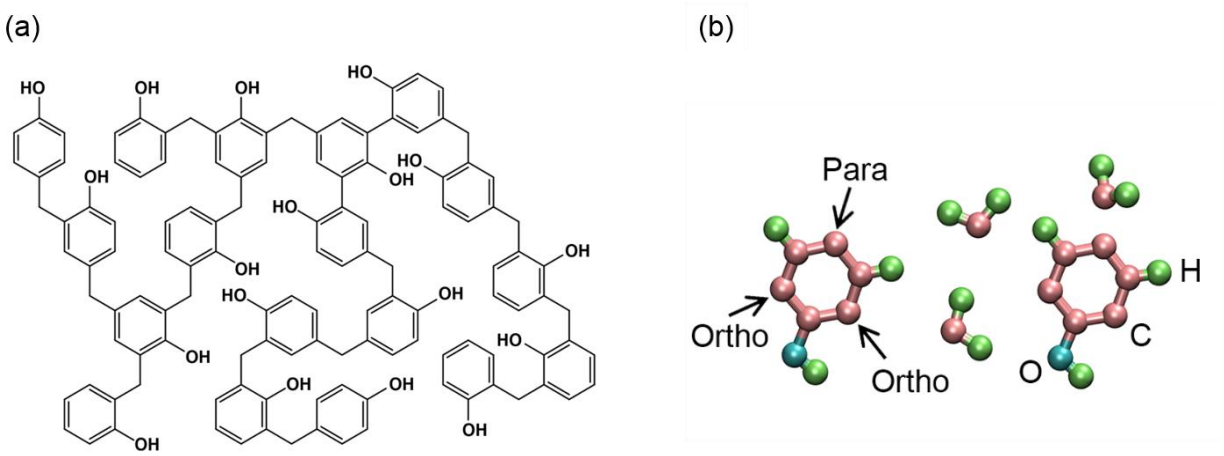

Fig 8.1: (a) Chemical structure of crosslinked phenol formaldehyde (phenolic) resin. (b) Unit cell containing three CH_2 molecules, and two phenolic rings with reactive para and ortho sites for crosslink formation.

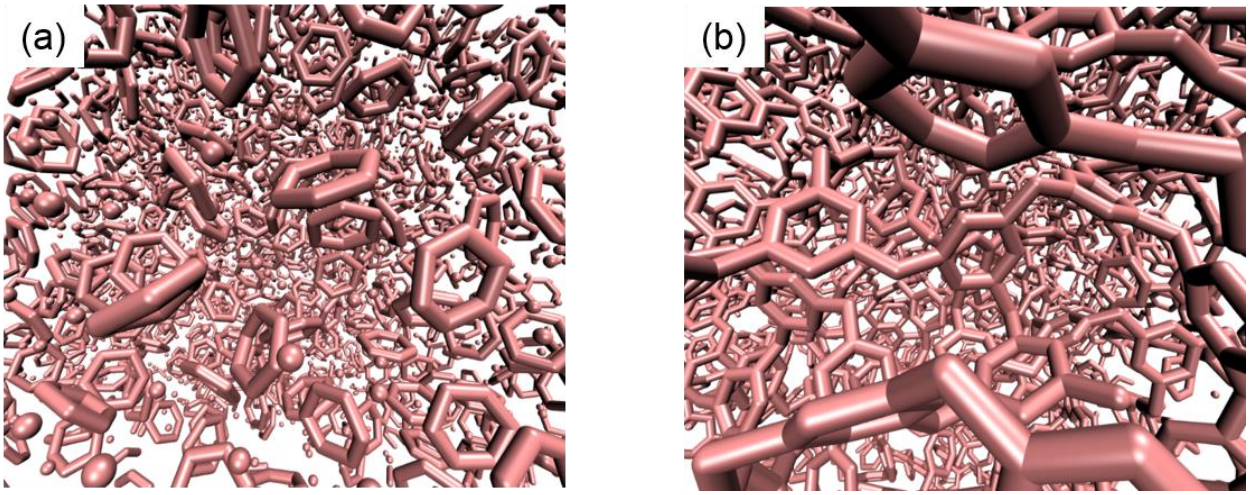

Fig 8.2: C atoms and C-C bonds in the MD box (a) before and (b) after the curing stage used to model the molecular structure of the crosslinked phenolic resin.

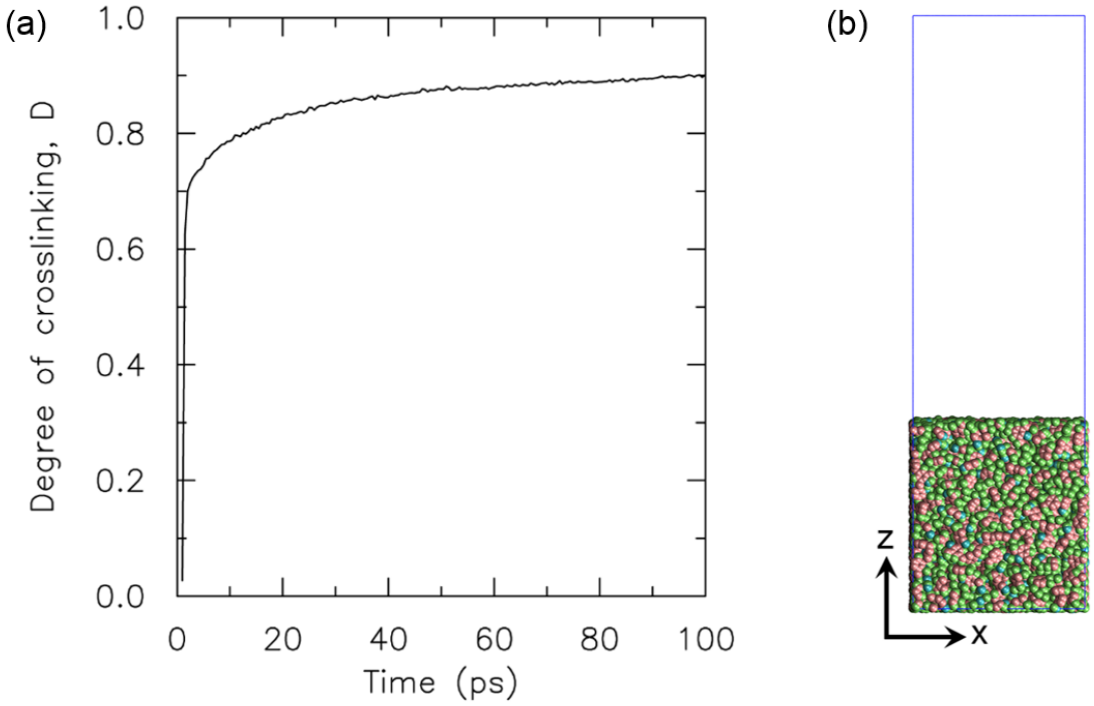

Fig 8.3: (a) Evolution of the degree of crosslinking (D) with time during the curing stage of the thermosetting simulations. The crosslinking is defined as the fraction of reactive sites on the phenolic rings that are saturated by C-C bonds. (b) Atomic configuration of the final crosslinked phenolic resin model structure. C, O and H atoms are colored pink, blue, and green, respectively.

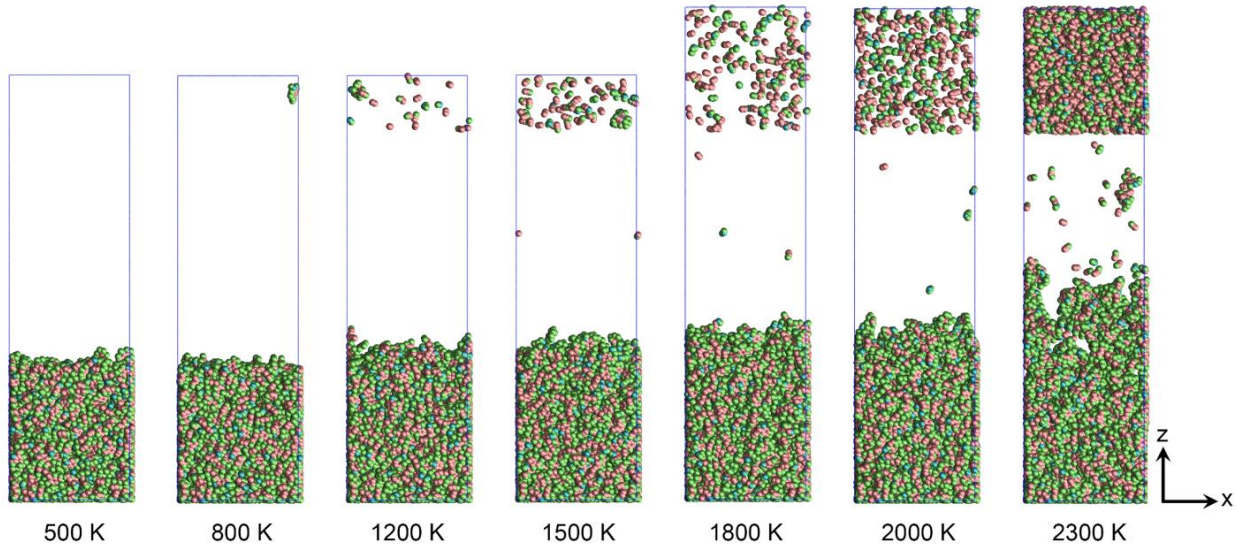

Fig 8.4: Snapshots of the atomic configurations of the phenolic resin model structures at temperatures of 500 to 1500 K after 500 ps of heating, and at temperatures of 1800 to 2300 K after 250 ps of heating. Fragments emerging from the bulk are trapped in the reservoir at the top vacuum region of the simulation box.

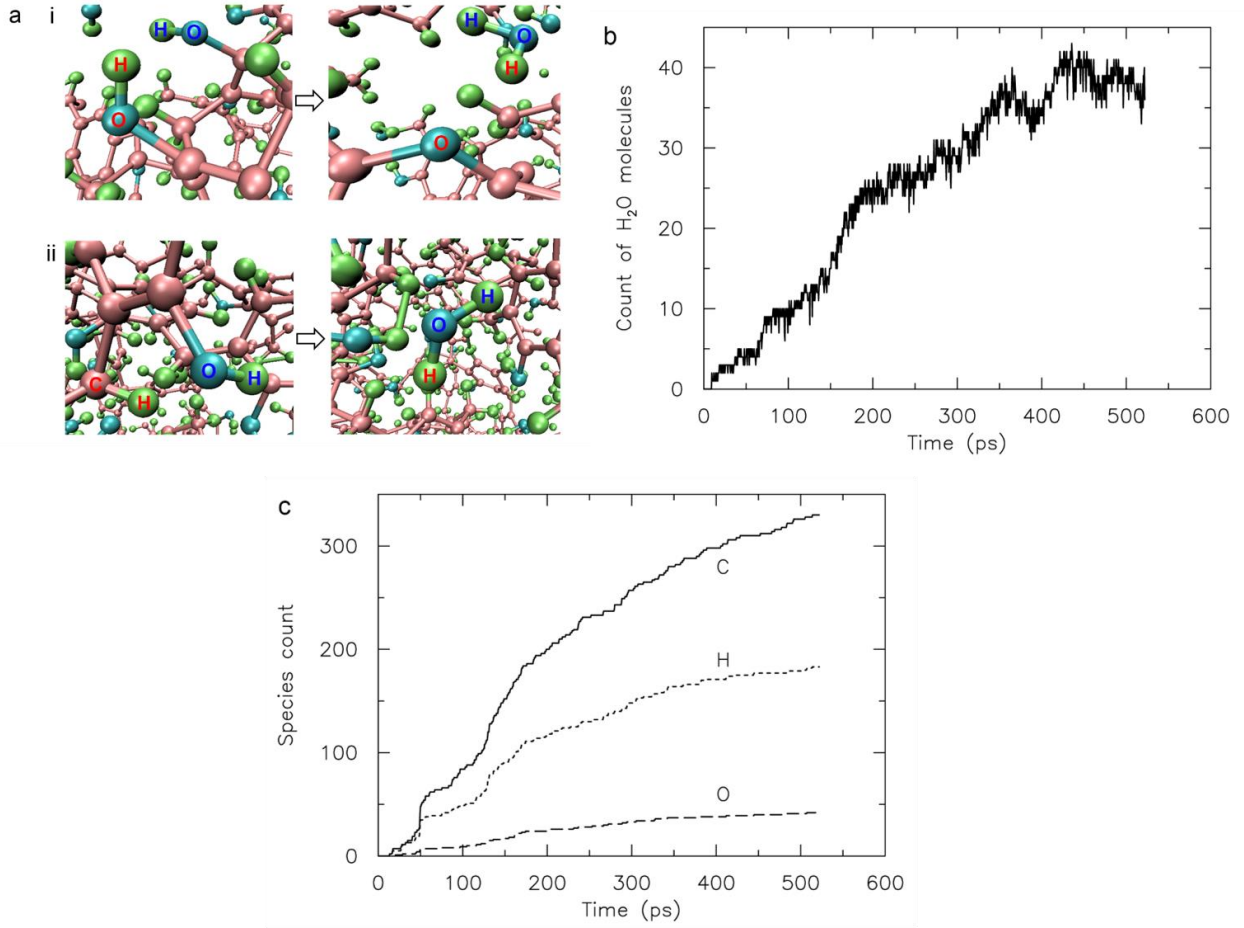

Fig 8.5: (a) Two dominant mechanisms of H_2O formation from early-stage pyrolysis. (b) Count of the evolving number of H_2O molecules from pyrolysis at 1800 K. (c) Count of the evolving number of C, H, and O atoms in the fragments released during pyrolysis at 1800 K.

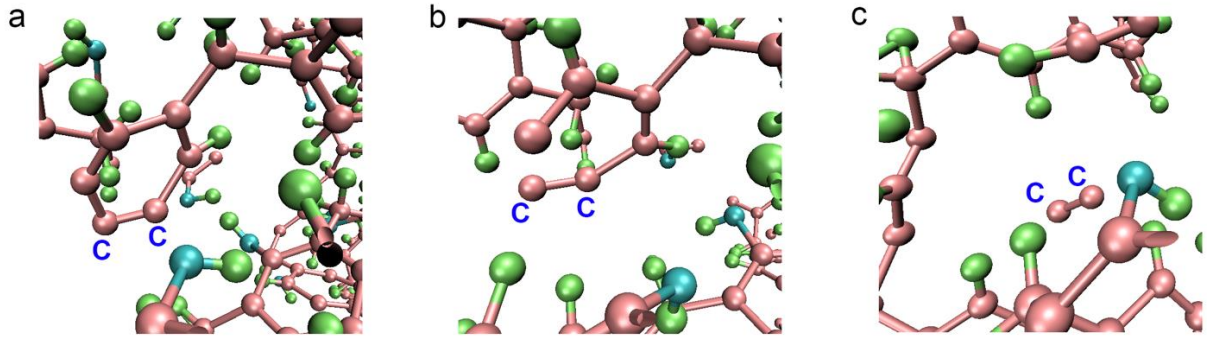

Fig 8.6: Sequential C-C bond breaking process after –H and –OH removal to release a C-C fragment during pyrolysis process.

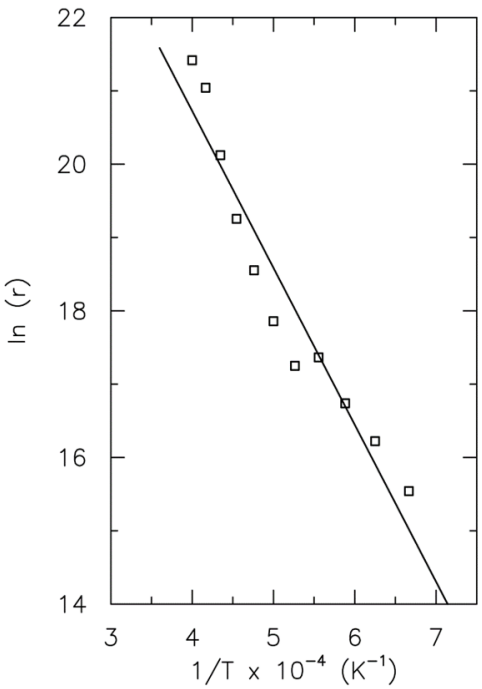

Fig 8.7: Arrhenius plot for determination of activation energy (E_a) and rate constant (B) governing the rate of dissociation of C-C bonds during pyrolysis. Symbols denotes the pyrolysis reaction rates from MD simulations at various temperatures

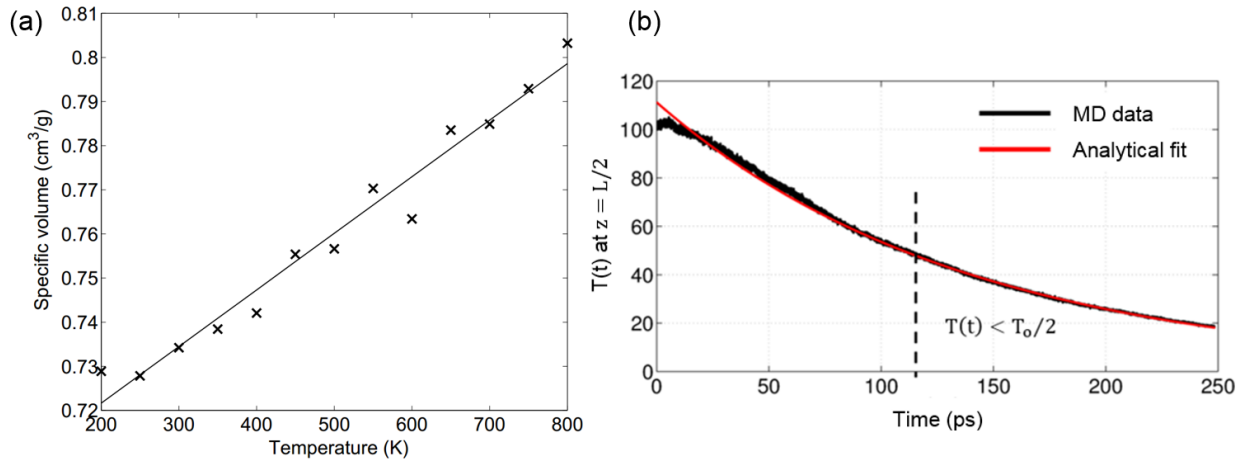

Fig 8.8: Calculation of thermophysical properties of phenolic resin using MD simulations. (a) Specific volume change of the crosslinked phenolic resin with temperature. The curve is used to determine the thermal expansion coefficient. (b) Temperature of the center of a 1D rod cooled from 100 K, by quenching to ends to 0 K. The black and red curves are the MD and analytical plots respectively. Using an exponential fit, the thermal conductivity is calculated.

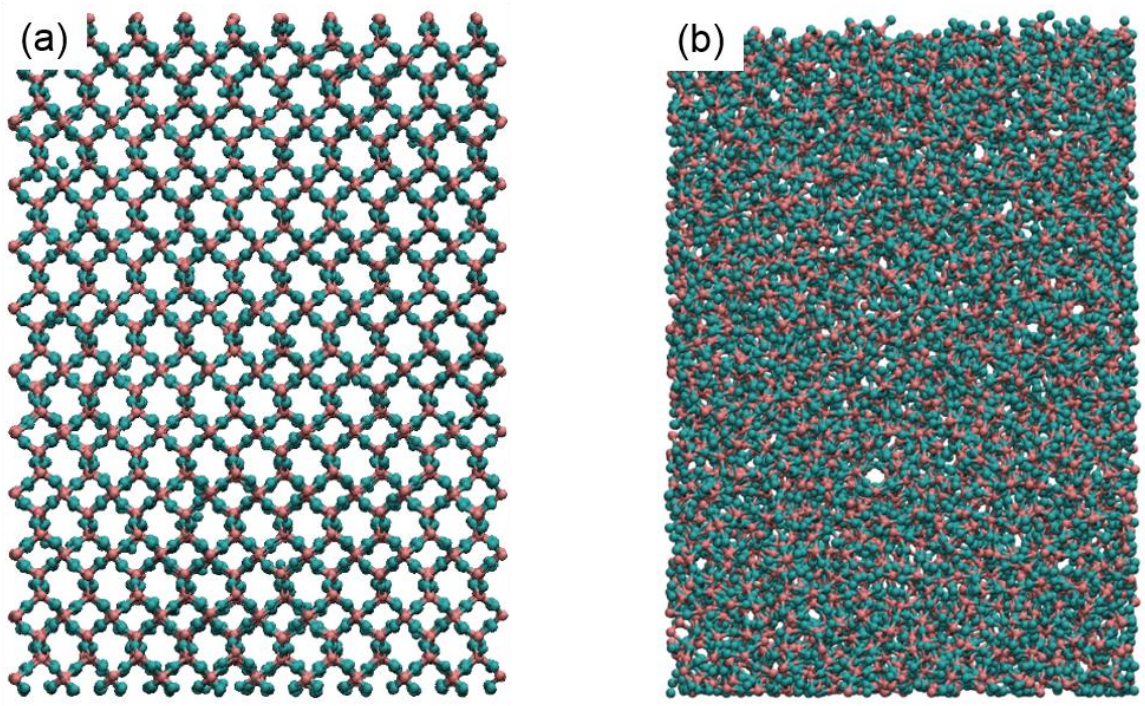

Fig 8.9: Modeling of silica fibers. (a) Initial α quartz crystalline configuration for SiO_2. (b) The atomic structure of amorphous SiO_2 formed by the liquid quench process. Si and O atoms are colored in pink and cyan respectively

Chapter 9. Surface Recession Rate for Phenolic Resin

The MD simulations in chapter 8 captured the pyrolysis of bulk phenolic resin and its dependence on temperature. At macroscopic lengths scale however, the material surface is subject to a heat flux giving rise to a temperature gradient though the bulk. Using a thermochemical model we propose a quantitative relationship for the surface recession rate as a function of the surface temperature of the phenolic resin. During the Apollo era several thermochemical models were proposed largely relying on either experimentally derived or empirical pyrolysis parameters, which resulted in wide variation in reported results.[90,123,124] For instance, Kemp calculated the ablation rate of a Teflon surface as ~ 10 mm/s at 1200 K while Steg used a different approach to determine the recession rate as ~ 3 mm/s.[90,123] The disagreement between the values reported arise due to the difference in the theoretical formulation as well as the parameters used. For example the values of the exponential pre-factor (B) of Teflon pyrolysis used in the above mentioned studies differ by an order of magnitude.

Building on 1-D analytical expressions motivated by Steg,[90] Scala,[124] and Kemp,[123] we calculate the effective surface recession rate during bulk pyrolysis of the phenolic resin based on our MD-derived values of E_a and B. Note that this surface recession rate essentially refers to the rate at which monolithic phenolic resin pyrolyzes and gets converted to char, and is distinct from the recession rate of the actual heat shield material caused by ablation. Consider the surface of a phenolic resin substrate subjected to a temperature T_s which is receding at a constant steady-state velocity V_{s0}, as schematically shown in the inset of Fig 9.1. In the moving coordinate system that recedes with the substrate surface ($y = 0$), we define a control volume of unit cross-sectional area extending from the cool region in the substrate (large negative y) where no pyrolysis occurs, i.e. at temperature of T_0 = 500 K, to any value y in the hot region (small negative y). Relative to the control volume, a mass flux of solid m_{s0} with enthalpy h_{s0} enters the cool (bottom) surface of the control volume, while mass fluxes of combined solid and gas, m_s and m_g, with enthalpies, h_s and h_g , respectively, pass through the hot (top) surface. From conservation of mass and energy,

$$m_s + m_g = m_{s0}$$

$$m_g h_g + m_s h_s - m_{s0} h_{s0} = k^r \frac{dT}{dy} \tag{9.1}$$

where k^r is the thermal conductivity of the phenolic resin. Complete pyrolysis occurs at the receding surface, i.e. $m_s = 0$ at $y = 0$, and the boundary condition can be expressed as

$$k^r \frac{dT}{dy}\Big|_{y=0} = m_{s0}\left(h_g - h_{s0}\right) = m_{s0}\left[C_p^r(T_s - T_0) + h_p^r\right] \tag{9.2}$$

where C_p^r and h_p^r are specific heat capacity and the enthalpy of pyrolysis for the phenolic resin, respectively. Performing a first-order Taylor series expansion of temperature T about $y = 0$,

$$T = T_s(1 + bT_s y) \tag{9.3}$$

and substituting Eqn 9.3 in Eqn 9.2 , we obtain,

$$b = m_{s0}\left[C_p^r(T_s - T_0) + h_p^r\right]/\left(k^r {T_s}^2\right) \tag{9.4}$$

Assuming T varies linearly in the bulk per Eqn 9.4, and C_p^r, k^r, and h_p^r do not significantly change with temperature, we estimate the pyrolysis start depth by substituting $T = T_0$ in Eqn 9.4,

$$\delta = (1 - T_0/T_s)/(bT_s) \tag{9.5}$$

The decomposition kinetics governing the pyrolysis of the phenolic resin from solid to gas is governed by the first-order Arrhenius relation. Re-expressing the reaction rate constant $r = -\frac{1}{\rho^r}\frac{dm_s}{dy}$, with the phenolic resin density of $\rho^r = 1.25$ g/cc, we get,

$$m_{s0} = -\int_{-\delta}^{0} \rho^r B e^{-E_a/(RT)} dy \tag{9.6}$$

Finally, the surface recession rate $V_{s0} = m_{s0}/\rho^r$ is obtained by substituting b from Eqn 9.4 in Eqn 9.5 and Eqn 9.3, and then substituting the expression for δ and T in Eqn 9.6, we get,

$$V_{s0} = \int_{\frac{-k^r T_s}{\rho^r V_{s0}\left[h_p^r + C_p^r\,(T_s - T_0)\right]}\left(1 - \frac{T_0}{T_s}\right)}^{0} B \exp\left(\frac{-E_a}{RT_s\left\{1 + \frac{\rho^r V_{s0}\left[h_p^r + C_p^r\,(T_s - T_0)\right]y}{k^r T_s}\right\}}\right) dy \tag{9.7}$$

A simplified closed form solution can be obtained if the surface temperature remains close to the pyrolysis start temperature $T_s/T_0 \sim 1$

$$V_{s0} \cong \sqrt{\frac{\left\{1 - e^{-\frac{E_a}{RT_s}\left(1-\frac{T_0}{T_s}\right)}\right\}\left\{Be^{-\frac{E_a}{RT_s}}\right\}Rk^r T_s^2}{\left[h_p^r + C_p^r(T_s - T_0)\right]E_a\rho^r}} \tag{9.8}$$

The exact governing integro-differential equation does not have a closed-form solution. Using MD-derived values for h_p^r (1578.5 kJ/kg), k^r (0.279 W/mK), and C_p^r (3280.7 J/kgK) based on the ReaxFF potential, we solve the exact governing equation (Eqn 9.7) numerically to obtain the variation of surface recession rate V_{s0} with surface temperature T_s, as shown in Fig 9.1. The integral on the right hand side of Eqn 9.7 is solved using a 50 point gauss quadrature method.

9.1 Figure

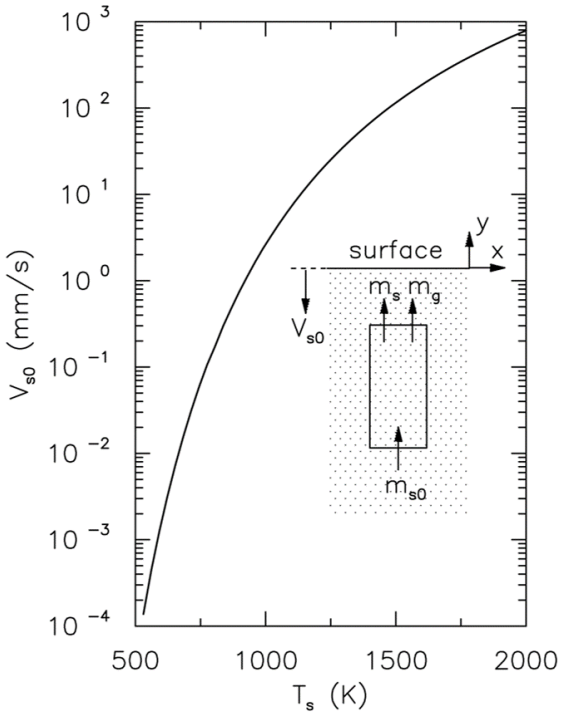

Fig 9.1: Surface recession rate V_{s0} versus surface temperature T_s induced by pyrolysis of monolithic phenolic resin.

Chapter 10. Continuum Scale Material Response Modeling

The surface recession rate V_{s0} (Fig 9.1) derived from MD simulations is for monolithic phenolic resin. The microstructure of the ablative TPS AVCOAT, is far more complex. AVCOAT TPS is a multi-phase syntactic foam material comprising of a mixture of silica fibers and phenolic microballoons, which are held together by novolac epoxy binder. The material has a porosity of $f_o^v = 0.5$ and incorporates two types of voids: those within the hollow microballoons, referred to as reinforced voids, and the space between the micro-balloons that are not filled by the binder, known as interstitial voids.[92] This highly porous material has an overall density of ρ^v = 0.51 g/cc, which is 2.5-fold lower than the bulk density of ρ^r = 1.25 g/cc for monolithic phenolic resin. During spacecraft reentry, heat is absorbed by endothermic thermal decomposition of the phenolic microballoons, and removed as the material ablates away. The release of pyrolysis products and gases as a result alters the boundary layer chemical composition and blocks atomic oxygen and nitrogen from further contact with the microstructure. In addition, the decomposition of the phenolic resin yields an emissive char residue with 60% higher porosity of $f_o^c = 0.8$, which thermally insulates the interior virgin material.[98] The silica fibrous fillers, on the other hand, remain chemically inert at the pyrolysis temperatures of 500-2300 K, but are also responsible for heat conduction into the material.[125] Here, we present a thermal response model of the AVCOAT TPS, which accounts for pyrolysis of the phenolic resin as it gets converted to char.

10.1 Formulation

The pyrolysis process results in the formation of three distinct layers: (a) charring layer at the top, (b) pyrolysis zone in the middle where resin decomposition reactions releasing the pyrolysis gases are actively occurring, and (c) intact virgin AVCOAT layer. Scanning electron microscopy (SEM) imaging in Fig 10.1a shows that the microballoons have an estimated initial outer radius of $r_o = 25$ μm.[92] Assuming closed-packing of the microballoons (i.e. packing fraction of $\frac{\pi}{3\sqrt{2}} \sim 0.74$), and by accounting for the 25% weight proportion (M_f^v) of the inert silica fibers (fiber density of 2.4 g/cc) in AVCOAT,[125] the inner radius of the microballoons can be

estimated to be $r_i = 20.4$ μm. Note that the calculated effective shell thickness of the microballoons, $r_0 - r_i$, also includes the epoxy binder content in AVCOAT, and assumes epoxy and phenol have similar pyrolysis rates. Within the pyrolysis zone, the surface of each individual microballoon recedes from r_o to r_i with surface recession rate $V_{s0}(T,t)$. This results in a change in shell thickness of $t_p(T,t) = \int_0^t V_{s0}(T,t)\,\mathrm{d}t$, as the microballoon gets converted to char. The extent of pyrolysis can thus be defined as

$$\begin{aligned} &\xi = 1 - \left\{\left[\left(r_o - t_p\right)^3 - r_i^3\right]/(r_o^3 - r_i^3)\right\} && \text{for} \quad t_p < r_o - r_i \\ &\xi = 1 && \text{for} \quad t_p \geq r_o - r_i \end{aligned} \tag{10.1}$$

Correspondingly, AVCOAT's material density (ρ), specific heat (C_p), and effective thermal conductivity (k_{eff}) are assumed to transition linearly with ξ from its virgin state ($\xi = 0$) to char form ($\xi = 1$) as shown in Fig 10.1b, i.e.

$$\begin{aligned} \rho &= \rho^v(1-\xi) + \rho^c\xi \\ C_p &= \left[C_p^v\left(1 - M_f^v\right) + C_p^f M_f^v\right](1-\xi) + \left[C_p^c\left(1 - M_f^c\right) + C_p^f M_f^c\right]\xi \\ k_{eff} &= k_{eff}^v(1-\xi) + k_{eff}^c\xi \end{aligned} \tag{10.2}$$

where the superscripts *v* and *c* are used to denote the properties of virgin AVCOAT and char, respectively, while the subscript/superscript *f* denotes the properties for the silica fibers. Since silica fibers remain chemically inert during the pyrolysis process, their mass does not change.[125] As such, the weight fraction of fibers in the char is given as $M_f^c = (\rho^v/\rho^c)M_f^v$. Note that the rule of mixtures used for calculating C_p in Eqn 10.2 includes the heat absorbed by the fibers, as well as that from the transition of the phenolic resin in the virgin AVCOAT to char as governed by the extent of pyrolysis index ξ. The specific heat capacities of phenolic resin in virgin AVCOAT ($C_p^v = 3281$ J/kgK) and char ($C_p^c = 1592$ J/kgK), and the silica fibers ($C_p^f = 730$ J/kgK), are assumed to be temperature-independent. While the thermal conductivity of monolithic phenolic resin, char (glassy carbon), and silica fibers can also be assumed to be temperature-independent ($k^r = 0.279$ W/mK, $k^c = 1.5$ W/mK, $k^f = 1.5$ W/mK)[126], the presence of micropores in the virgin AVCOAT and char allows for cavity radiation, viz. the radiative transfer of heat across the

void surfaces. The effective thermal conductivity of the porous material, resulting from this additional temperature-dependent radiative mode of heat transfer, can be obtained from Loeb's formulation as,[127]

$$k_{eff}^{v(c)} = k^m \left[1 - f_o^{v(c)} \left\{ \frac{1 - \frac{8\gamma\epsilon^{v(c)}\sigma r_0 T^3}{k^m}}{1 + \frac{8\gamma\epsilon^{v(c)}\sigma r_0 T^3}{k^m} \left(\frac{1 - f_0^{v(c)}}{f_0^{v(c)}} \right)} \right\} \right] \tag{10.3}$$

$$k^m = k^{r(c)} \left(1 - M_f^{v(c)} \right) + k^f M_f^{v(c)}$$

where σ is the Stephen's constant, $\epsilon^{v(c)}$ is the emissivity (estimated to be $\epsilon^v = 0.85$ for phenolic resin in virgin AVCOAT[98]; $\epsilon^c = 1.0$ for char), and γ is a geometric factor taken to be 2/3 for assumed spherical voids with average pore radius of 25 μm i.e. outer radius r_o of the individual microballoons.[92] The k_m term in Eqn 10.3 represents the conductivity of the solid phase which is adjusted to account for the relevant mass fraction of the silica fibers using rule of mixtures. Note that the contribution of cavity radiation in Eqn 10.3 largely depends on the temperature T and porosity f_0, with only minor contributions from the remaining parameters. Fig 10.2 shows the variation of effective thermal conductivity with temperature for pure phenolic resin ($\xi = 0$).

Following the approach of Kumar *et al.*[128] we solve a one-dimensional (1D) heat equation that incorporates the physical processes taking place in the reaction zone of the ablative material, viz. pyrolysis of the phenolic resin and the production of pyrolysis gases resulting in transpiration cooling, i.e.

$$\rho C_p \frac{\partial T}{\partial t} = \frac{\partial}{\partial y} \left(k_{eff} \frac{\partial T}{\partial y} \right) + Q_p(y) + Q_T(y) \tag{10.4}$$

where $y = 0$ represents the surface exposed to the heat flux $Q_{in} = -\, k_{eff} \left.\frac{dT}{dy}\right|_{y=0}$, and $y = L$ denotes the end of the 1D domain which is well-within the virgin AVCOAT for the time domain of interest where insulating boundary conditions can be assumed, i.e. $\left.\frac{dT}{dy}\right|_{y=L} = 0$ (Fig 10.1b). The initial temperature of the material is set at $T(y, 0) = 300\ K$. The body heat terms, Q_p and

Q_T, represent the rate of heat absorption per unit volume associated with pyrolysis and transpiration cooling, and are defined as,

$$Q_p(y) = h_p^r \dot{\rho}$$

$$Q_T(y) = -C_{pg} \frac{\partial T}{\partial y} \int_y^L \dot{\rho} \, \mathrm{d}y \tag{10.5}$$

where $C_{pg} = 2193$ J/kgK is the specific heat capacity of the pyrolysis gases reported in previous experiments.[98] In deriving the expression for Q_T, we assume thermal equilibrium is reached between pyrolysis gases and the material at each *y*. We solve Eqn 10.4 with finite difference, using an explicit forward-time-central-space (FTCS) scheme with a sufficiently small time step to ensure that the solution remains stable at each cross section. Parameters used in the development of this material response model are summarized in Table 10.1.

Table 10.1: List of parameters used in the material response model for AVCOAT.

Parameter	Symbol	Value	Source
Density of AVCOAT	ρ^v	0.51 g/cc	[98]
Density of char	ρ^c	0.32 g/cc	[98]
Density of phenolic resin	ρ^r	1.25 g/cc	*
Fiber matrix weight ratio in AVCOAT	M_f^v	0.25	[125]
Heat capacity of AVCOAT	C_p^v	3281 J/kgK	*
Heat capacity of char	C_p^c	1592 J/kgK	[89]
Heat capacity of fibers	C_p^f	730 J/kgK	[129]
Thermal conductivity of phenolic resin	k^r	0.279 W/mK	*
Thermal conductivity of glassy carbon	k^c	1.50 W/mK	[126]

Table 10.1 (cont.)

Thermal conductivity of fibers	k^f	$1.50\,\mathrm{W/mK}$	[129]
Heat of pyrolysis	h_p^r	1.58×10^6 J/kg	*
Heat capacity of pyrolysis gases	C_{pg}	2193 J/kgK	[98]
Porosity of AVCOAT	f_o^v	0.5	[98]
Porosity of char	f_o^c	0.8	[98]
Pore geometry factor for AVCOAT and char	γ	$2/3$	+
Outer radius of microballoons	r_o	25 μm	[92]
Emissivity of AVCOAT	ϵ^v	0.85	[98]
Emissivity of char	ϵ^c	1.0	+

* Obtained from MD simulations. + Estimated.

10.2 Validation of Material Response Model

To validate the model, we solve Eqn 10.4 for various input heat fluxes (Q_{in}) indicated in Table 10.2. Our model predictions of the char layer thicknesses at the indicated exposure times are in very good agreement with those reported from arc-jet measurements for AVCOAT, with an average deviation of ~13.7 %.[130] Recent experiments by Lisco *et al.* subjected a sample of AVCOAT material to a very high incident heat flux of $Q_{in} = 10{,}000\ \mathrm{kW/m^2}$ using an oxy-acetylene flame with oxygen: acetylene ratio of 3.375:1; four thermocouples were embedded within the AVCOAT sample at surface depths of 1.5 mm (TC1), 3.0 mm (TC2), 4.5 mm (TC3) and 6.0 mm (TC4).[131] As shown in Fig 10.3a, the temperature profile prediction for the last thermocouple TC4 from our 1D material response model (solid lines) is in good agreement with experimental measurements (dashed lines). However, our model over predicts the temperatures at the first three thermocouples; in fact, our model predictions for TC1 to TC3 appear to be

phase-shifted by a thermocouple spacing (1.5 mm). It should be noted that the MD-derived surface recession rates in our 1D model accounts only for thermally-induced pyrolysis of the phenolic resin and not the added effects of chemical reactions from O radicals, which are prevalent in an oxidizing environment produced by the oxy-acetylene flame. Lisco *et al*. demonstrated that in such environment and at this extremely high Q_{in}, the char progressively ablates from the surface and recesses at the rate of 0.32 mm/s. This additional mechanism of heat removal is not accounted for in our material response model which assumes a fully-intact char layer.

Our calculations in Fig 10.3 are based on the virgin AVCOAT density of $\rho^v = 0.51$ g/cc, and assumes microballoons with outer radius $r_o = 25$ μm, and silica fiber with mass fraction $M_f^v = 0.25$. We examine the sensitivity of each of these model parameters ($M_f^v; r_o; \rho^v$) in Fig 10.3b-d, by varying each parameter while keeping the remaining two fixed for a heat flux of $Q_{in} = 10{,}000$ kW/m^2 as in Fig 10.3a. Observe that increasing fiber mass fraction increases the temperature within the material (Fig 10.3b), while increasing density of AVCOAT while keeping the same fiber fraction delays the build-up of temperature (Fig 10.3d). The microballoon radius, however, has negligible effect on the temperature distribution within the material (Fig 10.3c).

Table 10.2: Comparison of the char layer thickness from model predictions versus experiments at the same input heat flux Q_{in} and exposure time.

Input heat flux Q_{in} (kW/m^2)	Exposure time (s)	Char layer thickness (mm)	
		Experiments[130]	Model predictions
2271	90	10.7	12.7
2839	80	10.2	12.2
3179	75	10.9	12.0
4031	38	8.9	8.3
5394	30	8.9	7.6
6189	30	8.9	7.8

In a separate experimental report, a sample of phenolic-refrasil, which is similar in structure to AVCOAT, was subjected to Q_{in} of 740 KW/m^2 for 1 min in a high speed wind

tunnel;[90] a thermocouple inserted 6.85 mm from the surface registered a peak temperature of 962 K during the test. Under the same Q_{in} conditions, our material response model predicts a peak temperature of 898 K at the thermocouple location.

10.3 Thermal Response of AVCOAT during Atmospheric Re-entry

Atmospheric re-entry subjects the AVCOAT surface to a time varying heat flux Q_{in}. We estimate the heat flux profile using the empirical formulation proposed by Finke for hypersonic laminar stagnation point heating.[132] The input flux is given as,

$$Q_{in} = \frac{5423}{\sqrt{R_{Orion}}}\sqrt{\frac{\rho_\infty}{\rho_{SL}}}\left(\frac{V_\infty}{3.05}\right)^{3.15} \; kW/m^2 \tag{10.6}$$

where, ρ_∞ and V_∞ are the free stream density and speed (km/sec), ρ_{SL} is the sea level density (ISA). $R_{Orion} = 2.52\ is$ the hemispherical nose radius of the Orion heatshield in meters.[91] The free stream conditions are obtained from the flight trajectory data for the Crew Exploration Vehicle (CEV) shown in Fig 10.4 a, b.[133]

The free stream conditions from flight trajectory data are used to estimate $Q_{in}(t)$, shown in Fig 10.5a. Peak heat flux of 595 kW/m^2 is reached at 200 s from the start of the trajectory. Fig 10.5b shows the material response model predictions of the through-thickness temperature profile versus trajectory time. During peak heating, temperatures exceeding 3000 K are predicted in the first 5 mm of the TPS. As shown by our MD simulations, such temperatures can cause surface spallation and micro-cracking of the phenolic resin. Bulk pyrolysis will be active ($\xi > 0$) up to depths of 25.95 mm, beyond which temperatures fall below the MD-calculated pyrolysis start temperature of 500 K. Fig 10.5c shows the evolving char layer ($\xi = 1$) thickness versus trajectory time. The char layer reaches a final thickness of 24.8 mm at the end of the 500 s trajectory, resulting in an average char formation rate of ~ 0.05 mm/s over the duration of re-entry. Charring is limited due to the combined effects of pyrolysis (Q_p) and transpiration cooling (Q_T) which confines heat transport to the surface region of the ablative TPS. We remark that the pyrolysis zone ($0 < \xi < 1$) remains relatively thin throughout the ablation process. It increases

in thickness monotonically reaching a final maximum thickness of 1.15 mm by the end of the trajectory. During the pyrolysis process, the virgin AVCOAT gets converted to char, which changes the density in the pyrolysis zone from ρ^v to ρ^c. This change in net density produces blowing gases which diffuse through the charring layer, and removes heat in the process (Q_T). Fig 10.5d shows the mass flow rate of pyrolysis gases emerging from the surface at y = 0,

$$\dot{m} = -\int_0^L \dot{\rho}\, dy \tag{10.7}$$

Observe that $\dot{m}$ has a non-monotonic profile, and has a peak value of 0.0154 $\mathrm{kg/m^2 s}$ at 23 s. Previous studies on steady state ablation coupled with a flow-field solver report a similar non-monotonous blowing rate profile with a peak value of 0.00692 $\mathrm{Kg/m^2 s}$.[134] From Fig 10.5d we observe that the blowing rate reaches its peak much earlier than 200 s, when peak heat flux is reached. The trend can be explained by observing that the char layer growth rate (Fig 10.5c) is decreasing with time, which indicates that the pyrolysis of deeper regions of AVCOAT becomes progressively more difficult despite the increasing heat flux. The transpiration gases play a key role in this phenomena as they remove more heat from the incipient char layers when generated deeper in the material. These blowing gases emerge from the surface and further aid in the performance of the heat shield as they push the heated shock layer from the heatshield.

10.4 Summary

In this chapter, results from MD simulations were used to inform a thermal material response model at the macroscale governed by a 1D heat transfer equation. The macroscopic model considers (a) the complex structure of porous polymer ablators such as AVCOAT, (b) the phase transition from virgin material to char, (c) the various heat removal processes, specifically, pyrolysis and transpiration cooling, (d) thermal conductivity variation due to cavity radiation and (e) Contribution from the silica fibers. Predictions from the model were validated against prior arc-jet and oxy-acetylene torch experiments on AVCOAT TPS. Finally, the heat flux encountered by the TPS during flight was estimated and the material response model was used to

predict the temperatures at various cross sections inside the material, the thickness of the resulting char layer and the blowing rate of pyrolysis gases under re-entry conditions. The unified atomic to continuum approach presented here ties across multiple length and time scales, providing an important tool for accurately predicting the flight performance using computer simulations.

10.5 Figures

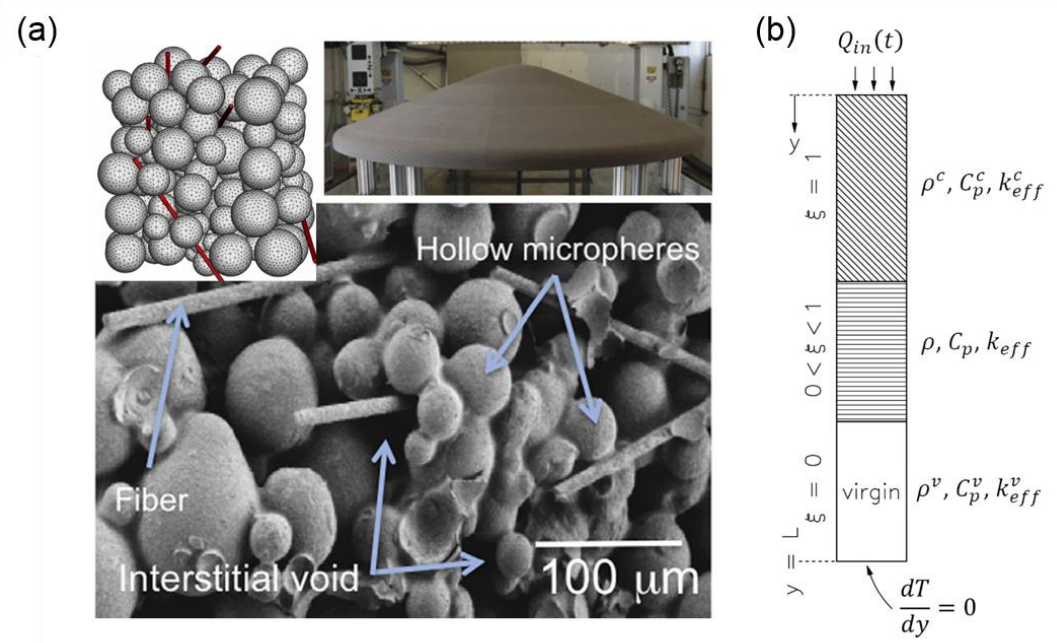

Fig 10.1: AVCOAT TPS comprising of a mixture of silica fibers and phenolic microballoons. Clockwise from bottom: Scanning electron microscopy image of AVCOAT microstructure; [93] computer aided representation of the model structure; picture of AVCOAT heat shield. (b) One-dimensional material response model, accounting for virgin-char transitions, heat conduction, pyrolysis gas generation, and transpiration cooling.

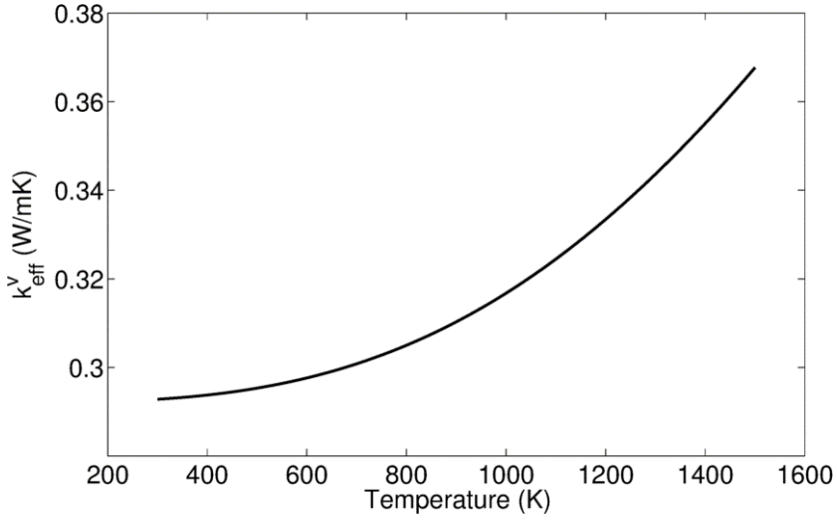

Fig 10.2: Effective thermal conductivity of virgin AVCOAT as calculated from Eqn 10.3. The thermal conductivity increases with temperature due to increasing contribution from cavity radiation, within the porous bulk.

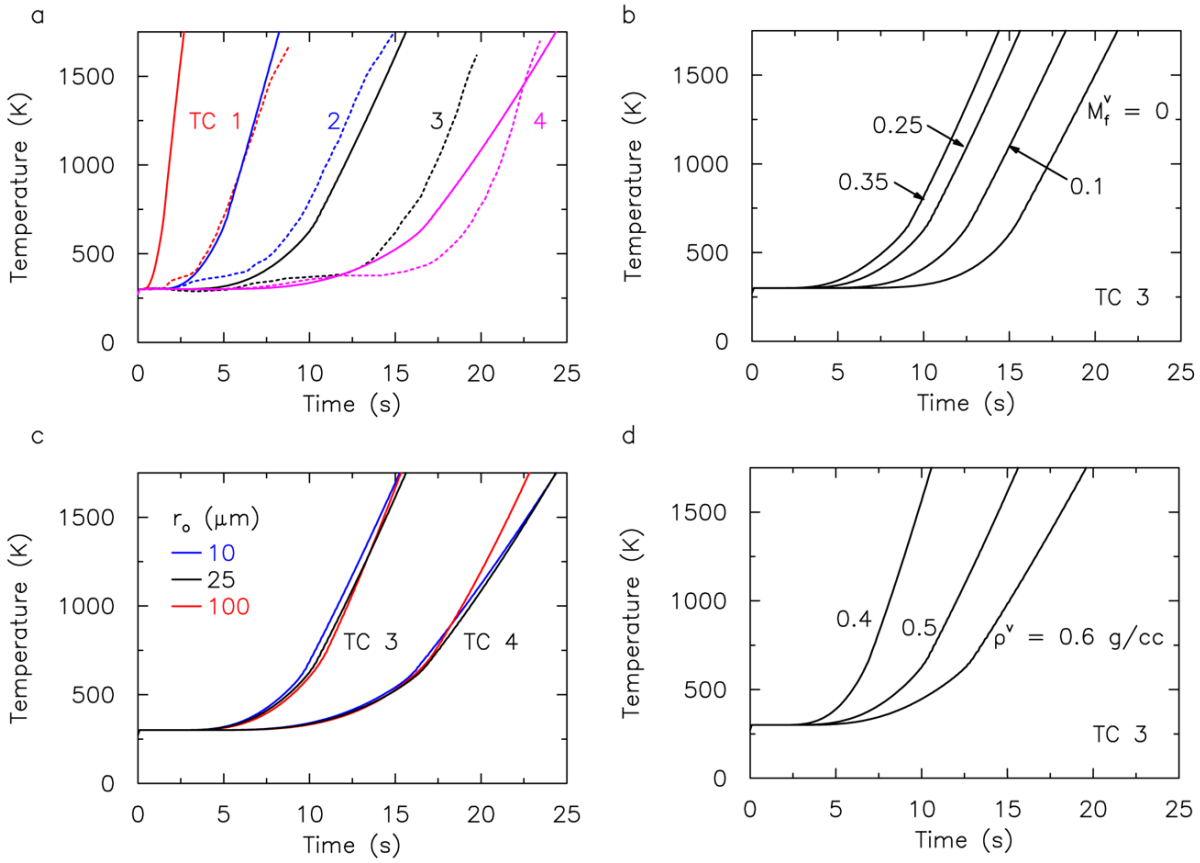

Fig 10.3: Temperature profiles at various depths for AVCOAT sample subjected to an incident heat flux of Q_{in} = 10,000 kW/m^2. Thermocouples (TC) 1-4 are embedded at increasing depths of 1.5, 3.0, 4.5, and 6 mm from the surface. (a) Comparison of model predictions (solid lines) versus experimental measurements (dashed lines)[132]. (b) Temperature profiles at TC3 for varying silica fiber mass fraction M_f^v. (c) Temperature profiles at TC3 and TC4 for varying microballoon outer radius r_o. (d) Temperature profiles at TC3 for varying virgin AVCOAT density ρ^v.

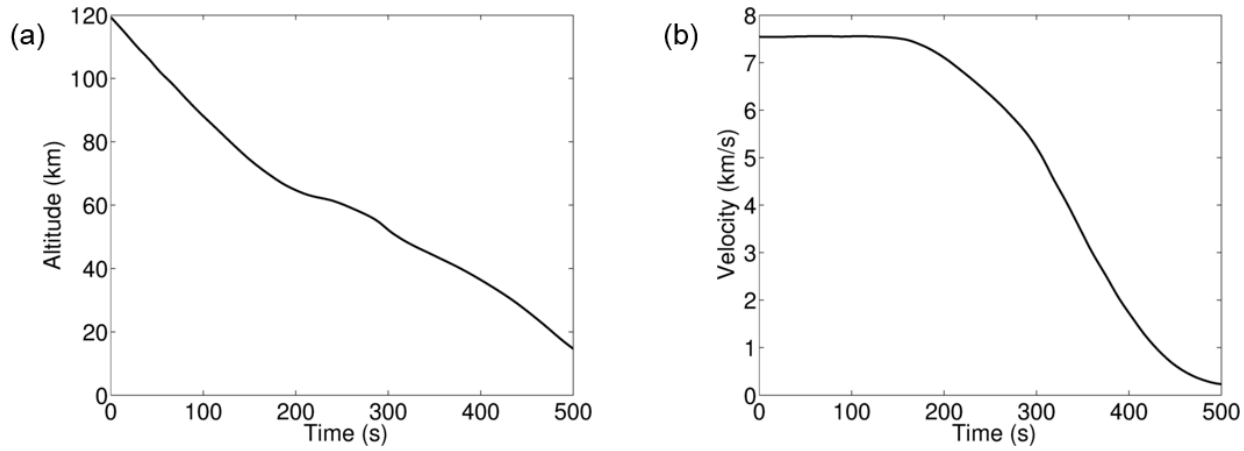

Fig 10.4: (a) Altitude and (b) velocity during atmospheric re-entry of the Crew Exploration Vehicle (CEV) from low earth orbit.[134]

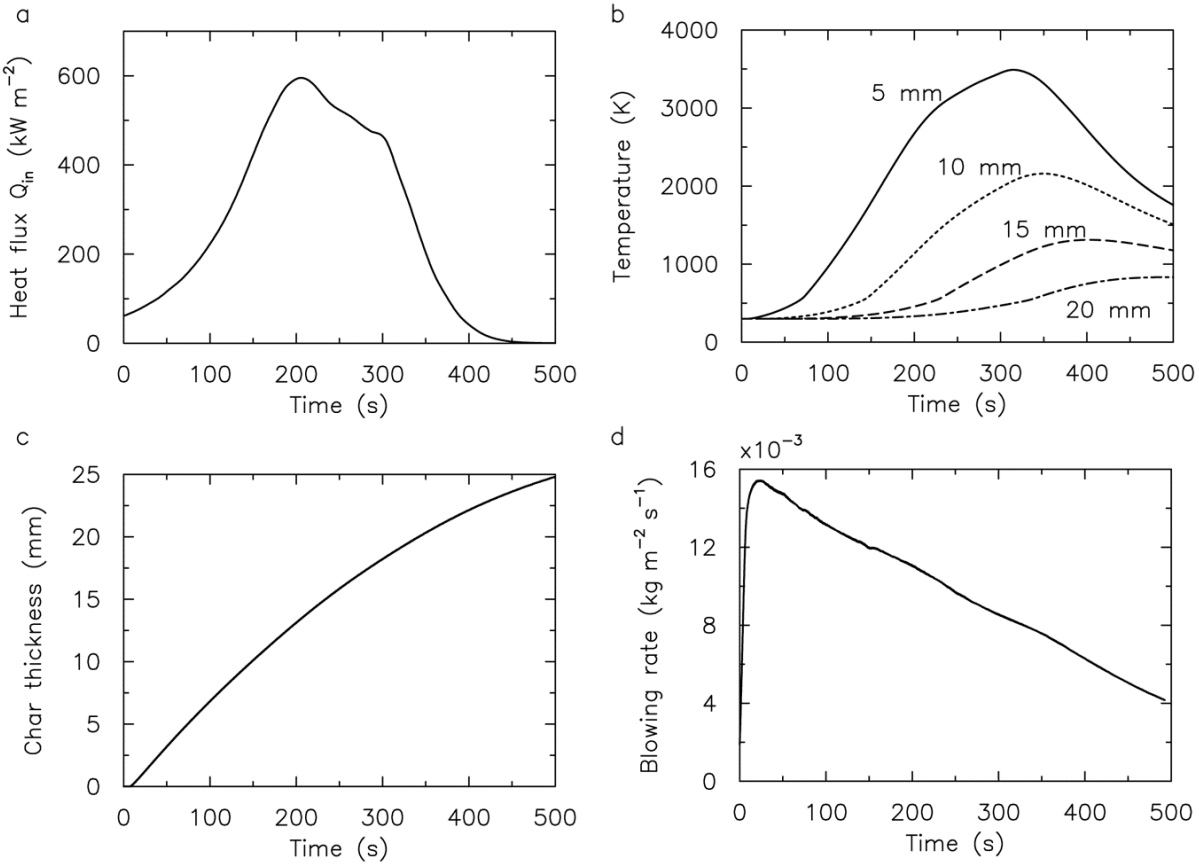

Fig 10.5: (a) Time-varying heat flux profile (Q_{in}) experienced by an AVCOAT TPS during atmospheric reentry of a Crew Exploration Vehicle from low earth orbit. (b-d) Predictions of the material response model: Time evolution of temperature at various surface depths (b), evolving thickness of the char layer (c), and blowing rate of pyrolysis gases from the surface (d).

Chapter 11. Future Work: Ablative TPS

11.1 Modeling of Polymeric Char

Our MD simulation so far demonstrate the thermal degradation of phenolic resin into pyrolysis gases. In reality however, the phenolic resin or any polymeric precursor generates carbonaceous char residue upon expose to high temperatures. The process of transition of polymer into char is called carbonization and is beyond the length- and time-scale of atomic scale simulations.[135] Due to the amorphous nature of the materials involved, most time acceleration techniques mentioned in chapter 6 are not applicable to study the pyrolysis of phenolic resin. Hence, the char produced during pyrolysis should be modeled and examined in using a separate set of MD simulations. The analysis of the role of char represents a potential avenue for future work in this field.

During pyrolysis phenolic resin produces non-graphitizing char, composed largely of sp^2 and sp^3 C atoms arranged in an amorphous manner. In its solid state, this material is called glassy carbon and exists in a highly porous form.[136] In chapter 10 we considered the role of incident heat flux in the material response model and ignored the contribution of thermal O and N radicals. While these species are prevented from interacting with the virgin phenolic resin due to the blowing of the pyrolysis gases, they do react with the char. However, to date, the nature of the gas surface chemistry close to the heat shield surface has not been fully investigated. Here, we present an algorithm for modeling the atomic structure of glassy carbon using MD simulations. The algorithm can be used for developing a recession model for the char layer based on surface oxidation and nitration rates established from MD simulations.

At a molecular scale, glassy carbons have a highly crosslinked amorphous carbon network. An important chemical signature distinguishing glassy carbons from other forms of carbon, like diamond-like carbon (DLC), graphite and diamond, is the fraction of sp^3 hybridized C atoms. X-ray diffraction experiments have estimated this value to be 6-8 % for glassy carbon, in contrast to 0 % for graphite, 65-70 % for DLC and 100 % for diamond.[137] The density of a monolithic solid composed of glassy carbon has been reported to be ~ 2.24 g/cc.[135] While this makes glassy carbon denser that phenolic resin the presence of extensive micro pores formed during heat treatment reduces the density to ~ 0.5g/cc in its char form.[98]

We present an '*atom deposition*' method for modeling the molecular structure of glassy carbon using MD simulations.[138] This method is contrast with the '*pyrolytic*' approach by Lawson *et al.*[139] and the *Reverse Monte Carlo* (RMC) approach by Jain *et al.*[140] Unlike the pyrolytic approach the atom deposition method does not begin with a precursor polymer and is less computational expensive. RMC uses an externally imposed parameter like the structure factor and evolves the molecular configuration to minimize the difference between the simulation and the target parameters. As a results, RMC can produces non-physical molecular configuration with high local energy densities. For generating the model carbon structures we use the LAMMPS package. The interactions between the C atoms is governed by the Airebo potential.[141] The liquid quench process can be divided into three stages: mixing stage, compression stage and equilibration stage. A fully periodic $5.0 \times 5.0 \times 5.0$ nm^3 simulation box is populated with 7654 C atoms generated at randomly chosen coordinates, resulting in an overall density of 1.12 g/cc. The system first is subjected to an energy minimization using the conjugate gradient method. The mixing is initiated by heating the system to a temperature of 1000 K, which is gradually quenched to a 100 K, linearly over 500 ps.

We calculate the average C-C coordination number as a measure of the degree of condensation. During the mixing stage the coordination number increases from 1.70 to 2.49. To increase the density of the simulation box to the char target density of 2.24 g/cc the system is subjected to the compression stage. The volume of the simulation box is halved by deforming the dimensions uniformly over a simulation time of 1000 ps. During the compression the C atoms are set to a temperature of 2000 K using a Berendsen thermostat to mitigate local residual stresses. The average C-C coordination number further increases from 2.49 to 3.05 which indicates that a large number of additional C-C bonds are formed. The final equilibration stage involves subjecting the system to an NPT ensemble with the pressure and temperature set to 10 atm and 300 K respectively, for 500 ps. The density of the system converge to $\sim$ 2.18 g/cc at the end of equilibration stage.

Fig 11.1 shows the final relaxed molecular configuration obtained by the liquid quench method along with the electron micrographs of carbonized phenolic resin at 900 K.[142] Note that the amorphous nature of the structure visible in the micrographs is similar to the MD-derived structure. Since our eventual goal is the study the oxidation and nitration reactions of the char we

switch the interatomic potential from Airebo to ReaxFF. We use the ReaxFF potential by Strachen *et al.*, which was calibrated for the high temperature decomposition of nitramine RDX and can simulate C, H, O and N species.[143] The ReaxFF potential reported by Chenoweth *et al.* was shown to predict unphysically low thermal stability for glassy carbon.[117] The system generated by liquid quench method is subjected to energy minimization and thermal equilibration at 300 K using the ReaxFF potential. We determine the fraction of sp^3 hybridized C atoms in the final molecular structure to be 6.98 %, in excellent agreement with experimental reported value of 6-8 %.[137] We calculate the radial density function of the C atoms and found the curve to be in good agreement with previous MD and RMC simulations. The first and second peaks (for sp^2 and sp^3 C atoms) are located at 1.395 Å and 2.415 Å, respectively, in agreement with previous simulations.[138,139,144,145] Simulation of the pyrolysis of the phenolic resin char (Fig 11.1) under thermal and reactive conditions presents an avenue for future work in this field.

11.2 DSMC and RWMC Techniques

The material response model we developed in chapter 10 used a 1D heat transfer equation (Eqn 10.4) as its governing relationship. Such a form only considered the conductive heat transfer and used the Loeb's equation and transpiration cooling term to approximate the radiation and convection modes respectively. Transpiration cooling is the heat removed by the flow of pyrolysis gases generated in the relatively cooler interior regions of the TPS as they blow towards the hotter surface. The transpiration cooling term $Q_T(y)$ described in Eqn 10.5 is derived assuming the gas flow is sufficiently slow to reach thermal equilibrium at each cross section. In other words, at each time step the gases reach the temperature of the cross section, removing heat as it moves towards the increasing hotter regions closer to the surface. A more accurate and representation approach for approximating the transpiration cooling is using Direct Simulations Monte Carlo (DSMC)[146,147]. DSMC is a numerical methods for modeling rarefied gas flow where the mean free path of a molecule is of similar order of magnitude as the representative length scale of the physical domain through which the gas is flowing. Since the TPS encounters extremely low density gases in the upper atmosphere which are heated to high temperatures in the plasma layer, the rarefied assumption is a more accurate representation of the flow than

conventional CFD. Fig 11.2a shows the streamlines of the pyrolysis gases flowing though the phenolic microballoons which constitute the AVCOAT TPS. DSMC simulations coupled with solid heat transfer models can also be used to improve the estimate of the incident heat flux Q_{in} which is used as a boundary condition in Eqn 10.4. In the current work the stagnation heat flux estimate by Finke is used as described in Eqn 10.6.[132] Fig 11.2b shows the incident heat flux profile on the TPS surface. The DSMC calculations are significantly more accurate that the current form used in Eqn 10.6 and have a better resolution which can enable 1D heat transfer model to be further extended into a 3D formulation.[148–150] A complete 3D formulation would allow for the estimation of the spatial profile of the temperature and char thickness on the surface of the TPS.

Another serious limitation of the material response model presented here is the approximate treatment of cavity radiation. We utilized Loeb's homogenized conduction-radiation coupling in Eqn 10.3 which assumed the matrix to be an isotropic, homogeneous material containing uniformly dispersed spherical voids of equal diameter.[127] The actual microstructure is far more complex.[92] Cavity radiation is likely to be present within the phenolic microballoons (reinforced voids) as well as in the space between the microballoons (interstitial voids). While the reinforced voids can be approximated as perfect sphered the interstitial voids are certainly not spherical in shape. Additionally, the microballons have a range of diameters and wall thickness, and cannot be approximated as equal sized voids. Further complicating the model is role of the novolac epoxy glue which the binds the constituents together. In our calculations we have assumed that the glue has the same properties as the phenolic resin and is assumed to part of the microballons. Random walk Monte Carlo (RWMC) methods provide a possible means to circumvent the inaccuracy of the Loeb's assumption.[151,152] The irregularity of the internal geometry of the TPS makes conventional finite element methods infeasible due to challenges of meshing. RWMC is a mesh-free technique which is well suited for the microstructure of the TPS. The methods involves tracking the local density of virtual heat carrying units called *Walkers*. During each time step the position of the walkers is updated by sampling a normally distributed random variable. Inside the void the walkers travel in a straight line till it intersect with an internal surface. The method has been successfully applied for calculation of the effective thermal conductivity of porous collection fibers and is currently being investigated as a replacement for the Loeb's formulation (Eqn 10.3) in the material response model.[150,153]

11.3 Figures

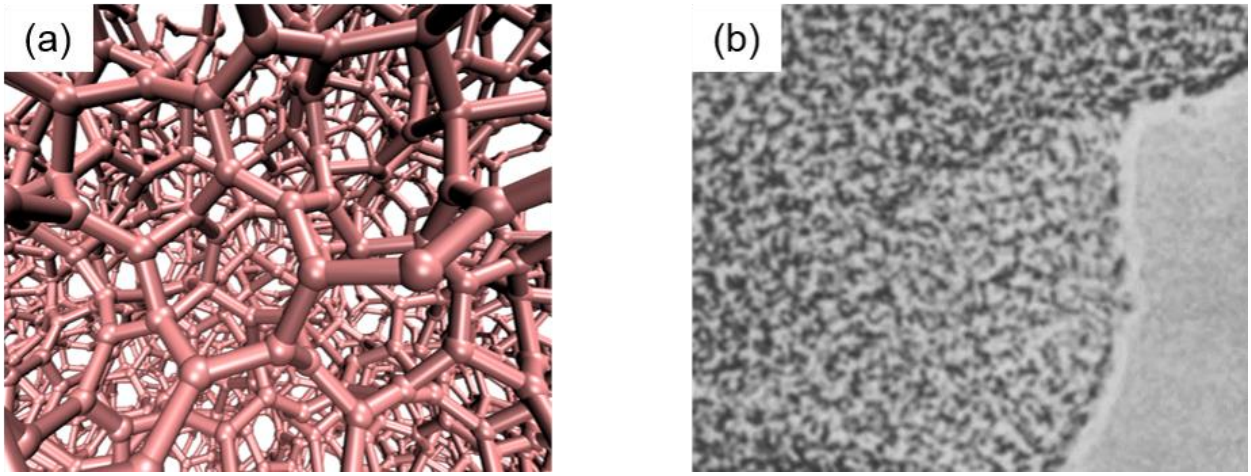

Fig 11.1: (a) Molecular structure of glassy carbon generated by the liquid quench method. (b) Electron micrographs of carbonized phenolic resin at 900 K.[143]

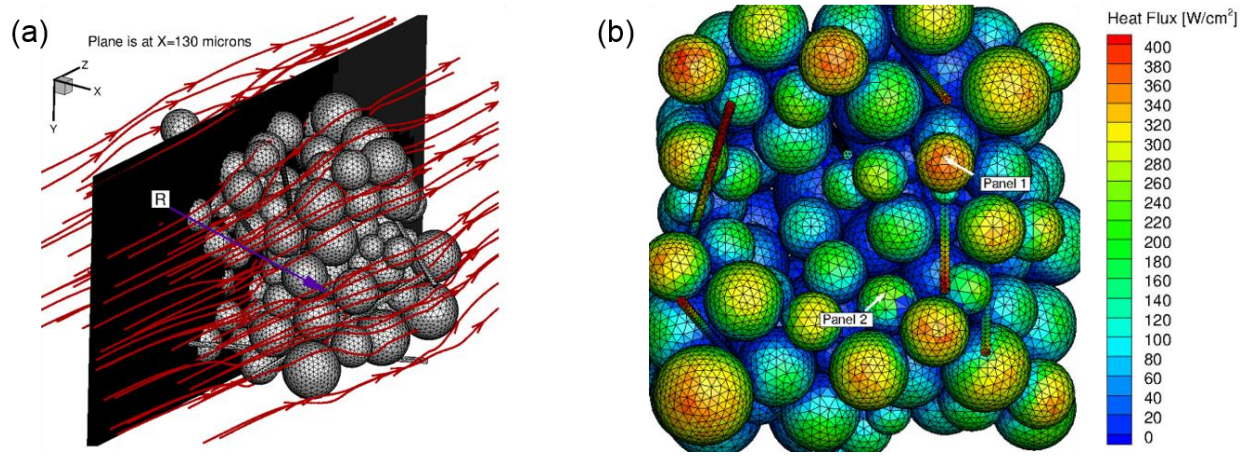

Fig 11.2: (a) Flow stream lines through the AVCOAT TPS calculated using DSMC. (b) Heat flux incident on the surface of the TPS as calculated from DSMC.[148]

Chapter 12. Conclusions

In this dissertation, atomistic simulations coupled to micromechanics models were used to study the patterning of graphene (Part I) and the ablation of thermal protection systems (Part II) resulting from controlled and erosive plasma-surface interactions. In Part I (chapter 2-6) we study the controlled patterning of graphene by low energy hydrogen plasma using scale bridging molecular dynamics. Our simulations of monolayer graphane etching uncover distinct etching mechanisms, operative within narrow ion energy windows, which fully explain the differing plasma-graphene reactions observed experimentally. Specific ion energy ranges are demonstrated for stable isotropic (∼2 eV) versus anisotropic hole growth (∼20–30 eV) within the basal plane of graphene, as well as for pure edge etching of graphene (∼1 eV). For etching of multilayer graphene we demonstrate the possibility of controlled 3D patterning using hydrogen plasma tuned to specific ion energy windows. Layers 1 to 4 in a multilayer sheet were show to etching selectively at ion energy range centered on 10 eV, 17 eV, 23 eV and 28 eV respectively. For both monolayer and multilayer graphene we developed scale bridging continuum level models to enable a direct comparison of experiments with simulations. Finally, we examined the effects of thermal processes beyond the time-scale of MD simulations, such as thermal dehydrogenation and surface H recombination. The chemical kinetics of dehydrogenation were obtained using high temperature MD simulations.

In Part II (chapter 7-11) we focus on the erosive effect of atmospheric plasma on the thermal protection systems of re-entry space crafts. Large-scale MD simulations coupled to mechanism-based macroscale models were used to quantify the complex pyrolysis kinetics operative in polymer-based charring ablators. Our MD simulations showed that pyrolysis of highly-crosslinked phenolic resin was activated at temperatures greater than 500 K. Early-stage pyrolysis was dominated by the removal of –OH functional groups and –H atoms from aromatic C rings to release H_2O, while later stage involved the breaking up of these weakened C-rings to release C-based fragments (CH_4, C_2H_2, etc.). The thermal decomposition reactions were found to scale with temperature following the Arrhenius law, with activation energy of $E_a = 42.5$ kcal/mol and pre-exponential factor of $B = 5.24 \times 10^{12}\ s^{-1}$ .These kinetic parameters were used to derive an expression for surface recession rate of monolithic phenolic resin as a function of temperature. Results from MD simulations were used to inform a thermal material response

model at the macroscale governed by a 1D heat transfer equation. The macroscopic model considers (a) the complex structure of porous polymer ablators such as AVCOAT, (b) the phase transition from virgin material to char, (c) the various heat removal processes, specifically, pyrolysis and transpiration cooling, and (d) thermal conductivity variation due to cavity radiation. Predictions from the model were validated against prior arc-jet and oxy-acetylene torch experiments on AVCOAT TPS. The model was also used to gain insights into the thermal response of AVCOAT TPS during atmospheric reentry from low-earth orbit.

References

(1) Council, N. R. *Plasma Processing of Materials*; National Academies Press: Washington, D.C., 1991.

(2) Donnelly, V. M.; Kornblit, A. Plasma Etching: Yesterday, Today, and Tomorrow. *J. Vac. Sci. Technol. A Vacuum, Surfaces, Film.* **2013**, *31* (5), 50825.

(3) Reyntjens, S.; Puers, R. A Review of Focused Ion Beam Applications in Microsystem Technology. *J. Micromechanics Microengineering* **2001**, *11* (4), 287–300.

(4) Bell, D. C.; Lemme, M. C.; Stern, L. A.; Williams, J. R.; Marcus, C. M. Precision Cutting and Patterning of Graphene with Helium Ions. *Nanotechnology* **2009**, *20* (45), 455301.

(5) Bolt, H.; Barabash, V.; Krauss, W.; Linke, J.; Neu, R.; Suzuki, S.; Yoshida, N.; ASDEX Upgrade Team. Materials for the Plasma-Facing Components of Fusion Reactors. *J. Nucl. Mater.* **2004**, *329–333*, 66–73.

(6) Löhle, S.; Hermann, T.; Zander, F. Experimental Assessment of the Performance of Ablative Heat Shield Materials from Plasma Wind Tunnel Testing. *CEAS Sp. J.* **2017**, 1–9.

(7) Allen, J. E. The Plasma–sheath Boundary: Its History and Langmuir's Definition of the Sheath Edge. *Plasma Sources Sci. Technol.* **2008**, *18* (1), 14004.

(8) Huber; W., P. *Deduction of Reentry Plasma Properties about Manned Orbital Spacecraft from Radio Signal Attenuation Data*; 1967.

(9) Rybak, J. *Causes, Effects and Diagnostic Measurements of the Reentry Plasma Sheath*; Colorado State University, 1970.

(10) Wright, M. J.; Milos, F. S.; Tran, P. Afterbody Aeroheating Flight Data for Planetary Probe Thermal Protection System Design. *J. Spacecr. Rockets* **2006**, *43* (5), 929–943.

(11) Ponomarenko, L. A.; Schedin, F.; Katsnelson, M. I.; Yang, R.; Hill, E. W.; Novoselov, K. S.; Geim, A. K. Chaotic Dirac Billiard in Graphene Quantum Dots. *Science* **2008**, *320* (5874), 356–358.

(12) Geim, A. K.; Novoselov, K. S. The Rise of Graphene. *Nat. Mater.* **2007**, *6* (3), 183–191.

(13) Bonaccorso, F.; Sun, Z.; Hasan, T.; Ferrari, A. C. Graphene Photonics and Optoelectronics. *Nat. Photonics* **2010**, *4* (9), 611–622.

(14) Dvorak, M.; Oswald, W.; Wu, Z. Bandgap Opening by Patterning Graphene. *Sci. Rep.* **2013**, *3* (2289).

(15) Son, Y.-W.; Cohen, M. L.; Louie, S. G. Energy Gaps in Graphene Nanoribbons. *Phys. Rev. Lett.* **2006**, *97* (21).

(16) Son, Y.-W.; Cohen, M. L.; Louie, S. G. Half-Metallic Graphene Nanoribbons. *Nature* **2006**, *444* (7117), 347–349.

(17) Surwade, S. P.; Smirnov, S. N.; Vlassiouk, I. V; Unocic, R. R.; Veith, G. M.; Dai, S.;

Mahurin, S. M. Water Desalination Using Nanoporous Single-Layer Graphene. *Nat. Nanotechnol.* **2015**, *10* (5), 459–464.

(18) Cohen-Tanugi, D.; Grossman, J. C. Water Desalination across Nanoporous Graphene. *Nano Lett.* **2012**, *12* (7), 3602–3608.

(19) Hauser, A. W.; Schwerdtfeger, P. Methane-Selective Nanoporous Graphene Membranes for Gas Purification. *Phys. Chem. Chem. Phys.* **2012**, *14* (38), 13292–13298.

(20) Koenig, S. P.; Wang, L.; Pellegrino, J.; Bunch, J. S. Selective Molecular Sieving through Porous Graphene. *Nat. Nanotechnol.* **2012**, *7* (11), 728–732.

(21) Postma, H. W. C. Rapid Sequencing of Individual DNA Molecules in Graphene Nanogaps. *Nano Lett.* **2010**, *10* (2), 420–425.

(22) El-Kady, M. F.; Kaner, R. B. Scalable Fabrication of High-Power Graphene Micro-Supercapacitors for Flexible and on-Chip Energy Storage. *Nat. Commun.* **2013**, *4*.

(23) Robinson, J. T.; Burgess, J. S.; Junkermeier, C. E.; Badescu, S. C.; Reinecke, T. L.; Perkins, F. K.; Zalalutdniov, M. K.; Baldwin, J. W.; Culbertson, J. C.; Sheehan, P. E.; Snow, E. S. Properties of Fluorinated Graphene Films. *Nano Lett.* **2010**, *10* (8), 3001–3005.

(24) Fan, X.; Shen, Z.; Liu, a. Q.; Kuo, J.-L. Band Gap Opening of Graphene by Doping Small Boron Nitride Domains. *Nanoscale* **2012**, *4* (6), 2157.

(25) Tapasztó, L.; Dobrik, G.; Nemes-Incze, P.; Vertesy, G.; Lambin, P.; Biró, L. Tuning the Electronic Structure of Graphene by Ion Irradiation. *Phys. Rev. B* **2008**, *78* (1), 2–5.

(26) Fischbein, M. D.; Drndic, M. Electron Beam Nanosculpting of Suspended Graphene Sheets. *Appl. Phys. Lett.* **2008**, *93* (11).

(27) Diankov, G.; Neumann, M.; Goldhaber-Gordon, D. Extreme Mono Layer-Selectivity of Hydrogen-Plasma Reactions with Graphene. *ACS Nano* **2013**, *7* (2), 1324–1332.

(28) Yang, R.; Zhang, L.; Wang, Y.; Shi, Z.; Shi, D.; Gao, H.; Wang, E.; Zhang, G. An Anisotropic Etching Effect in the Graphene Basal Plane. *Adv. Mater.* **2010**, *22* (36), 4014–4019.

(29) Xie, L.; Jiao, L.; Dai, H. Selective Etching of Graphene Edges by Hydrogen Plasma. *J. Am. Chem. Soc.* **2010**, *132* (42), 14751–14753.

(30) Skoro, N.; Puac, N.; Lazovic, S.; Cvelbar, U.; Kokkoris, G.; Gogolides, E. Characterization and Global Modelling of Low-Pressure Hydrogen-Based RF Plasmas Suitable for Surface Cleaning Processes. *J. Phys. D-Applied Phys.* **2013**, *46* (47).

(31) Despiau-Pujo, E.; Davydova, A.; Cunge, G.; Delfour, L.; Magaud, L.; Graves, D. B. Elementary Processes of H2 Plasma-Graphene Interaction: A Combined Molecular Dynamics and Density Functional Theory Study. *J. Appl. Phys.* **2013**, *113* (11).

(32) Felten, A.; McManus, D.; Rice, C.; Nittler, L.; Pireaux, J. J.; Casiraghi, C. Insight into Hydrogenation of Graphene: Effect of Hydrogen Plasma Chemistry. *Appl. Phys. Lett.* **2014**, *105* (18).

(33) Cazalilla, M. A.; Lorente, N.; Muino, R. D.; Gauyacq, J. P.; Teillet-Billy, D.; Echenique, P. M. Theory of Auger Neutralization and Deexcitation of Slow Ions at Metal Surfaces. *Phys. Rev. B* **1998**, *58* (20), 13991–14006.

(34) Datz, S.; Sundstrom, G.; Biedermann, C.; Brostrom, L.; Danared, H.; Mannervik, S.; Mowat, J. R.; Larsson, M. Branching-Processes in the Dissociative Recombination of H_3^+. *Phys. Rev. Lett.* **1995**, *74* (6), 896–899.

(35) Marinov, D. Comment on "Insight into Hydrogenation of Graphene: Effect of Hydrogen Plasma Chemistry" [Appl. Phys. Lett. **105** , 183104 (2014)]. *Appl. Phys. Lett.* **2016**, *108* (22), 226101.

(36) Davydova, A.; Despiau-Pujo, E.; Cunge, G.; Graves, D. B. Etching Mechanisms of Graphene Nanoribbons in Downstream H_2 Plasmas: Insights from Molecular Dynamics Simulations. *J. Phys. D-Applied Phys.* **2015**, *48* (19).

(37) Plimpton, S. Fast Parallel Algorithms For Short-Range Molecular-Dynamics. *J. Comput. Phys.* **1995**, *117* (1), 1–19.

(38) Newsome, D. A.; Sengupta, D.; Foroutan, H.; Russo, M. F.; van Duin, A. C. T. Oxidation of Silicon Carbide by O_2 and H_2O: A ReaxFF Reactive Molecular Dynamics Study, Part I. *J. Phys. Chem. C* **2012**, *116* (30), 16111–16121.

(39) van Duin, A. C. T.; Dasgupta, S.; Lorant, F.; Goddard, W. A. ReaxFF: A Reactive Force Field for Hydrocarbons. *J. Phys. Chem. A* **2001**, *105* (41), 9396–9409.

(40) Boukhvalov, D. W.; Katsnelson, M. I.; Lichtenstein, A. I.; Hydrogen on Graphene: Electronic Structure, Total Energy, Structural Distortions and Magnetism from First-Principles Calculations. *Phys. Rev. B - Condens. Matter Mater. Phys.* **2008**, *77* (3), 1–7.

(41) Ivanovskaya, V. V.; Zobelli, A.; Teillet-Billy, D.; Rougeau, N.; Sidis, V.; Briddon, P. R. Hydrogen Adsorption on Graphene: A First Principles Study. *Eur. Phys. J. B* **2010**, *76* (3), 481–486.

(42) Sluiter, M. H. F.; Kawazoe, Y. Cluster Expansion Method for Adsorption: Application to Hydrogen Chemisorption on Graphene. *Phys. Rev. B* **2003**, *68* (8), 85410.

(43) Miao, M.; Nardelli, M. B.; Wang, Q.; Liu, Y. First Principles Study of the Permeability of Graphene to Hydrogen Atoms. *Phys. Chem. Chem. Phys.* **2013**, *15* (38), 16132.

(44) Nordlund, K. Molecular Dynamics Simulation of Ion Ranges in the 1–100 keV Energy Range. *Comput. Mater. Sci.* **1995**, *3* (4), 448–456.

(45) Cuong, N. T.; Otani, M.; Okada, S. Semiconducting Electronic Property of Graphene Adsorbed on (0001) Surfaces of SiO_2. *Phys. Rev. Lett.* **2011**, *106* (10).

(46) Stukowski, A. Structure Identification Methods for Atomistic Simulations of Crystalline Materials. *Model. Simul. Mater. Sci. Eng.* **2012**, *20* (4), 45021.

(47) Tsuzuki, H.; Branicio, P. S.; Rino, J. P. Structural Characterization of Deformed Crystals by Analysis of Common Atomic Neighborhood. *Comput. Phys. Commun.* **2007**, *177* (6), 518–523.

(48) Faken, D.; Jónsson, H. Systematic Analysis of Local Atomic Structure Combined with 3D Computer Graphics. *Comput. Mater. Sci.* **1994**, *2* (2), 279–286.

(49) Fukunaga, T.; Itoh, K.; Otomo, T.; Mori, K.; Sugiyama, M.; Kato, H.; Hasegawa, M.; Hirata, A.; Hirotsu, Y.; Hannon, A. C. Voronoi Analysis of the Structure of Cu–Zr and Ni–Zr Metallic Glasses. *Intermetallics* **2006**, *14* (8–9), 893–897.

(50) Mauri, F.; Pasquarello, A.; Pfrommer, B. G.; Yoon, Y.-G.; Louie, S. G. Si-O-Si Bond-Angle Distribution in Vitreous Silica from First-Principles ^{29}Si NMR Analysis. *Phys. Rev. B* **2000**, *62* (8), R4786–R4789.

(51) Keys, A. S.; Iacovella, C. R.; Glotzer, S. C. Characterizing Complex Particle Morphologies through Shape Matching: Descriptors, Applications, and Algorithms. *J. Comput. Phys.* **2011**, *230* (17), 6438–6463.

(52) Hu, S.; Lozada-Hidalgo, M.; Wang, F. C.; Mishchenko, A; Schedin, F.; Nair, R. R.; Hill, E. W.; Boukhvalov, D. W.; Katsnelson, M. I.; Dryfe, R. A. W.; Grigorieva, I. V; Wu, H. A; Geim, A K. Proton Transport through One-Atom-Thick Crystals. *Nature* **2014**, *516* (7530), 227–230.

(53) Liu, Y.; Dobrinsky, A.; Yakobson, B. I. Graphene Edge from Armchair to Zigzag: The Origins of Nanotube Chirality? *Phys. Rev. Lett.* **2010**, *105* (23).

(54) Okada, S. Energetics of Nanoscale Graphene Ribbons: Edge Geometries and Electronic Structures. *Phys. Rev. B* **2008**, *77* (4).

(55) Jiang, D.; Sumpter, B. G.; Dai, S. Unique Chemical Reactivity of a Graphene Nanoribbon's Zigzag Edge. *J. Chem. Phys.* **2007**, *126* (13).

(56) Russo, C. J.; Golovchenko, J. A. Atom-by-Atom Nucleation and Growth of Graphene Nanopores. *Proc. Natl. Acad. Sci. U. S. A.* **2012**, *109* (16), 5953–5957.

(57) Weldon, M. K.; Collot, M.; Chabal, Y. J.; Venezia, V. C.; Agarwal, A.; Haynes, T. E.; Eaglesham, D. J.; Christman, S. B.; Chaban, E. E. Mechanism of Silicon Exfoliation Induced by Hydrogen/helium Co-Implantation. *Appl. Phys. Lett.* **1998**, *73* (25), 3721.

(58) Bongiorno, A.; Colombo, L.; Cargnoni, F. Hydrogen Diffusion in Crystalline SiO_2. *Chem. Phys. Lett.* **1997**, *264* (3–4), 435–440.

(59) Lee, R. W. Diffusion Of Hydrogen In Natural And Synthetic Fused Quartz. *J. Chem. Phys.* **1963**, *38* (2), 448.

(60) Eren, B.; Hug, D.; Marot, L.; Pawlak, R.; Kisiel, M.; Steiner, R.; Zumbuhl, D. M.; Meyer, E. Pure Hydrogen Low-Temperature Plasma Exposure of HOPG and Graphene: Graphane Formation? *Beilstein J. Nanotechnol.* **2012**, *3* (1), 852–859.

(61) Rosner, D. E. High-Temperature Gas-Solid Reactions. *Annu. Rev. Mater. Sci.* **1972**, *2* (1), 573–606.

(62) Luo, Z.; Yu, T.; Kim, K. J.; Ni, Z.; You, Y.; Lim, S.; Shen, Z.; Wang, S.; Lin, J. Thickness-Dependent Reversible Hydrogenation of Graphene Layers. *ACS Nano* **2009**, *3* (7), 1781–1788.

(63) Shi, Z.; Yang, R.; Zhang, L.; Wang, Y.; Liu, D.; Shi, D.; Wang, E.; Zhang, G. Patterning Graphene with Zigzag Edges by Self-Aligned Anisotropic Etching. *Adv. Mater.* **2011**, *23* (27), 3061.

(64) Meijer, A.; Farebrother A. J.; Clary, D. C. Isotope Effects in the Formation of Molecular Hydrogen on a Graphite Surface via an Eley−Rideal Mechanism. **2002,** 106 (39).

(65) Waqar, Z. Hydrogen Accumulation in Graphite and Etching of Graphite on Hydrogen Desorption. *J. Mater. Sci.* **2007**, *42* (4), 1169–1176.

(66) Elias, D. C.; Nair, R. R.; Mohiuddin, T. M. G.; Morozov, S. V; Blake, P.; Halsall, M. P.; Ferrari, A. C.; Boukhvalov, D. W.; Katsnelson, M. I.; Geim, A. K.; Novoselov, K. S. Control of Graphene's Properties by Reversible Hydrogenation: Evidence for Graphane. *Science* **2009**, *323* (5914), 610–613.

(67) Ryu, S.; Han, M. Y.; Maultzsch, J.; Heinz, T. F.; Kim, P.; Steigerwald, M. L.; Brus, L. E. Reversible Basal Plane Hydrogenation of Graphene. *Nano Lett.* **2008**, *8* (12), 4597–4602.

(68) Wojtaszek, M.; Tombros, N.; Caretta, A.; Van Loosdrecht, P. H. M.; Van Wees, B. J. A Road to Hydrogenating Graphene by a Reactive Ion Etching Plasma. *J. Appl. Phys.* **2011**, *110* (6).

(69) Le Bourlot, J.; Le Petit, F.; Pinto, C.; Roueff, E.; Roy, F. Surface Chemistry in the Interstellar Medium. *Astron. Astrophys.* **2012**, *541*, A76.

(70) Zhang, Y.; Li, Z.; Kim, P.; Zhang, L.; Zhou, C. Anisotropic Hydrogen Etching of Chemical Vapor Deposited Graphene. *ACS Nano* **2012**, *6* (1), 126–132.

(71) Sharma, S.; Kalita, G.; Vishwakarma, R. Opening of Triangular Hole in Triangular-Shaped Chemical Vapor Deposited Hexagonal Boron Nitride Crystal. *Sci. Rep.* **2015**, *5*, (10426).

(72) Henkelman, G.; Uberuaga, B. P.; Jonsson, H. A Climbing Image Nudged Elastic Band Method for Finding Saddle Points and Minimum Energy Paths. *J. Chem. Phys.* **2000**, *113* (22), 9901–9904.

(73) Hornekær, L.; Šljivančanin, Ž.; Xu, W.; Otero, R.; Rauls, E.; Stensgaard, I.; Lagsgaard, E.; Hammer, B.; Besenbacher, F. Metastable Structures and Recombination Pathways for Atomic Hydrogen on the Graphite (0001) Surface. *Phys. Rev. Lett.* **2006**, *96* (15).

(74) Borodin, V. A.; Vehviläinen, T. T.; Ganchenkova, M. G.; Nieminen, R. M. Hydrogen Transport on Graphene: Competition of Mobility and Desorption. *Phys. Rev. B - Condens. Matter Mater. Phys.* **2011**, *84* (7).

(75) Simon, J.M.; Haas, O.E.; Kjelstrup, S. Adsorption and Desorption of H_2 on Graphite by Molecular Dynamics Simulations. *J. Phys. Chem. C* **2010**, *114* (22), 10212–10220.

(76) Huang, L. F.; Ni, M. Y.; Zheng, X. H.; Zhou, W. H.; Li, Y. G.; Zeng, Z. Ab Initio Simulations of the Kinetic Properties of the Hydrogen Monomer on Graphene. *J. Phys. Chem. C* **2010**, *114* (51), 22636–22643.

(77) Jónsson, H.; Mills, G.; Jacobsen, K. W. Nudged Elastic Band Method for Finding

Minimum Energy Paths of Transitions. In *Classical and Quantum Dynamics in Condensed Phase Simulations*; World Scientific, **1998**; pp 385–404.

(78) Voter, A. F. Introduction To The Kinetic Monte Carlo Method. In *Radiation Effects in Solids*; Springer Netherlands: Dordrecht, **2007**; pp 1–23.

(79) Zamora, R. J.; Uberuaga, B. P.; Perez, D.; Voter, A. F. The Modern Temperature-Accelerated Dynamics Approach. *Annu. Rev. Chem. Biomol. Eng.* **2016**, *7* (1), 87–110.

(80) Sørensen, M. R.; Voter, A. F. Temperature-Accelerated Dynamics for Simulation of Infrequent Events. *J. Chem. Phys.* **2000**, *112* (21), 9599–9606.

(81) Voter, A. F. Parallel Replica Method for Dynamics of Infrequent Events. *Phys. Rev. B-Condens. Matter Mater. Phys.* **1998**, *57* (22), R13985–R13988.

(82) Miron, R. A.; Fichthorn, K. A. Accelerated Molecular Dynamics with the Bond-Boost Method. *J. Chem. Phys.* **2003**, *119* (12), 6210–6216.

(83) Voter, A. F. Hyperdynamics: Accelerated Molecular Dynamics of Infrequent Events. *Phys. Rev. Lett.* **1997**, *78* (20), 3908–3911.

(84) Bennett, C. H. Molecular Dynamics and Transition State Theory: The Simulation of Infrequent Events. In *Algorithms for Chemical Computations*; **1977**; pp 63–97.

(85) Perez, D.; Huang, R.; Voter, A. F. Long-Time Molecular Dynamics Simulations on Massively Parallel Platforms: A Comparison of Parallel Replica Dynamics and Parallel Trajectory Splicing. *J. Mater. Res.* **2017**, 1–10.

(86) Zhou, X. W.; El Gabaly, F.; Stavila, V.; Allendorf, M. D. Molecular Dynamics Simulations of Hydrogen Diffusion in Aluminum. *J. Phys. Chem. C* **2016**, *120* (14), 7500–7509.

(87) Alavi, S.; Shin, K.; Ripmeester, J. A. Molecular Dynamics Simulations of Hydrogen Bonding in Clathrate Hydrates with Ammonia and Methanol Guest Molecules. *J. Chem. Eng. Data* **2015**, *60* (2), 389–397.

(88) Tadmor, E.; Miller, R. *Modeling Materials: Continuum, Atomistic and Multiscale Techniques*. Cambridge University Press, **2011**.

(89) Tran, H. K.; Rasky, D. J.; Esfahani, L. Thermal Response and Ablation Characteristics of Lightweight Ceramic Ablators. *J. Spacecr. Rockets* **1994**, *31* (6), 993–998.

(90) Steg, L. Materials for Re-Entry Heat Protection of Satellites. *ARS J.* **1960**, *30* (9), 815–822.

(91) Gladysz, G.; Chawla, K. Material Voids in Heat Shield Protect Orion Spacecraft | SciTech Connect http://scitechconnect.elsevier.com/the-space-between-voids-in-heat-shield-protecting-orion-spacecraft/.

(92) Gladysz, G. M.; Chawla, K. K. Chapter 7 – Applications. In *Voids in materials: from unavoidable defects to designed cellular materials*. Newnes, **2015**; pp 131–156.

(93) Crouch, R. K.; Walberg, G. D. An Investigation of Ablation Behavior of Avcoat 5026/39M over a Wide Range of Thermal Environments. *NASA Technical Report,*

69N22933, Hampton, VA, **1969**.

(94) Trick, K. A.; Saliba, T. E.; Sandhu, S. S. A Kinetic Model of the Pyrolysis of Phenolic Resin in a Carbon/phenolic Composite. *Carbon* **1997**, *35* (3), 393–401.

(95) Anderson, H. C. Thermogravimetry of Polymer Pyrolysis Kinetics. *J. Polym. Sci. Part C Polym. Symp.* **2007**, *6* (1), 175–182.

(96) Friedman, H. L. Kinetics of Thermal Degradation of Char-Forming Plastics from Thermogravimetry. Application to a Phenolic Plastic. *J. Polym. Sci. Part C Polym. Symp.* **2007**, *6* (1), 183–195.

(97) Jiang, H.; Wang, J.; Wu, S.; Wang, B.; Wang, Z. Pyrolysis Kinetics of Phenol - Formaldehyde Resin by Non-Isothermal Thermogravimetry. *Carbon* **2010**, *48* (2), 352–358.

(98) Williams, S. D.; Curry, D. M. Thermal Protection Materials: Thermophysical Property Data. *NASA Technical Report*, 93N18765, Houston, TX, **1992**.

(99) Jiang, D.; van Duin, A. C. T.; Goddard, W. A.; Dai, S. Simulating the Initial Stage of Phenolic Resin Carbonization via the ReaxFF Reactive Force Field. *J. Phys. Chem. A* **2009**, *113* (25), 6891–6894.

(100) Desai, T. G.; Lawson, J. W.; Keblinski, P. Modeling Initial Stage of Phenolic Pyrolysis: Graphitic Precursor Formation and Interfacial Effects. *Polymer.* **2011**, *52* (2), 577–585.

(101) Qi, T.; Bauschlicher, C. W.; Lawson, J. W.; Desai, T. G.; Reed, E. J. Comparison of ReaxFF, DFTB, and DFT for Phenolic Pyrolysis: Molecular Dynamics Simulations. *J. Phys. Chem. A* **2013**, *117* (44), 11115–11125.

(102) Monk, J. D.; Haskins, J. B.; Bauschlicher, C. W.; Lawson, J. W. Molecular Dynamics Simulations of Phenolic Resin: Construction of Atomistic Models. *Polymer.* **2015**, *62*, 39–49.

(103) Morterra, C.; Low, M. J. D. I.R. Studies of Carbons-VII. The Pyrolysis of a Phenol-Formaldehyde Resin. *Carbon.* **1985**, *23* (5), 525–530.

(104) Murayama, T.; Bell, J. Relation between the Network Structure and Dynamic Mechanical Properties of a Typical Amine-cured Epoxy Polymer. *J. Polym. Sci. Part B Polym. Phys.* **1970**, 8(3), 437-445.

(105) Ogata, M.; Kinjo, N.; Kawata, T. Effects of Crosslinking on Physical Properties of Phenol–formaldehyde Novolac Cured Epoxy Resins. *J. Appl. Polym.* **1993**, *48*(4), 583-601

(106) Tzeng, S. S.; Chr, Y. G. Evolution of Microstructure and Properties of Phenolic Resin-Based Carbon/carbon Composites during Pyrolysis. *Mater. Chem. Phys.* **2002**, *73* (2–3), 162–169.

(107) Izumi, A.; Nakao, T.; Shibayama, M. Atomistic Molecular Dynamics Study of Cross-Linked Phenolic Resins. *Soft Matter* **2012**, *8* (19), 5283.

(108) Malhotra, H. C. Kinetics of the Acid-Catalyzed Phenol–formaldehyde Reaction. *J. Appl. Polym. Sci.* **1976**, *20* (9), 2461–2471.

(109) Mitsunaga, T.; Conner, A. H.; Hill, C. G. Predicting the Reactivity of Phenolic Compounds with Formaldehyde. II. Continuation of an Ab Initio Study. *J. Appl. Polym. Sci.* **2002**, *86* (1), 135–140.

(110) Fisher, T. H.; Chao, P.; Upton, C. G.; Day, A. J. One- and Two-Dimensional NMR Study of Resol Phenol-Formaldehyde Prepolymer Resins. *Magn. Reson. Chem.* **1995**, *33* (9), 717–723.

(111) Li, C.; Strachan, A. Molecular Dynamics Predictions of Thermal and Mechanical Properties of Thermoset Polymer EPON862/DETDA. *Polymer.* **2011**, *52*(13), 2920-2928.

(112) Sun, H.; Ren, P.; Fried, J. R. The COMPASS Force Field: Parameterization and Validation for Phosphazenes. *Comput. Theor. Polym. Sci.* **1998**, *8* (1–2), 229–246.

(113) Shenogin, S. ;Ozisi. R. XenoView v. 3.4. **2007**.

(114) Varshney, V.; Patnaik, S. S.; Roy, A. K.; Farmer, B. L. A Molecular Dynamics Study of Epoxy-Based Networks: Cross-Linking Procedure and Prediction of Molecular and Material Properties. *Macromolecules* **2008**, *41* (18), 6837–6842.

(115) Bandyopadhyay, A.; Valavala, P.; Clancy, T.; Wise, K. Molecular Modeling of Crosslinked Epoxy Polymers: The Effect of Crosslink Density on Thermomechanical Properties. *Polymer.* **2011**, *52*(11), 2445-2452.

(116) Winter, H. Can the Gel Point of a Cross-Linking Polymer Be Detected by the G′–G ″crossover? *Polym. Eng. Sci.* **1987**, *27*(22), 1698-1702.

(117) Chenoweth, K.; van Duin, A. C. T.; Goddard, W. A. ReaxFF Reactive Force Field for Molecular Dynamics Simulations of Hydrocarbon Oxidation. *J. Phys. Chem. A* **2008**, *112* (5), 1040–1053.

(118) Mottram, J.; Geary, B.; Taylor, R. Thermal Expansion of Phenolic Resin and Phenolic-Fibre Composites. *J. Mater. Sci.* **1992**, *27*(18), 5015-5026.

(119) Sellan, D. P.; Landry, E. S.; Turney, J. E.; McGaughey, A. J. H.; Amon, C. H. Size Effects in Molecular Dynamics Thermal Conductivity Predictions. *Phys. Rev. B* **2010**, *81* (21), 214305.

(120) Mottram, J. T.; Taylor, R. Thermal Conductivity of Fibre-Phenolic Resin Composites. Part I: Thermal Diffusivity Measurements. *Compos. Sci. Technol.* **1987**, *29* (3), 189–210.

(121) Mottram, J. T.; Taylor, R. Thermal Conductivity of Fibre-Phenolic Resin Composites. Part II: Numerical Evaluation. *Composites Science and Technology*. **1987**, *29*(3), 211-232

(122) Titov, E.; Kumar, R.; Levin, D.; Anderson, B. Modeling of the Crack Growth in the AVCOAT Heat Shield. In *AIAA Aerospace Sciences Meeting;* American Institute of Aeronautics and Astronautics: Reston, Virigina, **2011**.

(123) Kemp, N. H. Surface Recession Rate of an Ablating Polymer. *AIAA J.* **1968**, *6* (9), 1790–1791.

(124) Scala, S. M. A Study of Hypersonic Ablation. In *Xth International Astronautical Congress London 1959*; Springer Berlin Heidelberg: Berlin, Heidelberg, **1960**; 790–827.

(125) Jr, R. G.; Witte, W. Flight Test Analysis of Apollo Heat Shield Material Using the Pacemaker Vehicle System, *NASA Technical Report*, 68N30747, Hampton, VA, **1968**.

(126) Makeev, M. A.; Srivastava, D. Thermal Properties of Char Obtained by Pyrolysis: A Molecular Dynamics Simulation Study. *Appl. Phys. Lett.* **2009**, *95* (18), 181908.

(127) Loeb, A. L. Thermal Conductivity: VIII, A Theory of Thermal Conductivity of Porous Materials. *J. Am. Ceram. Soc.* **1954**, *37* (2), 96–99.

(128) Titov, E.; Kumar, R.; Levin, D.; Anderson, B. Development and Application of a Charring Ablator Thermal Response Model. In *42nd AIAA Thermophysics Conference*; American Institute of Aeronautics and Astronautics: Reston, Virigina, **2011**.

(129) Properties:Silica-Silicon Dioxide (SiO_2) https://www.azom.com/properties.aspx?ArticleID=1114 (accessed Feb 5, 2018).

(130) Davis, W. Determination of Heat-Shield Char-Front Recession with a Nucleonic Technique, *NASA Technical Report*, TND3264, Houston, TX, **1966**.

(131) Lisco, B.; Yao, E.; Pinero, D.; Koo, J. H.; Bouslog S. A. In-situ Ablation and Thermal Sensing of Two Low Density Ablators - Revisited. *Composites and Advanced Materials Expo* (CAMX)**, 2014**

(132) Finke, R. *Calculation of Reentry-Vehicle Temperature History*; Institute for Defense Analyses, Alexandria, VA, **1990**.

(133) Costa, R. R.; Silva, J. A.; Wu, S.-F.; Chu, Q. P.; Mulder, J. A. Atmospheric Re-Entry Modeling and Simulation: Application to a Lifting Body Re-Entry Vehicle. In *Proceedings of the AIAA Modeling and Simulation Technologies Conference and Exhibit*; **2000**; pp 1–11.

(134) Johnston, C. O.; Gnoffo, P. A.; Mazaheri, A. Study of Ablation-Flowfield Coupling Relevant to the Orion Heatshield. *J. Thermophys. Heat Transf.* **2012**, *26* (2), 213–221.

(135) Levendis, Y. A.; Flagan, R. C. Synthesis, formation and characterization of micron-sized glassy carbon spheres of controlled pore structure. *Carbon* **1989**, 27(2), 265-283.

(136) Lawson, J. W.; Srivastava, D. Formation and Structure of Amorphous Carbon Char from Polymer Materials. *Phys. Rev. B - Condens. Matter Mater. Phys*, **2008**, *77* (14), 144209.

(137) Harris, P. J. F. New Perspectives on the Structure of Graphitic Carbons. *Crit. Rev. Solid State Mater. Sci.* **2005**, *30* (4), 235–253.

(138) Ranganathan, R.; Rokkam, S.; Desai, T.; Keblinski, P. Generation of Amorphous Carbon Models Using Liquid Quench Method: A Reactive Molecular Dynamics Study. *Carbon.* **2017**, *113*, 87–99.

(139) Lawson, J. W.; Srivastava, D. Formation and Structure of Amorphous Carbon Char from Polymer Materials. *Phys. Rev. B - Condens. Matter Mater. Phys* **2008**, *77* (14), 144209.

(140) Jain, S. K., Pellenq, R. J. M., Pikunic, J. P., & Gubbins, K. E. Molecular modeling of porous carbons using the hybrid reverse Monte Carlo method. *Langmuir*, **2006**, *22*(24), 9942-9948.

(141) Stuart, S. J.; Tutein, A. B.; Harrison, J. A. A Reactive Potential for Hydrocarbons with Intermolecular Interactions. *J. Chem. Phys.* **2000**, *112* (14), 6472–6486.

(142) Jenkins, G. M.; Kawamura, K.; Ban, L. L. Formation and Structure of Polymeric Carbons. *Proc. R. Soc. London A Math. Phys. Eng. Sci.* **1972**, *327* (1571).

(143) Strachan, A.; van Duin, A. C. T.; Chakraborty, D.; Dasgupta, S.; Goddard, W. A. Shock Waves in High-Energy Materials: The Initial Chemical Events in Nitramine RDX. *Phys. Rev. Lett.* **2003**, *91* (9).

(144) Petersen, T.; Yarovsky, I.; Snook, I.; McCulloch, D. G.; Opletal, G. Microstructure of an Industrial Char by Diffraction Techniques and Reverse Monte Carlo Modelling. *Carbon* **2004**, *42* (12–13), 2457–2469.

(145) Opletal, G.; Petersen, T.; O'Malley, B.; Snook, I.; McCulloch, D. G.; Marks, N. A.; Yarovsky, I. Hybrid Approach for Generating Realistic Amorphous Carbon Structure Using Metropolis and Reverse Monte Carlo. *Mol. Simul.* **2002**, *28* (10–11), 927–938.

(146) Ozawa, T.; Levin, D. A.; Wang, A.; Modest, M. F. Development of Coupled Particle Hypersonic Flowfield- Photon Monte Carlo Radiation Methods. *J. Thermophys. Heat Transf.* **2010**, *24* (3), 612–622.

(147) Zhu, T.; Li, Z.; Levin, D. A. Modeling of Unsteady Shock Tube Flows Using Direct Simulation Monte Carlo. *J. Thermophys. Heat Transf.* **2014**, *28* (4), 623–634.

(148) Sawant, S. S.; Harpale, A.; Jambunathan, R.; Chew, H. B.; Levin, D. A. High Fidelity and Multi-Scale Thermal Response Modeling of an Avcoat-like TPS. In *AIAA Aerospace Sciences Meeting*; American Institute of Aeronautics and Astronautics: Reston, Virginia, **2017**.

(149) Sawant, S. S.; Rao, P.; Harpale, A.; Chew, H. B.; Levin, D. A. Correction: Micro-Scale Thermal Response Modeling of Avcoat-like TPS. In *AIAA Aerospace Sciences Meeting*; American Institute of Aeronautics and Astronautics: Reston, Virginia, **2018**.

(150) Sawant, S. S.; Rao, P.; Harpale, A.; Chew, H. B.; Levin, D. A. Micro-Scale Thermal Response Modeling of Avcoat-like TPS. In *AIAA Aerospace Sciences Meeting*; American Institute of Aeronautics and Astronautics: Reston, Virginia, **2018**.

(151) Ghoniem, A. F.; Sherman, F. S. Grid-Free Simulation of Diffusion Using Random Walk Methods. *J. Comput. Phys.* **1985**, *61* (1), 1–37.

(152) Talebi, S.; Gharehbash, K.; Jalali, H. R. Study on Random Walk and Its Application to Solution of Heat Conduction Equation by Monte Carlo Method. *Prog. Nucl. Energy* **2017**, *96*, 18–35.

(153) Vignoles, G. L. A Hybrid Random Walk Method for the Simulation of Coupled Conduction and Linearized Radiation Transfer at Local Scale in Porous Media with Opaque Solid Phases. *Int. J. Heat Mass Transf.* **2016**, *93*, 707–719.